Strojniški vestnik – Journal of Mechanical Engineering (SV-JME)

Cover:
A handheld optical system for in-vivo skin topography measurement which uses Fourier transform profilometry and optical triangulation methods has been developed and used for three dimensional reconstructions of skin surface samples. The reconstructions are done quickly and precisely, thus making this compact, lightweight and easy-handeling device convenient for use in dermatology and cosmetics.

Courtesy:
University of Ljubljana,
Faculty of Mechanical Engineering, Slovenia

ISSN 0039-2480

Contents

Strojniški vestnik - Journal of Mechanical Engineering
volume 61, (2015), number 5
Ljubljana, May 2015
ISSN 0039-2480

Published monthly

Papers

Handheld Optical System for Skin Topography Measurement Using Fourier Transform Profilometry

Jernej Laloš* – Marko Mrak – Urban Pavlovčič – Matija Jezeršek
University of Ljubljana, Faculty of Mechanical Engineering, Slovenia

In medicine and cosmetics a need has arisen for an accurate, fast, simple and broadly applicable three-dimensional skin surface measuring system. A new development of such handheld optical device that uses white light Fourier transform profilometry for skin surface topography measurement is presented here. The device is based on a commercially available DSLR camera and a newly designed optical system which projects a Ronchi grating pattern on the measured surface and records its image. The 3D surface is reconstructed from a single image. The topography is described using four surface roughness parameters: mean absolute deviation R_a, root-mean-square deviation R_q skewness R_{sk} and kurtosis R_{ku}. Experimental measurements were conducted on five facial skin areas, together belonging to three people, before and after the laser skin treatment therapy, to evaluate its effects on skin surface roughness. The results show the viability and usefulness of the developed optical system for skin topography measurement.
Keywords: Fourier transform profilometry, optical triangulation, skin topography, surface roughness parameters

Highlights
- A new handheld optical skin surface topography measuring system has been developed.
- The device is based on a DSLR camera with a newly designed flash light grating projector and image recording optics.
- The Fourier transform profilometry method is used for surface topography measurements.
- Surface topography is measured and reconstructed quickly and accurately from a single image.
- The surface roughness parameters are used to show the effects of laser skin treatment therapy on several people.

0 INTRODUCTION

Until recently, skin surface evaluations were done visually with no universally consistent measuring procedure. One example of this requires standardized digital photographs of the skin to be taken and visually assessed by experienced professionals [1].

In dermatology and cosmetics a need has arisen for an accurate, fast, broadly applicable, simple and cheap *in-vivo* skin surface measuring system. This kind of optical device would provide accurate and consistent information about the skin surface topography and colour. Its most significant new feature would be the introduction of depth measurement without any contact or invasive procedure.

Indeed great advancements have been made in skin surface measuring techniques and in the development of such systems and devices. The most practical and therefore most widely used technique for *in-vivo* skin surface analysis is fringe projection areal topography [2]. It is done by projecting a fringe pattern onto the measured surface and recording its image. The image is then processed by special computer software which calculates the topography of the surface [3].

Many commercial 3D skin surface measuring systems have been invented, some examples of which can be found in the literature: handheld skin surface measuring device [4], handheld body scanner [5], stationary face measuring device [6], to name a few. Most of these use non-coherent light sources, mainly light emitting diodes (LED). They operate with precision from 0.05 mm to 0.5 mm in ranges from 18 mm × 13 mm × 10 mm to 380 mm × 380 mm × 250 mm with data acquisition times from 0.001 s to 0.1 s.

Some experimental skin topography measuring systems may be different from commercial ones. They may use a flashtube as a light source [7], for example. Such devices can be used in medicine to study wounds [8]. A similar principle can also be used in three dimensional foot shape measurements [9], chest wall monitoring during breathing [10], head-to-trunk orientation determination [11] and the study of tissue ablation depths during laser treatments [12]. Similar devices are used for measuring numerous types of objects in science and industry where their adverse health and safety effects are not of concern [13].

This article presents a new optical system that uses the Fourier transform profilometry method [14] for skin surface topography measurement. It was developed primarily for precise and objective monitoring of the skin surface appearance after various laser based skin treatments [15].

In the interest of simplicity, accessibility and cost-effectiveness, this skin topography measuring system

was to be constructed out of as many commercially available products as possible. It was chosen to be based on a digital single-lens reflex (DSLR) camera with a non-coherent flashtube light source around which a camera-specific optical system was to be constructed.

1 FOURIER TRANSFORM PROFILOMETRY

Fourier transform profilometry is a type of fringe projection areal topography method in which the Fourier series expansion and Fourier transform of a single line grating pattern image are used together with optical triangulation to determine the topography of the measured surface [14].

The basics of crossed-optical-axes-with-parallel-optical-planes geometry is presented in Fig. 1. In this setup, the optical axes of the projector lens and camera lens intersect at a certain point. At that same time their respective optical planes coincide as well and they effectively form one single plane. This is useful because it ensures the proper orthogonal grating pattern projection without unnecessary distortions.
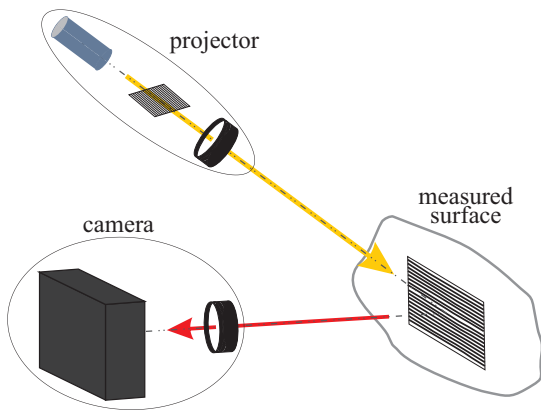
Fig. 1. *Basic element setup in crossed-optical-axes-with-parallel-optical-planes geometry*

The coincidence of both planes is achieved by using the Scheimpflug principle [16]. It determines at what angle θ an object plane transmitted through a lens with magnification M_p has to be tilted in order to produce an image plane tilted at an angle α_0 relative to the normal plane in the other direction:

$$\tan(\theta) = \frac{1}{M_p}\tan(\alpha_0). \qquad (1)$$

Therefore, the projection grating has to be tilted at the angle θ before it can be properly projected.

The spatial period of the line grating is p_0. However, when it is projected through a projector lens

with a magnification M_p, the projected grating pattern period becomes $p = M_p p_0$ which makes its projected spatial frequency $\xi_p = 1/p$.

Fig. 2 shows the principles of this kind of optical setup. The optical axes of the projector and camera lenses intersect at point O at angle α_0 and their optical planes coincide in plane I. It lies at a distance l_0 away from the camera lens and is perpendicular to its optical axis. A point H(x, y) on the measured object's surface is in the focus of interest.
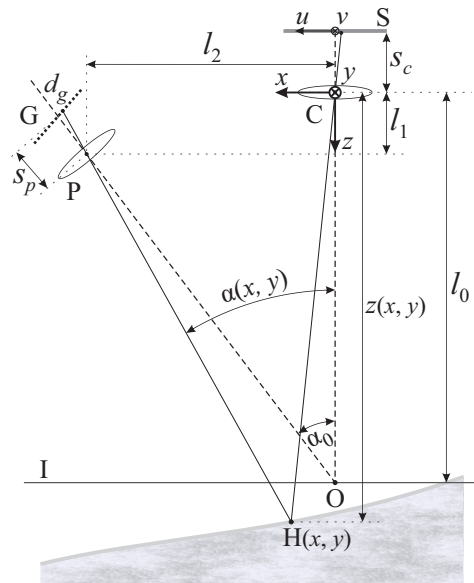
Fig. 2. *Optical schematics in crossed-optical-axes-with-parallel-optical-planes geometry; H(x, y) is a point of interest on the object surface; the optical axes of the projector lens (P) and the camera lens (C) intersect at point O and their optical planes coincide in plane I; (S) represents the camera sensor and (G) the projection grating*

A measurement takes the form of a recorded image of a grating pattern projected onto a measured surface. Such an image can be interpreted as multiple rows of light intensity signals modulated in phase $\phi(x, y)$ and amplitude $r(x, y)$ with the main spatial carrier frequency of ξ_p.

This kind of light intensity signal of a single row, as shown in Fig. 3a, can be expanded into the Fourier series in the x dimension which is perpendicular to the grating lines orientation:

$$g(x, y) = r(x, y) \sum_{n=-\infty}^{\infty} A_n e^{i(2\pi\xi_p x + \phi(x,y))}. \qquad (2)$$

Here, $r(x, y)$ represents the light distribution on the diffuse surface, $\phi(x, y)$ the phase shift and the A_n a Fourier coefficient.

The Fourier series expansion from Eq. (2) is then Fourier transformed and filtered. The Fourier transform is performed only in the x direction, perpendicular to the orientation of the grating lines, while y is kept fixed.

Frequency filtering filters out all frequencies except the fundamental one ξ_p and some of its closest neighbours. A Hanning window function centred at ξ_p is used [17]. Width w of the window function has to be carefully chosen – too wide and the signal may carry too much noise; too narrow and it may lose the sharp edge and discontinuity details [7]. Original spatial frequency distribution and its filtering is shown in Fig. 3b.

The filtered Fourier transform is inversely Fourier transformed back to a complex signal:

$$\hat{g}(x,y) = A_1 r(x,y) e^{i(2\pi\xi_p x + \phi(x,y))}. \tag{3}$$

The argument of this complex signal $\Phi(x,y) = 2\pi\xi_p x + \phi(x,y)$ contains phase shift information $\phi(x,y)$ and has to be expressed:

$$\Phi(x,y) = \arctan\left(\frac{\Im\left[\hat{g}(x,y)\right]}{\Re\left[\hat{g}(x,y)\right]}\right). \tag{4}$$

This kind of calculation gives principal values of the argument wrapped into an interval of $[-\pi, \pi]$. This creates discontinuity phase jumps of 2π for variations greater than 2π, as shown in Fig. 3c. Therefore, a phase unwrapping algorithm is necessary in order to reconstruct the correct continuous phase distribution. The one used here is two-dimensional and is presented in the literature [18]. This algorithm provides an optimal balance between quality and speed as it is designed to give priority to pixels with a higher reliability in order to prevent error propagation.

Once phase $\Phi(x,y)$ is obtained, trigonometry is used to determine the spatial coordinates of a surface point H(x,y). The coordinates x and y are calculated from their respective pixel positions on the camera sensor u and v. Coordinate $z(x,y)$, however, is calculated from:

$$z(x,y) = \frac{l_1 \tan(\alpha(x,y)) - l_2}{u - \tan(\alpha(x,y))}, \tag{5}$$

where

$$\alpha(x,y) = \alpha_0 + \arctan(\beta(x,y)), \tag{6}$$

and

$$\beta(x,y) = \frac{d_g}{s_p} - \frac{\Phi(x,y)}{2\pi s_p} p_0. \tag{7}$$

Here, d_g is a half-width of the grating and s_p is its mean distance from the projector lens.

Further details can be found in the literature [19] and [20].
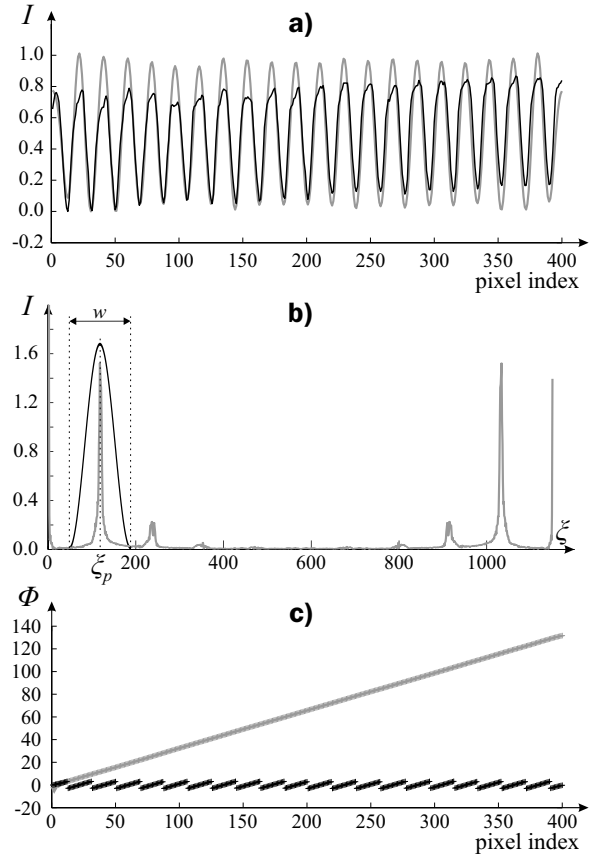
Fig. 3. *Typical processing signals of Fourier transform profilometry method; a) light intensity signal g(x,y) segment of one pixel row of the grating image taken before (black) and after frequency filtering (grey); b) spatial frequency distribution of the first signal (grey) and the window function for frequency filtering (black); c) phase Φ(x,y) of the first signal in the wrapped (black) and unwrapped (grey) state*

2 MEASURING SYSTEM

The core of this skin topography measuring system is a custom-made handheld device based on a commercially available DSLR camera with its built-in flash as a light source to which other optical components are added. The whole system is shown in Fig. 4 and its most important optical dimensions are shown in Fig. 5.

The structural body (B) is made out of a solid plastic block and has the function of rigidly holding the camera lens, the projector lens, the object spacer and the camera in precise relative positions to each other.
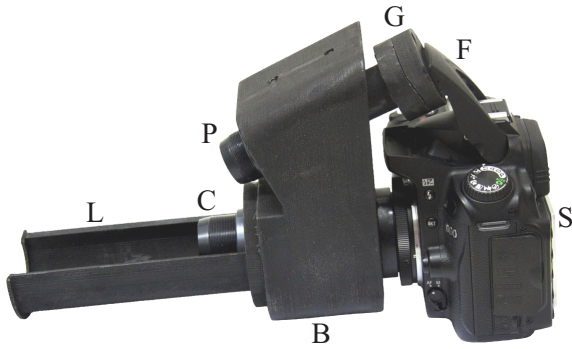
Fig. 4. *Handheld optical system for skin topography measurement:*
(B) structural body, (S) camera, (F) popup flash, (C) camera lens,
(P) projector lens, (G) projection grating, (L) object spacer
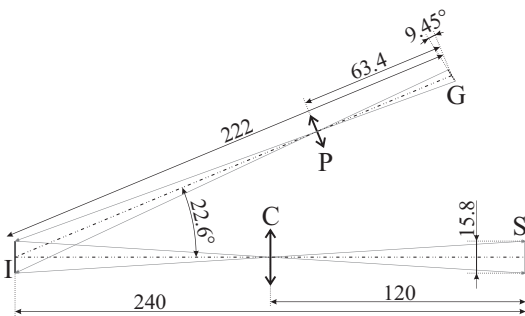
Fig. 5. *Schematics of the system's significant optical measurements in mm and degrees: (S) camera sensor, (C) camera lens, (P) projector lens, (G) projection grating, (I) main coincidental plane*

The camera (S) used here is Nikon D90 DSLR camera [21]. Its image sensor is a complementary metal-oxide-semiconductor (CMOS) active pixel sensor of Nikon DX format with dimensions of 23.6 mm × 15.8 mm. It has approximately 12.3 effective megapixels arranged in a 4288 × 2848 array. The camera has a sensitivity from 200 up to 3200 according to the International Organization for Standardization (ISO) standard [22]. It is attached to the structural body behind the camera lens on the same optical axis using a Samyang's lens mount adapter for T2 Lenses on a Nikon F mount.

The built-in pop-up flash (F) produces short white light projection illumination. When open, it is in line with the projector lens and projection grating.

The camera lens (C) is positioned at the base of the structural body and in line with the camera sensor and object spacer. It is an Edmund Optics' #32724 MgF_2 coated achromatic doublet lens with an effective focal length of $f_c = 60$ mm and an overall diameter of $d_c = 25.0$ mm. The camera lens setup has a designed optical magnification of $M_c = 1.0$, as seen on Fig. 5.

Its diaphragm is positioned at $a_c = 20$ mm behind the doublet.

The projector lens (P) is similar in design to the camera lens. It is positioned above the camera lens at an angle $\alpha_0 = 22.6°$ against it and in line with the projection grating and flash. The lens is an Edmund Optics' #45-136 MgF_2 coated achromatic doublet lens with an effective focal length of $f_p = 45$ mm and a diameter of $d_p = 12.5$ mm. The projector lens setup was designed to have an optical magnification of $M_p = 2.5$. The diaphragm of the projector lens is positioned at $a_p = 20$ mm behind the doublet.

The projection grating (G) is a horizontal line pattern Ronchi grating. The Edmund Optics' #58-776 1''×1'' (10 lp/mm) Ronchi ruling with a pattern period of $p_0 = 0.1$ mm was used. It sits in the object plane of the projector lens between the lens and the flash and in line with them. The grating is inclined towards the projector lens at an angle $\theta = 9.45°$ in accordance with the Scheimpflug principle so that its projected image falls correctly on the measured object.

The object spacer (L) is an open half-tube attached to the structural frame in line with the camera lens. Its open end is meant to lean against the measured object – skin in this case. The length of the spacer is chosen such that the distance between the open end of the spacer and the camera lens doublet is equal to the designed object plane distance of the camera lens $l_0 = 120$ mm, thus making the measured area lie in the object plane of the camera lens and in the image plane of the projector lens (I).

The whole optical device weighs 1500 g and measures 270 mm × 135 mm × 160 mm overall. It is robust, light and compact, making it convenient to be used as a portable handheld device.

Experimentally it was found that the flash powered with half of its maximum power provides an appropriate lighting for the purposes of Fourier transform profilometry. Due to a relatively short duration of flash illumination compared to the exposure time, the best possible setting is a shutter speed of 1/200 s at an ISO sensitivity of 200.

Special computer software was developed for the processing of the images. Its code was written in Visual C++ with the aid of the OpenCV and OpenGL libraries. In a few seconds the software analyses the image using the Fourier transform profilometry method. With it, each pixel row is transformed and filtered separately. The pixel rows are then combined into an array for the phase unwrapping and final calculations. This entire process determines the spatial positions of a large number of discrete points on the measured surface – as described in Section 1.

The calibration of the measuring system and corresponding computer software was done using a precisely manufactured reference surface with a known geometry which was measured at incremental distances between 115.5 mm and 125.5 mm from the camera lens. The captured images were imported into the software for the transformation parameter optimization. The parameters were optimized using the Powell's conjugate gradient descent method. This resulted in the standard deviation between the measurements and the reference surface being 0.05 mm. Further information about such a calibration can be found in the literature [7].

This optical system has an effective measuring range of 24 mm × 15 mm × 7 mm in which a precision of 0.05 mm is achieved. The computer software provides data about the position of the discrete points (x_i, y_i, z_i) on the surface of the measured object which correspond to each pixel in a rectangular grid of the camera sensor. The most interesting aspect of these data for the purposes of surface roughness determination is of course the vertical component in relation to its planar position $z_i(x_i, y_i)$.

A topography analysis of the measured surfaces is made using four surface roughness parameters: the mean absolute deviation R_a, the root-mean-square deviation R_q, the skewness R_{sk} and kurtosis R_{ku} [23]. In order to calculate these parameters, discrete reference points of a smooth reference plane had to be determined as an average value of all the measured points which lie in the neighbourhood of the corresponding measured point.

3 MEASUREMENTS

For experimental purposes, five facial skin areas, together belonging to three people, were measured. Thus the areas A1 and A2 belong to person A, areas B1 and B2 belong to person B and area C1 belongs to person C. Each skin surface area was measured twice – before and after the laser skin treatment therapy. While the purpose of this therapy was to smooth the skin, its effects were measured and evaluated here.

To provide a better diffuse reflection of light and a higher line pattern contrast on the semi-translucent and non-homogeneous skin surface, face powder was applied to the measured areas. Three-dimensional skin surface reconstructions from the captured images of the selected samples B2Be (before the therapy) and B2Af (after the therapy) are shown in Fig. 6.
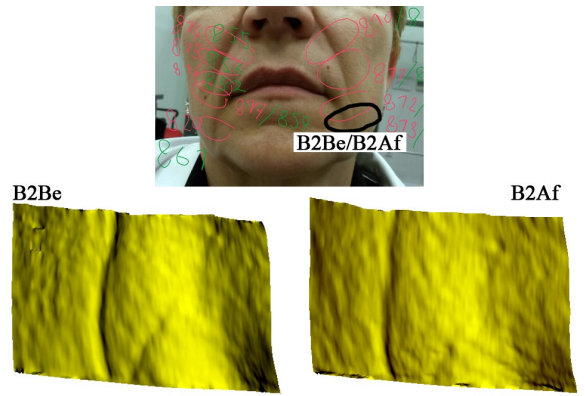
Fig. 6. *Experimentally measured areas of person B's facial skin (top) and three-dimensional skin surface reconstructions from the measurements of the area B2, before (sample B2Be) and after (sample B2Af) laser skin treatment therapy*

The surface roughness parameters were calculated from the measured data points. For the establishment of reference plane points, the neighbourhood O_i was chosen in the shape of an octagon with a diagonal of 2 mm. The calculated surface roughness parameters for each of the measured samples are presented in Table 1.

Table 1. *The calculated surface roughness parameters for the measured skin samples before (index .Be) and after (index .Af) the laser skin treatment therapy and the relative changes Δ in their absolute values; the parameters are: the mean absolute deviation R_a, the root-mean-square deviation R_q, the skewness R_{sk} and kurtosis R_{ku}; $\bar{\chi}$ represents the average value for all the samples and σ_χ their standard deviation*

	$R_{a.Be}$ [µm]	$R_{a.Af}$ [µm]	ΔR_a [%]	$R_{q.Be}$ [µm]	$R_{q.Af}$ [µm]	ΔR_q [%]	$R_{sk.Be}$	$R_{sk.Af}$	ΔR_{sk} [%]	$R_{ku.Be}$	$R_{ku.Af}$	ΔR_{ku} [%]
A1	92.6	75.2	−18.8	122.6	101.6	−17.1	−1.32	−1.17	−11.4	1.96	3.00	53.5
A2	93.5	70.0	−25.1	134.0	99.9	25.4	−1.65	−1.77	7.3	3.59	3.85	7.4
B1	51.5	48.9	−5.0	62.3	58.8	−5.6	−0.51	−0.60	18.5	−0.44	−0.56	28.0
B2	54.1	30.8	−43.1	69.3	39.7	−42.7	−1.20	−0.21	−82.6	1.14	0.06	−94.7
C1	53.6	60.9	13.6	71.0	78.9	11.1	−0.46	−1.38	201.0	1.08	0.91	−15.8
$\bar{\chi}$	69.1	57.2	−15.7	91.8	75.8	−16.0	−1.03	−1.03	26.6	1.46	1.45	−4.3
σ_χ	21.9	17.8	21.3	33.7	26.7	20.3	0.52	0.62	105.3	1.47	1.90	56.6

These statistically calculated surface roughness parameters show that most of the facial skin samples in general have a mean absolute deviation R_a between 45 μm and 80 μm and a root-mean-square deviation R_q between 55 μm and 110 μm. The parameters also show that the skin samples have low peaks and deep valleys ($R_{sk} < 0$) and that, for the most part, those peaks and valleys are relatively pointed ($R_{ku} > 0$).

Regarding the laser skin treatment therapy and its effect on skin surface roughness, it can be clearly seen from Table 1 that almost all of the samples measured after the therapy have lower parameters R_a and R_q compared to those measured before the therapy. This would suggest that the skin is indeed less rough after the therapy. However, the comparison of the parameters R_{sk} and R_{ku} before and after the therapy from all the samples together is quite inconclusive.

4 CONCLUSIONS

The measurement principle and design of a new optical three-dimensional skin topography measurement system is described. Its measuring range is 24 mm × 15 mm × 7 mm and its precision is 0.05 mm. Its small size, light weight, as well as its design and shape make it compact and easy-handling – a very convenient portable handheld device. *In-vivo* measurements and their analyses are done quickly and precisely.

The surface roughness parameters provide a simple way to quantify the surface roughness information of a skin sample. They help compare the surface roughness of different samples or that of a single sample at different times and circumstances. Here, the mean deviation R_a and the root-mean square deviation R_q parameters show a noticeable reduction in the height and depth of the skin profile after the laser skin treatment in almost all samples.

5 AKNOWLEDGEMENTS

6 REFERENCES

[1] Marini, L. (2013). 1064 nm Q-Switched photo-acoustic laser ablation of Xanthelasma Palpebrarum. *Journal of the Laser and Health Academy*, vol. 2013, no. 1, p. 48-51.

[2] Tchvialeva, L., Zeng, H., Markhvida, I., McLean, D. I., Lui, H., Lee, T.K. (2010). Skin roughness assessment. Campolo, D. (Ed.) *New Developments in Biomedical Engineering*. InTech, p. 341-358, **DOI:10.5772/7611**.

[3] Jezeršek, M., Možina, J. (2003). A laser anamorph profilometer. *Strojniški vestnik – Journal of Mechanical Engineering*, vol. 49, no. 2, p. 76-89.

[4] GFMesstechnik GmbH (2014). PRIMOS lite, from: *http://www.gfm3d.com/index.php?option=com_content&view=article&id=199\%3Aprimoslite&catid=48&lang=en*, accessed on 2014-10-15.

[5] Creaform (2014). Health Care Partner 3D scanner, from: *http://www.creaform3d.com/en/health-care-solutions/health-care-partner-3d-scanner*, accessed on 2014-10-15.

[6] 3D-Shape GmbH (2014). FaceSCAN3D and BodySCAN3D, from: *http://www.3d-shape.com/produkte/face_e.php*, accessed on 2014-10-15.

[7] Pavlovčič, U., Jezeršek, M., Možina, J. (2012). Handheld 3D measuring system based on DSLR camera. *Proceedings of the 3rd International Conference on 3D Body Scanning Technologies*, p. 74-80.

[8] Pavlovčič, U., Jezeršek, M., Možina, J. (2011). Laser triangulation system for the measurement of volume and color of wounds. *Proceedings of the 2nd International Conference on 3D Body Scanning Technologies*, p. 10-15.

[9] Novak, B., Babnik, A., Možina, J., Jezeršek, M. (2014). Three-dimensional foot scanning system with a rotational laser-based measuring head. *Strojniški vestnik – Journal of Mechanical Engineering*, vol. 60, no. 11, p. 685-693, **DOI:10.5545/sv-jme.2014.1950**.

[10] Jezeršek, M., Fležar, M., Možina, J. (2008). Laser multiple line triangulation system for real-time 3-D monitoring of chest wall during breathing. *Strojniški vestnik – Journal of Mechanical Engineering*, vol. 54, no. 7-8, p. 503-506.

[11] Pavlovčič, U., Diaci, J., Možina, J., Jezeršek, M. (2013). Characterization of the head-to-trunk orientation with handheld optical 3D apparatus based on the fringe projection technique. *BioMedical Engineering OnLine*, vol. 12, art. num. 96, **DOI:10.1186/1475-925X-12-96**.

[12] Nemes, K., Diaci, J., Ahcan, U., Marini, L., Lukac, M. (2014). Dependence of skin ablation depths on Er:YAG laser fluence. *Journal of the Laser and Health Academy*, vol. 2014, no. 1, p. 7-13.

[13] Brajlih, T., Tasič, T., Drstvenšek, I., Valentan, B., Hadžistević, M., Pogačar, V., Balič, J., Ačko, B. (2011). Possibilities of using three-dimensional optical scanning in complex geometrical inspection. *Strojniški vestnik – Journal of Mechanical Engineering*, vol. 57, no. 11, p. 826-833, **DOI:10.5545/sv-jme.2010.152**.

[14] Takeda, M., Mutoh, K. (1983). Fourier transform profilometry for the automatic measurement of 3-D object shapes. *Applied Optis*, vol. 22, no. 24, p. 3977-3982, **DOI:10.1364/AO.22.003977**.

[15] Gaspar, A., Gasti, G.A. (2013). Tightening of facial skin using intraoral 2940 nm Er:YAG smooth mode. *Journal of the Laser and Health Academy*, vol. 2013, no. 2, p. 17-20.

[16] Smith, W.J. (2000). *Modern Optical Engineering*. McGraw-Hill, New York.

[17] Pratt, W.K. (2001). *Digital Image Processing*. John Wiley & Sons, New York [etc.], **DOI:10.1002/0471221325**.

[18] Arevallilo Herráez, M., Burton, D.R., Lalor, M.J., Gdeisat, M.A. (2002). Fast two-dimensional phase-unwrapping algorithm based on sorting by reliability following a noncontinuous path. *Applied Optics*, vol. 41, no. 35, p. 7437-7444, **DOI:10.1364/AO.41.007437**.

[19] Su, X., Chen, W. (2001). Fourier transform profilometry: review. *Optics and Lasers in Engineering*, vol. 35, no. 5, p. 263-284, **DOI:10.1016/S0143-8166(01)00023-9**.

[20] Gåsvik, K.J. (2002). *Optical Metrology*, John Wiley & Sons, Chichester, **DOI:10.1002/0470855606**.

[21] Nikon Corporation (2008). *Digital camera D90 user's manual*. Nikon Corporation, Europe.

[22] ISO 12232:2006 (2006). *Photography — Digital still cameras — Determination of exposure index, ISO speed ratings, standard output sensitivity, and recommended exposure index*. International Organization for Standardization, Geneva.

[23] Whitehouse, D.J. (1994). *Handbook of Surface Metrology*. Institute of Physics Publishing, Bristol and Philadelphia.

The Study of Abrasive Water Jet Cutting Front Development using a Two-Dimensional Cellular Automata Model

Marko Jerman[1,*] – Joško Valentinčič[1] – Andrej Lebar[1,2] – Henri Orbanić[1]
[1] University of Ljubljana, Faculty of Mechanical Engineering, Slovenia
[2] University of Ljubljana, Faculty of Health Sciences, Slovenia

In this paper, the cutting front development during abrasive water jet (AWJ) cutting is studied using a two-dimensional cellular automata (CA) model, hence the striation formation phenomenon is studied indirectly. To calculate the shape of the cutting front, the CA model uses the following inputs: cutting velocity, AWJ intensity and material type. The cutting process is described by simplified material removal and AWJ propagation models in the form of CA rules. The rules encompass AWJ ability to erode the workpiece material and, inversely, the workpiece material's resistance to the erosion process. The proposed CA model is validated by checking the trend of the cutting front development at various input parameters. The simulation results are in good agreement with experimentally obtained trends and thus confirm the proper setup of CA rules. This gives a better insight into the AWJ cutting mechanism.
Keywords: abrasive water jet, cutting front, striation formation, cellular automata, simulation

Highlights
- *A simplified and efficient modelling of striation generation mechanism using a 2D cellular automata model is presented.*
- *The CA model takes into account the material removal model by the solid particle erosion process and the AWJ flow model which considers both energy potential and the direction in which it moves.*
- *The simulation results like flow redirection, not cutting through the workpiece and cutting of different materials are possible to obtain.*
- *The model predictions are in good agreement with experimentally obtained trends.*
- *The model offers a better insight into the AWJ cutting mechanism.*

0 INTRODUCTION

Abrasive water jet (AWJ) machining is a non-conventional machining process, which uses a high-speed water jet to accelerate hard abrasive grains in order to remove workpiece material. The process is mostly used for 2D and 3D cutting. In general, it can be used to cut any kind of material, regardless of its composition, structure, hardness or other physical properties. Many new materials in use today are impossible or very difficult to machine with other processes.

Typically, the surface cut by AWJ is striated. The striations are curved opposite to the cutting direction. The curvature and thickness mostly depend on the workpiece material, AWJ cross section, intensity and cutting velocity. Removal processes, which include solid particle erosion, e.g. AWJ machining, are very complex and thus difficult to describe theoretically [1]. Consequently, several numerical models have been developed to simulate the AWJ cutting process and to better understand it. Still, the main challenge is to develop a good striation formation model and thus try to find a solution which would reduce this phenomenon.

Several researchers have developed numerical models of AWJ cutting by recognizing the importance of describing the trajectory of abrasive grains and then calculating the material removal. The final results produced either 2D cutting front shapes or 3D cut surfaces, depending on the model complexity:

Fukunishi et al. [2] and [3] have developed a numerical model based on multiple jet impacts and Bitter's erosion theory [4] and [5]. A similar approach was used by Vikram and Babu [6] and El Tobgy et al. [7] who used a different material erosion model. Yong and Kovacevic [8] used a numerical method of memory cells to record the depth achieved by erosion of each abrasive grain. Ditzinger et al. [9] analyzed the formation of surface structures during the cutting process. Lebar [10] and Lebar and Junkar [11] developed the unit event model for generating the topography of the surface made by AWJ cutting. Deam et al. [12] developed a two-part two-dimensional model which predicts the shape of the cutting front. Zaki et al. [13] coupled a Computational Fluid Dynamics (CFD) solver, which simulates the dynamics of the AWJ, and a simplified material erosion. Some recent research has dealt with numerical simulations in such a way that LS-DYNA software was used to couple the AWJ flow model and material removal model [14] and [15].

The reviewed models show that extensive work has been performed in this area, but often the results

*Corr. Author's Address: University of Ljubljana, Faculty of Mechanical Engineering, Aškerčeva 6, 1000 Ljubljana, Slovenia,marko.jerman@fs.uni-lj.si

are limited to one material or a limited number of process parameter combinations. The cellular automata (CA) approach presented in this paper can, on the other hand, give a better insight into the studied process. CA have been used to model various processes found in nature and technology. They can be found in medicine for modelling the spread of virus infections [16], the growth of cancerous tissue [17] or image processing [18]. Other uses involve modelling of various diffusion processes, forest fires [19] and traffic [20]. In the area of mechanical engineering, CA have been used for modelling the structural changes in materials [21], modelling of etching process in integrated circuit manufacturing process [22] and fluid mechanics [23]. CA are extensively used in geology for modelling land erosion [24] and river meandering [25]. A similar process called solid particle erosion is the basic material removal mechanism in AWJ machining. The usage of CA for modelling of the AWJ machining process was first reported in Orbanic and Junkar's research paper [26].

In this paper, a significantly improved version of a previous two-dimensional CA model of AWJ cutting developed by Orbanic and Junkar [26] is presented, which simulates the development of the cutting front as it depends on the process parameters. The model allows a simple description of a complex process on a micro level, such as AWJ flow and material removal process for different types of material, and then quickly produces results for the macro level, thus allowing to quickly check different hypotheses. Additionally, the CA method is relatively simple to implement into computer code and offers vast parallelisation capabilities, which drastically shorten the computational times.

The main goal of the paper is to check the hypothesis described in the previous work performed by one of the authors [27], stating that the striation formation process is influenced by the shape of the cutting front. Based on it, special concern is given to the material model for various types of workpiece materials and the influence of the cutting front shape on the direction of AWJ flow and the direction of material removal. In the end the simulation was compared with actual experiments in order to confirm the proper functioning of the model.

1 NUMERICAL MODEL

The CA represent an idealization of a physical system, in which space and time are discrete and the physical quantities take only a finite set of values [28]. They consist of equally distributed arrays, which can be

of unlimited range. Each element of the array is characterized by a value of a certain physical quantity. This physical quantity, as a collection of all states in cells at a certain time, represents the global state of the CA. On the other hand, the value of the physical quantity in each cell represents a local state of the CA. Each cell in the CA can only interact with those cells that are in its neighbourhood. As a consequence, the cells in the CA are not able to communicate on a global level with other cells [29].

1.1 CA AWJ Cutting Model Definition

When using CA the modelled space of the process (AWJ cutting) has to be digitalized i.e. divided into an array of equal sized cells. The procedure is schematically shown in Fig. 1 where three characteristic areas define the states of CA: empty space – ES, abrasive water jet – AWJ and workpiece material – MAT.
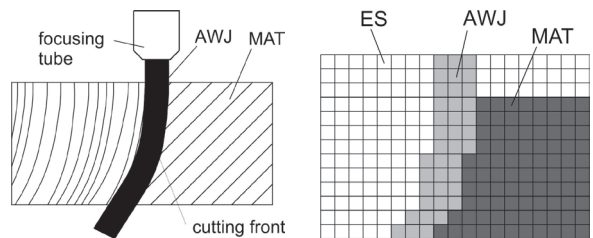
Fig. 1. *The digitization of the AWJ cutting process with three characteristic areas*

The difference between this and the base model previously described [26] is the reduced number of states. In this model, ES is a part of the AWJ state. This state represents the intensity of the AWJ or its ability to remove material. It is defined by two parameters:
- The first parameter is the intensity of AWJ (A_{awj}), which describes the kinetic energy of the jet, thus it depends on the process parameters, such as water pressure, water and abrasive mass flow rate, type and size of abrasive grains and geometry of the cutting head. Since the generation process of AWJ is very complex, it is currently not included in the model.
- The second parameter is the jet flow direction vector which describes the direction of AWJ operation. The empty space, which is part of the AWJ state, represents the state with low intensity and undefined flow direction. The MAT state is defined as a material removal resistance. It is represented by the parameter M_{mat}. The higher

the value of the parameter, the more time is required to remove the whole cell of material. The parameter M_{mat} is defined according to the machinability number N_m as:

$$M_{mat} = 10000 / N_m . \qquad (1)$$

The machinability number was introduced by Zeng and Kim [30] and [31]. In their semi-empiric model of AWJ cutting N_m represents a unique material property while cutting with AWJ. It is a simplified machining parameter of material erosion resistance, which was defined by authors in their theoretical model for calculating the depth of cut. Because N_m decreases with harder to machine materials, the Eq. (1) uses an inverse form. Currently, the N_m goes up to 15,000 [32] for foams which in practice are cut with pure water jet; therefore, a value of 10,000 was chosen as a limit at which the material can be cut without an abrasive.

The quantity of the removed material is calculated according to the intensity and impact angle of AWJ flow acting against a material cell with certain material resistance. At the same time the intensity of the AWJ in the neighbouring cells, which participated in the process of material removal, is reduced. After the new shape of the cutting front is determined, the normal vector at each point of the front is determined. This vector is later used for calculation of flow direction change for each part of the AWJ because of its contact with the cutting front. The contact was modelled as a specular reflection, thus by using the appropriate equation the new flow direction is calculated.

The AWJ flow in each cell is described by the intensity and direction value. The flow is considered to be infinite, and the intensity changes according to the flow direction in the cell, the intensity of the neighbouring cells and according to the energy spent for material removal. The previously mentioned definition of low AWJ intensity inside empty space cells was used in order to simulate the free flow of the jet in an empty space.

The whole area of CA is divided into an array of $n \times m$ cells. Rows are denoted by a variable i: the top row has a value 1 and the bottom row has a value n. Columns are denoted by the variable j: the left column has a value 1 and the right column has a value m.

In this space nine matrices are defined. The first matrix **B**, also called the matrix of states, represents the global space of CA. The values in this matrix can be 1 if the state is workpiece material or 2 otherwise (AWJ or empty space). Therefore, matrix **B** represents an instant picture of the process cycle. The border

between the two states represents the cutting front. After initialization, all cells in matrix **B** have the state 1 except the cells in the first row ($i=1$) for moving the AWJ source, which is described by matrix **C,** and initial columns (in our case $j=\{1,2,3\}$ as described latter).

Matrix **A** contains values of AWJ intensity for each cell, and matrix **M** contains the values of material removal resistance. Matrices N_x and N_y contain x and y components of the normal vector of the cutting front for each cell. Matrices S_x and S_y contain x and y components of the AWJ flow direction vector for each cell. The last two matrices Φ and **R** contain the inclination of the cutting front and material removal coefficients for each cell, which are calculated according to the cutting front inclination. It should be noted that the values for matrices N_x, N_y, Φ and **R** are 0 in cells which do not lie on the cutting front.

Initialization of matrices **A** and **M** are performed according to the Table 1. For the cells in state 2 (matrix **B**), the initial values of matrix **A** where the AWJ is situated are equal to A_{awj} and value 1 elsewhere. The latter value is needed for the purpose of AWJ intensity redistribution calculation as presented in the concept description.

Table 1. *Initialization of matrices **A** and **M** depends on the values in matrix **B***

B(i,j)	**A**(i,j)	**M**(i,j)
1	0	M_{mat}
2	1 or A_{awj}	0

A very important part of the CA is the definition of the AWJ source. The source is represented by a one-dimensional **C** array, which contains the information about jet diameter, the initial value of the AWJ intensity and its distribution. The flow vector of the source is directed downwards i.e. in $-y$ direction. The jet's movement is simulated by moving matrix **C** in the first row of the CA. Matrix **C** elements have the initial A_{awj} value while the rest of the first row cells have value 1. Movement of the matrix **C** is defined by the number of simulation cycles t_c needed to move the matrix one cell forward, i.e. $j+1$. Thus it is defined as the inverse value of the simulated cutting velocity v_c in unit cells per cycle (Eq. (2)).

$$t_c = v_c^{(-1)}. \qquad (2)$$

For calculations in the CA, the von Neumann neighbourhood with radius one (Fig. 2) was chosen.

1.2 Numerical Calculation Procedure

In the numerical simulation first the CA area is divided on an $n \times m$ matrix of identical square cells. Initial conditions are imposed by changing the states of specified CA cells and defining initial values for material resistance in **M** and initial values for AWJ intensity in **A**. The first row is reserved for jet movement, i.e. movement of subarray **C**. After initialization, the simulation starts. On each cycle the condition for jet movement according to number t_c is checked. Each time it is fulfilled the jet moves forward by one cell, otherwise the jet stays in place. Then the CA rules are checked. The simulation continues until the total number of time steps is equal to T after which the simulation stops. The global states of the CA are recorded during each time step, and the shape of the cutting front is determined and recorded.
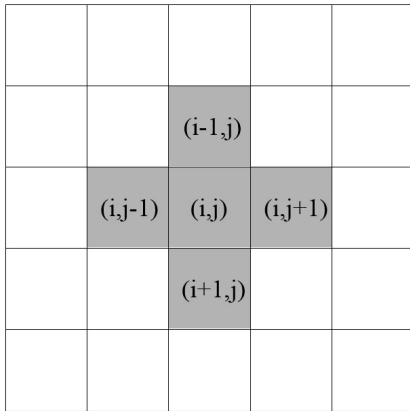
Fig. 2. *The von Neumann neighbourhood of the (i, j) cell comprised 5 grey cells*

1.2.1 *CA Cycle Definition*

The single cycle in the CA forms one time step and is composed out of five phases, which are sequentially executed in the simulation (Fig. 3), while in the real process these phases are overlapping. The sequence in the model starts first with the calculation of material removal. Then the current cutting front shape is determined and followed by the first redistribution of the AWJ intensity inside the AWJ flow. Next is the calculation of the AWJ flow direction change in each cell due to contact with the cutting front, followed by the second redistribution of the AWJ intensity and the calculation of the final direction of the AWJ flow.

As the CA cycle has five phases, the superscript ranges from 1 to 5. For example, superscript "$t+1, 1$" means the value of the variable at time $t+1$ in the first part of the CA cycle, while "$t+1, 5$" means the value of the variable at time $t+1$ in the last part of the CA cycle.

The first phase in the CA cycle to be performed is the rule for material removal, and it is performed in cells where the local state in matrix **B**, i.e. $B_{i,j}$ is equal to 1:

$$M_{i,j}^{t+1} = M_{i,j}^{t} - A_{i-1,j}^{t} \cdot R_{i-1,j}^{t} \cdot sgn\left(A_{i-1,j}^{t}\right) -$$
$$- A_{i+1,j}^{t} \cdot R_{i+1,j}^{t} \cdot sgn\left(A_{i+1,j}^{t}\right) -$$
$$- A_{i,j-1}^{t} \cdot R_{i,j-1}^{t} \cdot sgn\left(A_{i,j-1}^{t}\right) -$$
$$- A_{i,j+1}^{t} \cdot R_{i,j+1}^{t} \cdot sgn\left(A_{i,j+1}^{t}\right), \qquad (3)$$

where $M_{i,j}^{t+1}$ represents the material removal resistance at $t+1$, $M_{i,j}^{t}$ material removal resistance
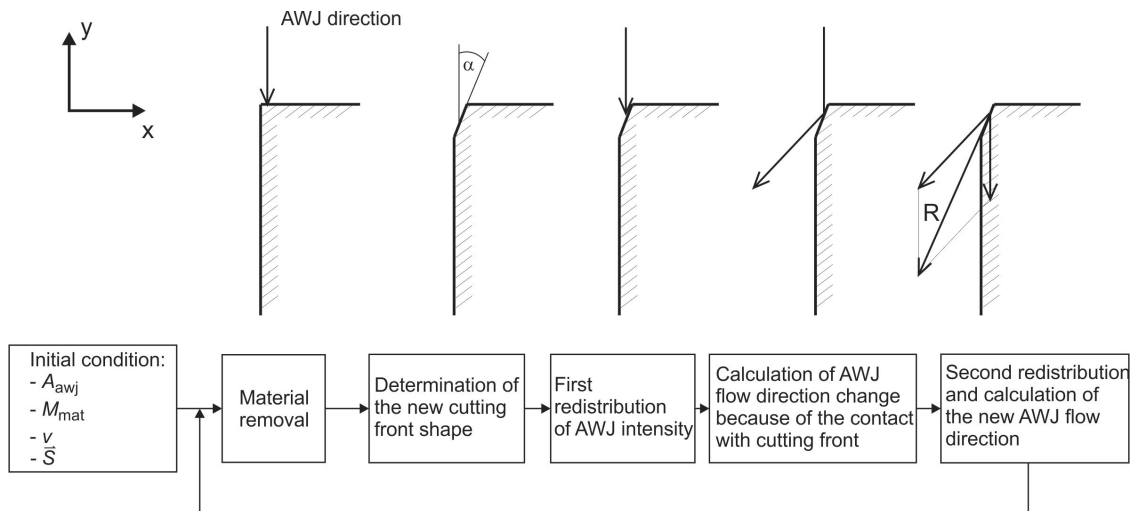
Fig. 3. *The five phase sequence during a single cycle of the CA*

at t, $R_{i-1,j}^{t}$, $R_{i+1,j}^{t}$, $R_{i,j-1}^{t}$ and $R_{i,j+1}^{t}$ are material removal coefficients at time t. During the calculation of material removal, only cells with AWJ intensity higher than 1 can participate, thus the signum function $sgn(x)$ in combination with the floor function $[x]$ is used. The floor function first rounds AWJ intensity downwards in cells $A_{i-1,j}^{t}$, $A_{i+1,j}^{t}$, $A_{i,j-1}^{t}$ and $A_{i,j+1}^{t}$ in such a way that values less than 1 are rounded to 0. Next, the signum function is used. For a real number x it is defined as follows:

$$sgn(x) = \begin{cases} -1 & if \quad x < 0, \\ 0 & if \quad x = 0, \\ 1 & if \quad x > 0. \end{cases} \quad (4)$$

Therefore, whole parts of Eq. (3) can be discarded if AWJ intensity in neighbouring cells is lower than 1. If $M_{i,j}^{t+1} < 0$, the value of $M_{i,j}^{t+1}$ is switched to 0 in order to prevent negative material resistance. A similar approach was used by Karafyllidis and Thanailakis [22]. When $M_{i,j}^{t+1} = 0$, the material is removed and the cell $B_{i,j}^{t+1}$ changes from state 1 to state 2 which means that the cell is filled by the AWJ flow.

After the material removal rule is performed in the given cell (i, j), the AWJ intensity is proportionally reduced in the neighbouring cells depending on the participation of each cell in the material removal process according to the following equations:

$$A_{i-1,j}^{t+1,1} = A_{i-1,j}^{t} \cdot \left(1 - R_{i-1,j}^{t}\right), \quad (5)$$

$$A_{i+1,j}^{t+1,1} = A_{i+1,j}^{t} \cdot \left(1 - R_{i+1,j}^{t}\right), \quad (6)$$

$$A_{i,j+1}^{t+1,1} = A_{i,j+1}^{t} \cdot \left(1 - R_{i,j+1}^{t}\right), \quad (7)$$

$$A_{i,j-1}^{t+1,1} = A_{i,j-1}^{t} \cdot \left(1 - R_{i,j-1}^{t}\right), \quad (8)$$

where $A_{i-1,j}^{t+1,1}$, $A_{i+1,j}^{t+1,1}$, $A_{i,j+1}^{t+1,1}$ and $A_{i,j-1}^{t+1,1}$ are AWJ intensities in the neighbouring cells in the first part of the CA cycle.

The second phase of the CA cycle determines the new shape of the cutting front and calculates the normal vectors on the cutting front. The matrix of material removal coefficients **R** and the new direction of AWJ flow after impact with the cutting front are calculated. The cutting front shape is obtained from the matrix of states **B** by determining the position of material cells at the border with AWJ cells.

Before the normal vector for each point on the cutting front is determined, a tangent vector of the curve $\vec{r}$ has to be calculated. This is done by subtracting position vectors of neighbouring points on the cutting front. To simplify further calculations the vector is normalized into $\hat{r}$. In order to obtain the normal vector $\vec{n}$, vector needs to be rotated around axis z for an angle duration of $-90°$ as shown in Fig. 4. The rotation around the z-axis is performed by using rotation matrix **T**:

$$\hat{n} = \mathbf{T} \cdot \hat{r} = \begin{bmatrix} \cos\left(-\frac{\pi}{2}\right) & -\sin\left(-\frac{\pi}{2}\right) & 0 \\ \sin\left(-\frac{\pi}{2}\right) & \cos\left(-\frac{\pi}{2}\right) & 0 \\ 0 & 0 & 1 \end{bmatrix} \cdot \begin{bmatrix} r_x \\ r_y \\ 0 \end{bmatrix} =$$

$$= \begin{bmatrix} 0 & 1 & 0 \\ -1 & 0 & 0 \\ 0 & 0 & 1 \end{bmatrix} \cdot \begin{bmatrix} r_x \\ r_y \\ 0 \end{bmatrix} = \begin{bmatrix} r_y \\ -r_x \\ 0 \end{bmatrix}. \quad (9)$$

The calculated normal vectors have to be entered into two matrices $\mathbf{N_x}$ and $\mathbf{N_y}$ where each one contains the x and y components of normal vectors. In this way each normal vector on the cutting front is transferred to the corresponding cell of the CA. Next, the impact angle φ is calculated for each cell on the cutting front (Eq. 10) and, based on this, the necessary material removal coefficients. Since all matrices of flow direction and normal vector components are normalized, it follows that:

$$\cos(\mathbf{\Phi}) = \frac{\mathbf{N_x} \cdot \mathbf{S_x} + \mathbf{N_y} \cdot \mathbf{S_y}}{1 \cdot 1}, \quad (10)$$

where $\mathbf{\Phi}$ is the matrix of the cutting front inclination. The value of matrix $\mathbf{\Phi}$ in cells which are not on the cutting front is equal to 0.

Fig. 4. *Normal vector $\vec{n}$ is perpendicular to the tangent vector $\vec{r}$ in the clockwise direction*

The matrix of material removal coefficients **R** is calculated by using the polynomial of 4th degree, which

was experimentally determined by Lebar [10] and by Lebar and Junkar [11] for solid particle erosion of aluminium by AWJ. It describes the material removal rate dependence on the impact angle of the AWJ. For this research, the polynomial was normalized in order to simulate cutting of ductile materials:
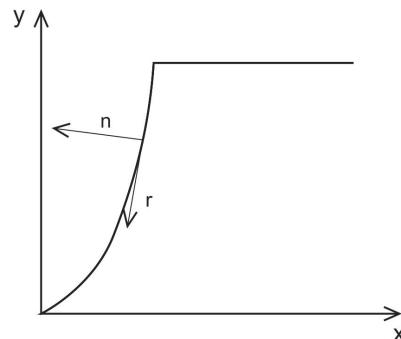
$$\mathbf{R} = 5.6 \cdot 10^{-8} \cdot \Phi^4 - 4.5 \cdot 10^{-6} \cdot \Phi^3 - $$
$$-4.8 \cdot 10^{-4} \cdot \Phi^2 + 4.7 \cdot 10^{-2} \cdot \Phi + 1.8 \cdot 10^{-3}. \quad (11)$$

This equation can also be used for other materials (ductile and brittle materials that under certain conditions show ductile behaviour during solid particle erosion), since only the relation between material removal and impact angle is required for CA calculations. According to several publications [33] to [35], this can occur at lower impact angles (up to 30°) and smaller sizes of abrasive grains. During many practical examples where solid particle erosion appears (such as AWJ cutting), lower impact angles are usually predominant [33]. In this paper, cutting of soda lime glass, which is grouped under brittle materials, was simulated. On the other hand, its machinability by AWJ is higher than most of the metals which show ductile behaviour.

The third phase of the cycle is the first redistribution of the AWJ intensity in matrix **A**. Redistribution in the cell (i,j) is calculated by the weighted average, where the weights w are determined with regard to the flow direction vector in the cell. Before the redistribution, a change of direction vectors in the cell needs to be calculated due to the mutual interaction between cells with state 2. This simulates the changes inside the flow itself. Applying Eqs. (12) to (14), the resultant of direction vectors in the neighbourhood of the cell (i,j) is calculated, and then normalization of the resultant vector by Eqs. (15) and (16) is performed:

$$S_{x(i,j)}^{t+1,3} = S_{x(i,j)}^{t} + S_{x(i-1,j)}^{t} + S_{x(i+1,j)}^{t} + $$
$$+ S_{x(i,j-1)}^{t} + S_{x(i,j+1)}^{t}, \quad (12)$$

$$S_{y(i,j)}^{t+1,3} = S_{y(i,j)}^{t} + S_{y(i-1,j)}^{t} + S_{y(i+1,j)}^{t} + $$
$$+ S_{y(i,j-1)}^{t} + S_{y(i,j+1)}^{t}, \quad (13)$$

$$\left| S_{y(i,j)}^{t+1,3} \right| = \sqrt{\left(S_{x(i,j)}^{t+1,3} \right)^2 + \left(S_{y(i,j)}^{t+1,3} \right)^2}, \quad (14)$$

$$\hat{S}_{x(i,j)}^{t+1,3} = \frac{S_{x(i,j)}^{t+1,3}}{\left| S_{i,j}^{t+1,3} \right|}, \quad (15)$$

$$\hat{S}_{y(i,j)}^{t+1,3} = \frac{S_{y(i,j)}^{t+1,3}}{\left| S_{i,j}^{t+1,3} \right|}. \quad (16)$$

The weights for neighbouring cells are calculated by Eqs. (17) to (20):

$$w_{i-1,j} = \left| \hat{S}_{y(i,j)}^{t+1,3} \right| \cdot \left(-1 + \operatorname{sgn}\left(\hat{S}_{y(i,j)}^{t+1,3} \right) \right)\left(-\frac{1}{2} \right), \quad (17)$$

$$w_{i,j-1} = \left| \hat{S}_{x(i,j)}^{t+1,3} \right| \cdot \left(1 + \operatorname{sgn}\left(\hat{S}_{x(i,j)}^{t+1,3} \right) \right)\left(\frac{1}{2} \right), \quad (18)$$

$$w_{i,j+1} = \left| \hat{S}_{x(i,j)}^{t+1,3} \right| \cdot \left(-1 + \operatorname{sgn}\left(\hat{S}_{x(i,j)}^{t+1,3} \right) \right)\left(-\frac{1}{2} \right), \quad (19)$$

$$w_{i+1,j} = \left| \hat{S}_{y(i,j)}^{t+1,3} \right| \cdot \left(1 + \operatorname{sgn}\left(\hat{S}_{y(i,j)}^{t+1,3} \right) \right)\left(\frac{1}{2} \right). \quad (20)$$

When calculating the weights, only two weights are considered per each cell while the other two are equal to zero. This is the consequence of the following rule: the AWJ flow is directed regarding the components x and y of the flow direction vector of the (i,j) cell. The new AWJ intensity for the (i,j) cell in the third part of the cycle is calculated by Eq. (21):

$$A_{i,j}^{t+1,3} = \frac{\begin{bmatrix} A_{i-1,j}^{t+1,1} \\ A_{i,j-1}^{t+1,1} \\ A_{i,j+1}^{t+1,1} \\ A_{i+1,j}^{t+1,1} \end{bmatrix} \cdot \begin{bmatrix} w_{i-1,j} \\ w_{i,j-1} \\ w_{i,j+1} \\ w_{i+1,j} \end{bmatrix}}{w_{i-1,j} + w_{i,j-1} + w_{i,j+1} + w_{i+1,j}}. \quad (21)$$

This procedure is repeated for every cell in the CA matrix.

The fourth phase of the cycle calculates the change of AWJ flow direction due to the flow contact with the cutting front. It was assumed that the interaction is similar to the specular reflection, which means the flow direction vector of the cell (i,j) has to be mirrored around the normal vector in the same cell. Therefore, a transformation matrix for calculating reflection **Z** was defined according to the data in existing research [36]. The matrix for the three dimensional Cartesian space is defined according to the vector around which the mirroring is being performed:

$$\mathbf{Z} = \begin{bmatrix} -\mathbf{N}_x^2 + \mathbf{N}_y^2 + \mathbf{N}_z^2 & -2 \cdot \mathbf{N}_x \cdot \mathbf{N}_y & -2 \cdot \mathbf{N}_x \cdot \mathbf{N}_z \\ -2 \cdot \mathbf{N}_y \cdot \mathbf{N}_x & \mathbf{N}_x^2 - \mathbf{N}_y^2 + \mathbf{N}_z^2 & -2 \cdot \mathbf{N}_y \cdot \mathbf{N}_z \\ -2 \cdot \mathbf{N}_z \cdot \mathbf{N}_x & -2 \cdot \mathbf{N}_z \cdot \mathbf{N}_y & \mathbf{N}_x^2 + \mathbf{N}_y^2 - \mathbf{N}_z^2 \end{bmatrix}. \quad (22)$$

Thus, the equation for mirroring the flow direction vectors in two dimensions is:

$$\begin{bmatrix} \hat{\mathbf{S}}_x^{t+1,4} \\ \hat{\mathbf{S}}_y^{t+1,4} \end{bmatrix} =$$

$$= \begin{bmatrix} -\mathbf{N}_x^2 + \mathbf{N}_y^2 & -2\cdot\mathbf{N}_x\cdot\mathbf{N}_y & \hat{\mathbf{S}}_x^{t+1,3}\cdot\left(1-\left|sgn\left(\mathbf{N}_x\right)\right|\right) \\ -2\cdot\mathbf{N}_y\cdot\mathbf{N}_x & -\mathbf{N}_y^2 + \mathbf{N}_x^2 & \hat{\mathbf{S}}_y^{t+1,3}\cdot\left(1-\left|sgn\left(\mathbf{N}_y\right)\right|\right) \end{bmatrix} \cdot$$

$$\cdot \begin{bmatrix} \hat{\mathbf{S}}_x^{t+1,3} \\ \hat{\mathbf{S}}_y^{t+1,3} \\ 1 \end{bmatrix}. \qquad (23)$$

This rule is performed only in cells which are near the cutting front and where the normal vector components in those cells have nonzero values. In this way, the change of the AWJ flow direction vector to $(0,0)$ is prevented in cells not at the cutting front.

The fifth and last phase of the CA cycle contains the second redistribution of the AWJ intensity which follows the jet deflection. This part is similar to the third phase but is necessary for calculation of resulting flow direction vectors and redistribution of the AWJ intensity resulting from the interaction between AWJ cells, which changed flow direction due to deflection from the cutting front, and those which did not. The calculations for this part are performed with the same set of equations as in part three (Eqs. (12) to (21)).

2 SIMULATION SETUP

The CA space is divided into 55×150 cells, thus all the matrices except matrix **C** are of this size. The AWJ source is 3 cells wide, bringing the first three columns of matrix **B** to state 2. The rest of the cells are taken as the workpiece material, so they are in state 1. Therefore, the dimension of the workpiece is 54×147 cells. The variable input parameters, which have to be set before the simulation start, are material resistance M_{mat}, AWJ source intensity A_{awj} and simulation cutting velocity v_c. It was also decided to use a uniform distribution of the AWJ intensity at the source; therefore, all three cells have the same value. The initial value of material removal resistance M_{mat} is calculated with Eq. (1).

The CA simulation was programmed using the MATLAB numerical computing environment. The total number of time steps T required for complete the simulation was determined according to the simulation cutting velocity and the number of CA columns m:

$$T = v_c^{-1}\cdot m. \qquad (24)$$

The time to complete each simulation depends on the size of the CA. On an average office PC the time step duration for a matrix with dimensions 55×150 was on average 0.6 seconds for all simulations.

The simulation results are presented in the form of consecutive cutting fronts recorded during each simulation run. The single recording is obtained from matrix **B** by determining the border between different states as it is shown in Fig. 5.
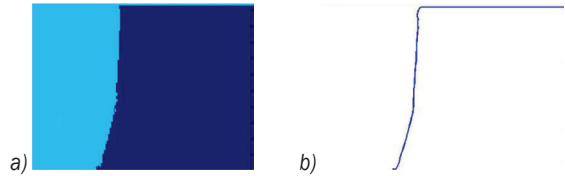
Fig. 5. *a) the image of matrix B; and b) the border between different states*

3 EXPERIMENTAL WORK

3.1 Time Step Determination

For simulation calibration purposes, the dimensions of the square cell were defined. If the focusing nozzle of 0.8 mm diameter is used, the size of the cell is equal to $0.8/3 \cong 0.267$ mm. This means the thickness of the workpiece in the simulation is 14.4 mm.

Because the simulation has two unknown parameters A_{awj} and a time step, it was decided to first fix the AWJ intensity and calibrate the simulation by matching the results for separation cut velocity. This is more pragmatic, as there is still no practical method to measure AWJ intensity. In order to perform the calibration the separation cut velocity for a particular AWJ machine setup, material and thickness has to be determined. This velocity is recorded when the AWJ just barely cuts through the workpiece. This velocity can also be calculated by using Zeng's equation [31] for calculating the depth of cut. If the operating parameters stated in Table 2 are used at the lowest cutting quality, the calculated separation cut is approximately 7 mm/s. The same parameters were used to practically perform such a cut on the OMAX 2652A AWJ machine. For practical purposes, the used workpiece thickness was 15 mm.

In order to calibrate the CA model the parameters A_{awj} and t_c, which control the cutting velocity v_c, have to be properly set in order for the separation cut to be obtained in simulation too. The AWJ intensity in the simulation was set to $A_{awj} = 200$, which at the same

time means that the calibration of jet parameters will also be performed.

By varying the t_c parameter in Eq. (2) and visually comparing the result to the real separation cut as presented in Fig. 6, the simulation separation cut velocity was found to be $v_c = 0.167$. In this case t_c was equal to 6, meaning the AWJ moves forward one cell each 6 time steps. The simulation result is composed of consecutive recordings of the cutting fronts. For the sake of clarity, only every third front is shown.

Simulation	Experiment
$v_c = 0.167$	$v = 7\ mm/s$
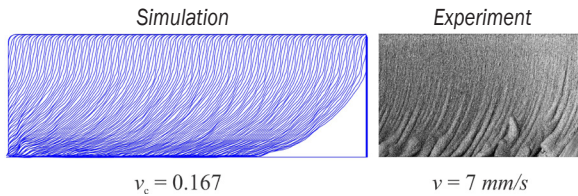
Fig. 6. *Matching the separation cut velocity*

Table 2. *Separation cut process parameters*

Water pressure	[MPa]	300
Water orifice diameter	[mm]	0.25
Focusing tube diameter	[mm]	0.8
Abrasive mass flow rate	[kg/min]	0.22
Abrasive type		Garnet # 80
Cutting velocity	[mm/s]	7
Stand-off distance	[mm]	2
Material type (machinability number)		AlMgSi1 (213)

Now the time step length can be determined. If the time needed to pass one cell the size of 0.267 mm with velocity of 7 mm/s is equal to 0.0381 s, then the time step size is equal to $0.0381/6 \cong 0.00635$ s.

3.2 Trend Confirmation

The further experimental work was focused on comparing the results with the simulation performance if 1) the cutting velocity is changed, 2) water pressure is changed and 3) different workpiece material is used. The additional parameters are presented in Table 3. The cut samples were then visually compared to the simulation results in order to compare trends.

Table 3. *Additional process parameters used for the experiments*

Water pressure	[MPa]	200, 250, 300, 350
Cutting velocity	[mm/s]	5, 6, 7, 8, 9
Material type (machinability number)		AlMgSi1 (213), Steel St-37 (82), Soda lime glass (322)

4 RESULTS

4.1 Variation of Velocity

At first, the cutting velocity was varied according to Table 3 while all other parameters were fixed. In the experiment aluminium alloy AlMgSi1 was cut at a water pressure of 300 MPa. The simulation cutting velocity v_c can be calculated from the real velocity, cell size and time step by the following relation:

$$v_c = \frac{v}{cell\ size} \cdot time\ step. \qquad (25)$$

This relation defines the distance made by AWJ in the time of one time step, i.e. cell size per time step. The corresponding velocities are given in Table 4. The initial AWJ intensity at the source A_{awj} was set to 200 as in the case of calibration.

The examples of simulation and experimental results for cutting velocities between 5 mm/s and 9 mm/s are shown in Fig. 7.

Table 4. *Simulation velocities*

Cutting velocity	[mm/s]	5, 6, 7, 8, 9
Calculated v_c	[cell/time step]	0.125, 0.143, 0.167, 0.2, 0.25

Simulation	Experiment
$v_c = 0.125$	$v = 5\ mm/s$
$v_c = 0.143$	$v = 6\ mm/s$
$v_c = 0.167$	$v = 7\ mm/s$
$v_c = 0.2$	$v = 8\ mm/s$
$v_c = 0.25$	$v = 9\ mm/s$
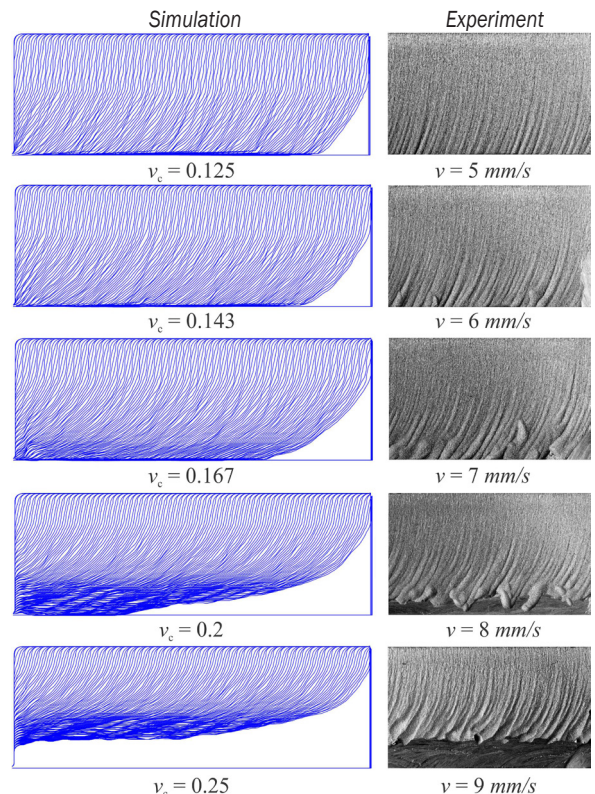
Fig. 7. *The comparison of cutting velocities in a) simulation and b) experiment*

4.2 AWJ Intensity and Material Resistance

The simulation was tested for the change of initial AWJ intensity at the source of the jet and for the material resistance to the removal. The former corresponds to the change of water pressure (the abrasive parameters were left unchanged), whereas the latter corresponds to the material type. The simulation cutting velocity was fixed at $v_c = 0.167$, which corresponds to v = 7 mm/s in the experiments.
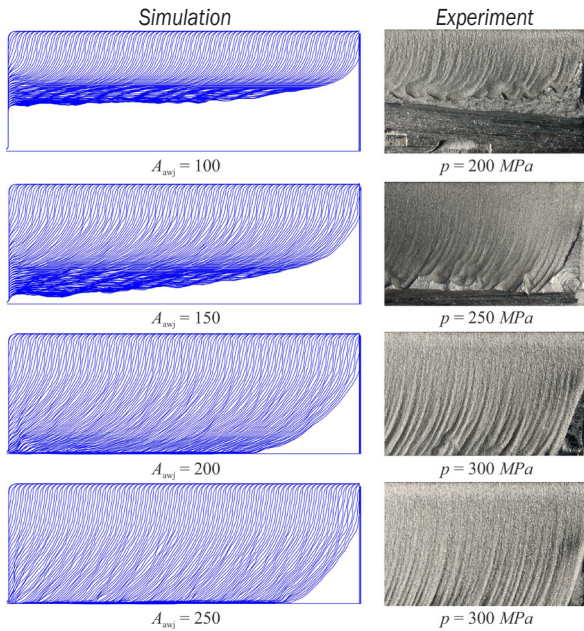
Fig. 8. *The comparison of different AWJ intensities in a) simulation and b) experiment*
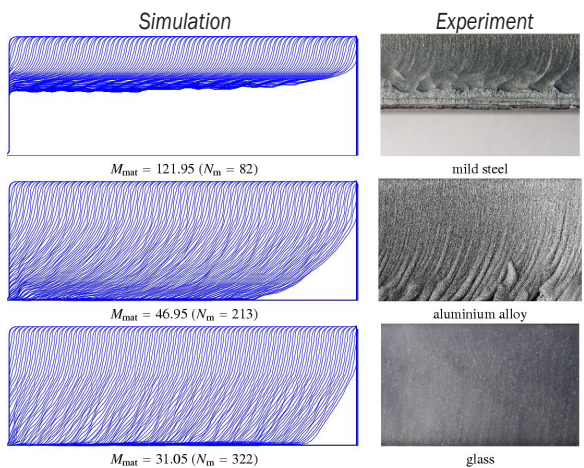
Fig. 9. *The comparison of cutting different materials in a) simulation and b) experiment*

According to known facts [37], the final result during AWJ cutting is linearly proportional to the change in water pressure. Thus the AWJ intensity parameter was changed in equal increments according to Table 3 while in the simulation the parameter A_{awj} was varied between value 100 and 250 based on the calibration run. The results for both the simulation and experiment are shown in Fig. 8 in the left and right columns, respectively.

The results of the simulation for three different materials according to Table 3 are presented for both the simulation and experiment in Fig. 9 in the left and right columns, respectively. Three different materials were chosen where aluminium alloy was taken as a reference from the calibration run while the other two materials have worse and better machinability than aluminium.

5 DISCUSSION

The simulation results show that the model is sound because by changing the input parameters, the curvature of the cutting front change is consistent with the response in the real process.

The presented model also considers redirection of AWJ flow. This allows it to also predict situations where the workpiece is not cut through due to higher cutting velocities. The results agree with those observed in the experiments.

With the previous model [26] this could not be simulated, as it was purely an energy based model which did not take into account the influence of abrasive slurry flow over the cutting front. In reality, when the cutting velocity for a certain material and a certain thickness is sufficiently high, the workpiece is not cut through even though it maintains significant energy to remove the material. This is due to the jet redirection at the bottom of the cut and not the AWJ intensity reduction [27].

The AWJ flow redirection at the cutting front depends on the interaction time between AWJ flow and workpiece material, AWJ intensity, AWJ flow direction and material type. While the first one is influenced by cutting velocity, which defines how much time the jet will have to remove a particular part of material, the later three deal with the material removal mechanism and thus define the material removal rate. If we want to focus on the cutting front development and its later influence on the cutting process, the proper material removal model has to be established. As solid particle erosion depends on the velocity of the abrasive grains, their impact angles and material type, all these parameters have been included into the CA model. This was done by calculating AWJ flow intensity in each cell, the direction of the flow,

impact angle at the cutting front, flow redirection at the front, material resistance to erosion depending on the material type and the impact angle. It was shown that the relation between different materials defined by Zeng and Kim [31] can be used to simulate the cutting of a variety of materials. Also, it was shown that because of low impact angles at the cutting front, the relation between impact angle and material removal rate for ductile materials can on micro level be used for materials often regarded as brittle, e.g. glass. Compared to the previous models mentioned in the introduction, the major advantage of the CA method is it being a simplified and efficient model of AWJ cutting macro-mechanism, which can be used for further study of the process.

The presented 2D model on the other hand suffers from limitations connected to the striation generation mechanism, which is a three-dimensional problem and therefore has to be modelled in a three-dimensional space. This goes particularly for the occurrence of the so-called step, as the anomaly responsible for the striation formation can only be correctly obtained in 3D, as this was already established in previous research [27].

6 CONCLUSIONS

A qualitative CA model for simulating the cutting with AWJ has been developed. It was shown that the CA approach can be successfully used to describe the AWJ cutting process. In order for the model to simulate the development of the cutting front by varying process parameters, such as cutting velocity, AWJ intensity and material type, the material removal and AWJ flow mechanisms have to be properly defined. The material removal model encompasses the solid particle erosion process and its parameters while the AWJ flow model considers both energy potential and the direction in which it moves. Therefore, the simulation results like flow redirection, not cutting through the workpiece and cutting of different materials are possible to obtain.

The presented model is a stepping stone towards modelling the striation generation mechanism in a three-dimensional space. Although the influence of the cutting front surface shape on the striation formation was partially confirmed in the presented 2D model, this will be fully possible in 3D. Thus, the CA model should be expanded into the third dimension, which requires adding additional equations for the third dimension.

8 REFERENCES

[1] Levy, A.V. (1995). *Solid Particle Erosion and Erosion-Corrosion of Materials*. ASM International, Materials Park.

[2] Fukunishi, Y., Kobayashi, R. and Uchida, K. (1995). Numerical simulation of striation formation on water jet cutting. *Proceedings of the 8th Water Jet Conference*, vol. 2, WJTA, Houston, p. 657-670.

[3] Sawamura, T., Fukunishi, Y. (1997). Three dimensional model for waterjet cutting simulation. *Proceedings of the 9th Water Jet Conference*, vol. 1, WJTA, Dearborn, p. 133-144.

[4] Bitter, J.G.A. (1963). A study of erosion phenomena - Part I. *Wear*, vol. 6, p. 5-21, **DOI:10.1016/0043-1648(63)90003-6**.

[5] Bitter, J.G.A. (1963). A study of erosion phenomena - Part II. *Wear*, vol. 6, p. 169-190, **DOI:10.1016/0043-1648(63)90073-5**.

[6] Vikram, G., Babu, N.R. (2001). Modelling and simulation of abrasive water jet cut surface topography. *Proceedings of the 11th Water Jet Conference*. vol. 1, WJTA, Minneapolis, p. 13-28.

[7] El Tobgy, M., Ng, E.G., Elbestawi, M.A. (2005). Modelling of abrasive waterjet machining: a new approach. *CIRP Annals – Manufacturing Technology*, vol. 54, no. 1, p. 285-288, **DOI:10.1016/S0007-8506(07)60104-8**.

[8] Yong, Z., Kovacevic, R. (1997). 3D simulation of macro and micro characteristics for AWJ machining. *Proceedings of the 9th Water Jet Conference*, vol. 1, WJTA, Dearborn, p. 15-28.

[9] Ditzinger, T., Friedrich, R., Henning, A., Radons, G. (1999). Non-linear dynamics in modelling of cutting edge geometry. *Proceedings of the 10th Water Jet Conference*, vol. 1, WJTA, Houston, p. 15-32.

[10] Lebar, A. (2002). *Modelling of Abrasive Water Jet Cutting Process*. PhD thesis, University of Ljubljana, Ljubljana.

[11] Lebar, A., Junkar, M. (2003). Simulation of abrasive waterjet machining based on unit event features. *Proceedings of the Institution of Mechanical Engineers, Part B: Journal of Engineering Manufacture*, vol. 217, p. 699-703, **DOI:10.1243/095440503322011425**.

[12] Deam, R.T., Lemma, E., Ahmed, D.H. (2004). Modelling of the abrasive water jet cutting process. *Wear*, vol. 257, no. 9-10, p. 877-891, **DOI:10.1016/j.wear.2004.04.002**.

[13] Zaki, M., Corre, C., Kuszla, P., Chinesta, F. (2008). Numerical simulation of the abrasive waterjet (AWJ) machining: multi-fluid solver validation and material removal model presentation. *International Journal Material Forming*, vol. 1, p. 1403-1406, **DOI:10.1007/s12289-008-0127-8**.

[14] Jianming, W., Na, G., Wenjun, G. (2010). Abrasive waterjet machining simulation by SPH method. *International Journal of Advanced Manufacturing Technology*, vol. 50, no. 1-4, p. 227-234, **DOI:10.1007/s00170-010-2521-x**.

[15] Wenjun, G., Jianming, W., Na, G. (2011). Numerical simulation for abrasive water jet machining based on ALE algorithm.

International Journal of Advanced Manufacturing Technology, vol. 53, no. 1-4, p. 247-253, **DOI:10.1007/s00170-010-2836-7**.

[16] Benyoussef, A., El Hafid Allah, N., El Kenz, A., Ez-Zaharouy, H., Loulidi, M. (2003). Dynamics of HIV infection on 2D cellular automata. *Physica A: Statistical Mechanics and its Applications*, vol. 322, p. 506-520, **DOI:10.1016/S0378-4371(02)01915-5**.

[17] Alarcon, T., Byrneb, H.M., Maini, P.K. (2003). A cellular automaton model for tumour growth in inhomogeneous environment. *Journal of Theoretical Biology*, vol. 225, p. 257-274, **DOI:10.1016/S0022-5193(03)00244-3**.

[18] Viher, B., Dobnikar, A., Zazula, D. (1998). Cellular automata and follicle recognition problem and possibilities of using cellular automata for image recognition purposes. *International Journal Medical Informatics*, vol. 49, no. 2, p. 231-241, **DOI:10.1016/S1386-5056(98)00042-2**.

[19] Dobnikar, A., Vavpotic S., Likar, A. (2002). Dynamic systems modeling with stochastic cellular automata (evolutionary versus stochastic correlation approach). *Journal of Computing and Information Technology – CIT*, vol. 10, no. 4, p. 251-259, **DOI:10.2498/cit.2002.04.01**.

[20] Maerivoet, S., De Moor, B. (2005). Cellular automata models of road traffic. *Physics Reports*, vol. 419, no. 1, p. 1-64, **DOI:10.1016/j.physrep.2005.08.005**.

[21] Zhang, L., Wang, Y.M., Zhang, C.B., Wang, S.Q., Ye, H.Q. (2003). A cellular automaton model of transformation from austenite to ferrite in low carbon steels. *Modelling and Simulation in Material Science and Engineering*, vol. 11, no. 5, p. 791-802, **DOI:10.1088/0965-0393/11/5/306**.

[22] Karafyllidis, I., Thanailakis, A. (1995). Simulation of the two-dimensional photoresist etching process in integrated circuit fabrication using cellular automata. *Modelling and Simulation in Material Science and Engineering*, vol. 3, no. 5, p. 629-642, **DOI:10.1088/0965-0393/3/5/004**.

[23] Wolf-Gladrow, D.A. (2000). *Lattice-gas Cellular Automata and Lattice Boltzmann Models: an Introduction*. Springer, Berlin, **DOI:10.1007/b72010**.

[24] D'Ambrosio, D., Di Gregorio, S., Gabriele, S., Gaudio, R. (2001). A cellular automata model for soil erosion by water. *Physics and Chemistry of the Earth, Part B*, vol. 26, no. 1, p. 33-39, **DOI:10.1016/S1464-1909(01)85011-5**.

[25] Murray, A.B., Paola, C. (1994). A cellular model of braided rivers. *Nature*, vol. 371, p. 54-57, **DOI:10.1038/371054a0**.

[26] Orbanic, H., Junkar, M. (2004). Simulation of abrasive water jet cutting process: Part 2. Cellular automata approach. *Modelling and Simulation in Material Science Engineering*, vol. 12, p. 1171-1184, **DOI:10.1088/0965-0393/12/6/011**.

[27] Orbanic, H., Junkar, M. (2008). Analysis of striation formation mechanism in abrasive water jet cutting. *Wear*, vol. 265, no. 5-6, p. 821-830, **DOI:10.1016/j.wear.2008.01.018**.

[28] Chopard, B., Droz, M. (1998). Cellular Automata Modelling of Physical Systems. Cambridge University Press, **DOI:10.1017/CB09780511549755**.

[29] Wolfram, S. (1994). *Cellular Automata and Complexity*. Addison-Wesley, Reading.

[30] Zeng, J., Kim, T.J. (1992). Development of an abrasive waterjet kerf cutting model for brittle materials. *Proceedings of 11th International Conference on Jet Cutting Technology*, St. Andrews, Kluwer Academic Publishers, p. 483-501, **DOI:10.1007/978-94-011-2678-6_33**.

[31] Zeng, J., Kim, T.J. (1995). Machinability of engineering materials in abrasive water jet machining. *International Journal of Water Jet Technology*, vol. 2, no. 2, p. 103-110.

[32] OMAX Intelli-MAX Premium (2009) *OMAX Make for Windows*, Version: 14.0.

[33] Finnie, I. (1995). Some reflections on the past and future of erosion. *Wear*, vol. 186-187, p. 1-10, **DOI:10.1016/0043-1648(95)07188-1**.

[34] Ballout, Y., Mathis, J.A., Talia, J.E. (1996). Solid particle erosion mechanism in glass. *Wear*, vol. 196, no. 1-2, p. 263-269, **DOI:10.1016/0043-1648(96)06922-0**.

[35] Wensink, H., Elwenspoek, M.C. (2002). A closer look at the ductile-brittle transition in solid particle erosion. *Wear*, vol. 253, no. 9-10, p. 1035-1043, **DOI:10.1016/S0043-1648(02)00223-5**.

[36] Baker, M.J. (2011). Euclidian Space, from *http://www.euclideanspace.com/maths/geometry/affine/reflection/index.htm* accessed on 2011-10-06.

[37] Momber, A.W., Kovacevic, R. (1998). Principles of Abrasive Water Jet Machining, Springer-Verlag, London, **DOI:10.1007/978-1-4471-1572-4**.

Numerical Calculation of Tooth Profile
of a Non-circular Curved Face Gear

Chao Lin* – Dong Zeng – Xianglu Zhao – Xijun Cao
Chongqing University, The State Key Laboratory of Mechanical Transmission, China

Based on the cylindrical coordinates and the space engagement theory, which utilize a cylindrical coordinate system, an arbitrary curve equation was obtained and a method of curve expansion was established. This allows any order of pitch curve of non-circular curved face gear and normal equidistant curve parameter equations to be derived. The tooth profile points of the non-circular curved face gear can be solved using the numerical calculation method where the tooth profile intersects with the pitch curve and normal equidistant curves of non-circular curved face gear. Finally the numerical method used to solve the tooth profile of the non-circular curved face gear was proved to be accurate and correct from the small error between measured data and the data of theoretical calculation.
Keywords: non-circular curved face gear, cylindrical coordinates, pitch curve, numerical calculation of tooth profile, error analysis

Highlights
- *Built a mathematical model and a expansion method of an arbitrary curve.*
- *Derived equations of the pitch curve and the normal equidistant curves of the non-circular curved face gear.*
- *Proposed a numerical method to calculate the tooth profile.*
- *Measured the tooth profile and analyzed the error of the tooth profile to verify the numerical method.*

0 INTRODUCTION

The non-circular curved face gear drive is also called the orthogonal variable transmission ratio face gear drive. It is generated by replacing the spur pinion and its conjugated face gear of a conventional face gear drive by a non-circular gear and its conjugated face gear [1]. The transmission ratio is variable when the non-circular curved face gear engages with non-circular gear, since the teeth distributed on the cylindrical surface. This is the most significant feature compared to the conventional face gear. This type of gear drive has many possible applications in the field of engineering, textile, agriculture, etc.

In 1940, Buckingham came up with the concept of the face gear in the paper [2], which he defined as a rack of changing tooth pitch and pressure angles; Litvin and his team made a strong contribution to the research about face gears on the basis of their predecessors' research. His book [3] gave in-depth research about the surface of the face gear in terms of the gear geometry and meshing principle; Ji et al and Zhu et al. did a lot of research on face gears in the field of tooth surface contact analysis, strength, coincidence degree theory, etc. [4]; Lin et al. were the first to propose a non-circular curved face gear and explored its tooth profile analysis, machining simulation, measurement, etc. and this study made significant achievements. To date there has been little research about the tooth profile of non-circular curved face gears [5] and [6].

The error of the tooth profile will not only impact on the instantaneous transmission accuracy but also cause plastic deformation on the tooth surface of intermeshing gear. There exist some methods for using the numerical method to solve the gear tooth profile, for instance, Xia et al., Li et al. and Tong et al. calculated the tooth profile of a bevel gear using the numerical method which was based on the spherical coordinates [7] to [9]. In the field of gear measurement, Guenther et al. and Zhang et al. put forward some new theories and methods of measuring and analyzing gears [10] to [12]. But, at present, there is no practical way of using the numerical method to solve the tooth profile of non-circular curved face gear. This paper presents a new general numerical method used to calculate the tooth profile of a non-circular curved face gear. This method will serve as an important reference basis in the field of modeling, processing, analyzing errors of measurement, and so forth.

1 PARAMETERS OF THE CURVE
IN THE CYLINDRICAL COORDINATE SYSTEM

The non-circular curved face gear is a kind of cylindrical gear. In order to describe and calculate the parameters of the gear more accurately, this paper prepared a study of the angle and the expansion of the curve under the cylindrical coordinate system.

*Corr. Author's Address: Chongqing University, The State Key Laboratory of Mechanical Transmission,
Shapingba District sand 174 Center Street, Chongqing, China, linchao@cqu.edu.cn
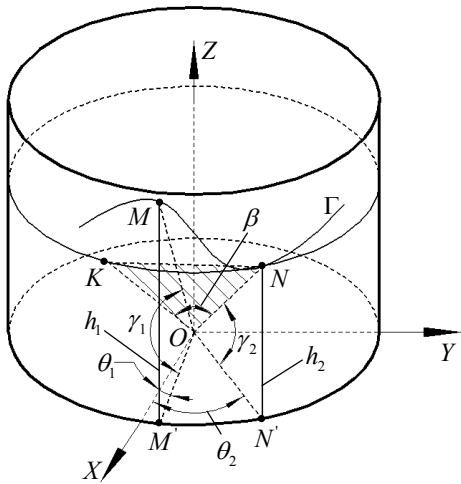
Fig. 1. *Parameters of the curve in the cylindrical coordinate system*

As shown in Fig. 1, $O-XYZ$ is the cylindrical coordinate system, Γ is one curve on the cylindrical surface, M and N are any two points on the curve. θ is the rotation angle which is from the positive X axis to the point. h is the distance between the point and the bottom surface, γ is the central angle of the point on the curve, R is the cylindrical radius.

1.1 Basic Description of the Curve

Assume that the equation of any curve is:

$$\Gamma = \begin{pmatrix} R\cos\theta & R\sin\theta & h(\theta) \end{pmatrix}. \qquad (1)$$

The arc length between points M and N is:

$$L_{\widehat{MN}} = \int_{\theta_1}^{\theta_2} \sqrt{R^2 + h'^2(\theta)}\, d\theta, \qquad (2)$$

where $h'(\theta)$ is the derivative of $h(\theta)$.

The central angle of one point on the curve can be defined as the angle between the line which links that point to the center of the circle in the bottom surface and the bottom surface. According to the geometric relationship the formula is:

$$\gamma = \arctan\frac{h(\theta)}{R}. \qquad (3)$$

1.2 Expansion of the Curve

The line linking all points on the curve to the center of the circle in the bottom surface will compose a conical surface. As shown in Fig. 1, there are countless tangent planes through point N. However, there exists a unique tangent plane that is vertical to the Z axis. There exists one point K on the line intersected by

the tangent plane and the cylindrical surface where $L_{\widehat{MN}} = L_{\widehat{NK}}$. At the same time the plane OKN is an expansion of the plane OMN. To solve Eq. (2), we get:

$$L_{\widehat{NK}} = L_{\widehat{MN}} = \int_{\theta_1}^{\theta_2} \sqrt{R^2 + h'^2(\theta)}\, d\theta. \qquad (4)$$

Thus the expansion angle β corresponding to the curve MN is:

$$\beta = \frac{1}{\sqrt{R^2 + h^2(\theta)}} \int_{\theta_1}^{\theta_2} \sqrt{R^2 + h'^2(\theta)}\, d\theta. \qquad (5)$$

2 PITCH CURVE OF THE NON-CIRCULAR CURVED FACE GEAR

2.1 Equation of the Pitch Curve

According to the meshing relationship of the non-circular curved face gear pair, a coordinate system can be established.
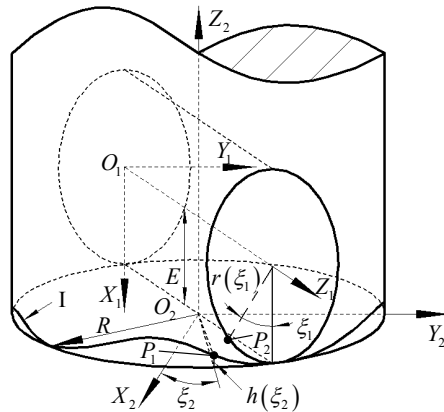
Fig. 2. *Meshing coordinate of the non-circular curved face gear*

As shown in Fig. 2, the axis of the non-circular gear is orthogonal to axis of the non-circular curved face gear. As shown in Fig. 2, $O_1-X_1Y_1Z_1$ is the fixed coordinate system of the non-circular gear. $O_2-X_2Y_2Z_2$ is the fixed coordinate system of the non-circular curved face gear. The point P_1 is on the pitch curve of non-circular gear and the point P_2 is on the pitch curve of non-circular curved face gear. When P_1 coincides with P_2, the non-circular gear turns at an angle of ξ_1, and the non-circular curved face gear turns at an angle of ξ_2. The radius of the pitch curve of the non-circular curved face gear is R, and the radius vector of the non-circular gear is $r(\xi_1)$. Under the conditions of Fig. 2, the distance between the axis of the non-circular gear and the bottom surface of

the face gear is E. I is the pitch curve of non-circular curved face gear.

According to the theory of non-circular gears, the equation for the pitch curve of the non-circular gear is:

$$r(\xi_1) = \frac{a(1-e^2)}{1-e\cos(n_1\xi_1)}, \qquad (6)$$

where, ξ_1 is the polar angle of the elliptic gear, a is half of the longer axis of the ellipse, e is the eccentricity of the ellipse, n_1 is the order of the non-circular gear.

When the parameters in Eq. (6) were chosen as follows: $a = 35$ mm, $e = 0.1$ and n_1 changes from 1 to 4. The pitch curve of the non-circular gear can be shown in Fig. 3.
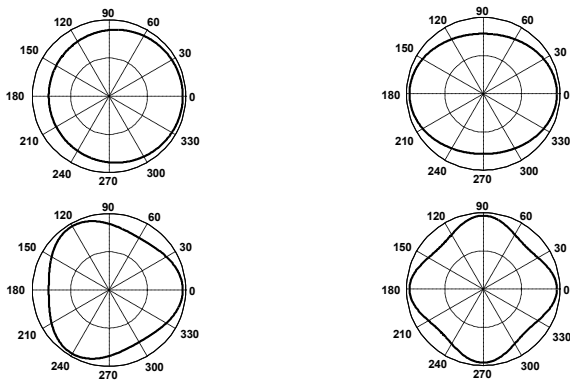
Fig. 3. *Impact of n_1 on the pitch curve of the non-circular gear*

In the meshing process of the non-circular gear and non-circular curved face gear, the center distance is fixed. From the geometric relationship shown in Fig. 2, Eq. (7) is correct at any point in time.

$$E = h(\xi_2) + r(\xi_1) = a + ae, \qquad (7)$$

where, $h(\xi_2)$ is the distance between the point on the pitch curve and the bottom surface when the non-circular face gear turns an angle ξ_2.

By substituting Eq. (6) and Eq. (7) into Eq. (1), the pitch curve of the non-circular curved face gear can be obtained.

$$r_2 = \begin{cases} x = R\cos\xi_2 \\ y = R\sin\xi_2 \\ z = h(\xi_2) = E - r(\xi_1) \end{cases}, \qquad (8)$$

where,

$$R = \frac{n_2}{2\pi}\int_0^{\frac{2\pi}{n_1}} r(\xi)\,d\xi, \quad \xi_2 = \int_0^{\xi_1}\frac{1}{i_{12}}d\xi = \frac{1}{R}\int_0^{\xi_1} r(\xi)\,d\xi,$$

n_1 is the order of the non-circular gear, n_2 is the order of non-circular curved face gear, i_{12} is the transmission ratio of the non-circular curved face gear pair and $i_{12} = R / r(\xi_1)$.

By substituting the equations above into Eq. (8), the pitch curve of the non-circular curved face gear can be obtained.

$$r_2(\xi_2) = \begin{cases} x = \frac{n_2}{2\pi}\cos\xi_2\int_0^{\frac{2\pi}{n_1}} r(\xi)\,d\xi \\ y = \frac{n_2}{2\pi}\sin\xi_2\int_0^{\frac{2\pi}{n_1}} r(\xi)\,d\xi \\ z = h(\xi_2) = E - r(\xi_1) \end{cases}. \qquad (9)$$

2.2 Tooth Modulus Angle of the Pitch Curve Plane

As shown in Fig. 4, based on the method of the expansion of the curve, tooth 1 and tooth 2 represent any 2 teeth on the pitch curve of the non-circular curved face gear. Point M and point N are the points on the right tooth profile of tooth 1 and tooth 2. There is a complete tooth profile between M and N. By expanding the tooth profile on the tangential circle of the pitch curve, the point K on the tangential circle can be obtained. When the arc length of $\overset{\frown}{MN}$ is equal to $\overset{\frown}{KN}$, the plane OKN is the expansion plane of the one tooth profile.

Fig. 4. *Tooth modulus angle of the non-circular curved face gear*

When the angle $\beta = \pi\beta_m$, β_m is the modulus angle of the tooth. The tooth profile of the non-circular curved face gear changes when the direction of the tooth width changes and so does the modulus angle.

2.3 Addendum Angle and Dedendum Angle

As shown in Fig. 5, the addendum line, pitch curve and dedendum line of the non-circular curved face gear are on the cylindrical surface Π. The tangential plane through the center point O of the bottom surface intersects with the addendum line, pitch curve and dedendum line at points M, P and N. $MN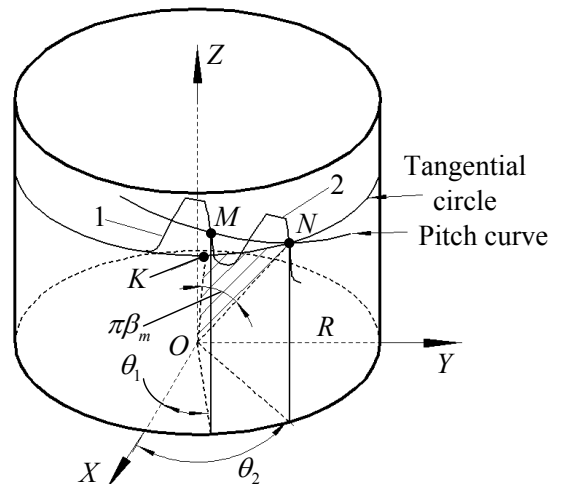$ is the tangent section on the cylindrical surface. Angles MOP and PON are defined as the addendum angle and the dedendum angle. And,

$$\begin{cases} \alpha_a = h_a^* \cdot \beta_m \\ \alpha_f = \left(h_a^* + c^*\right)\beta_m \end{cases}, \tag{10}$$

where, h_a^* is the addendum coefficient, c^* is the dedendum coefficient. β_m is the modulus angle.

So the addendum and dedendum of the non-circular curved face gear are:

$$\begin{cases} h_a = R\tan\left(\gamma + \alpha_a\right) \cdot h\left(\xi_2\right) \\ h_f = R\tan\left(\gamma - \alpha_f\right) \cdot h\left(\xi_2\right) \end{cases}, \tag{11}$$

where, γ is the center angle, R is the radius of the pitch curve of non-circular curved face gear, α_a is the addendum angle of non-circular curved face gear, and α_f is the dedendum angle of non-circular curved face gear.
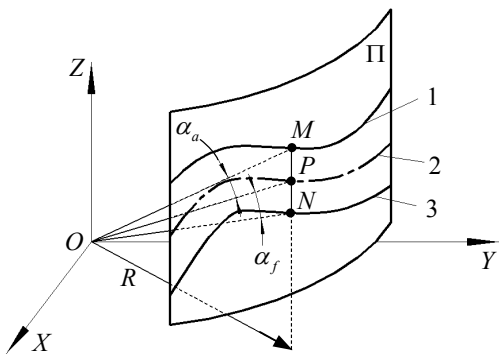
Fig. 5. *Addendum angle and dedendum angle (1 addendum line, 2 pitch curve, and 3 dedendum line)*

3 USING THE NUMERICAL METHOD TO SOLVE TOOTH PROFILE

The fundamental theory of the numerical method in solving the tooth profile of non-circular curved face gear is derived from the generating process of the non-circular curved face gear. The generating process is shown in Fig. 6.
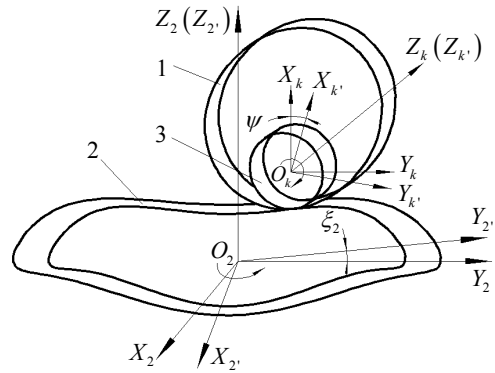
Fig. 6. *Coordinate system of generating process*

As shown in Fig. 6, $O_k-X_kY_kZ_k$ is rigidly connected to the frame of the cutting machine. $O_{k'}-X_{k'}Y_{k'}Z_{k'}$ is rigidly connected to the cutter. Likewise $O_2-X_2Y_2Z_2$ is rigidly connected to the frame of the cutting machine. $O_{2'}-X_{2'}Y_{2'}Z_{2'}$ is rigidly connected to the non-circular curved face gear.

According to the principle of gear engagement, the transformation matrix from $X_{kk'}$ to $M_{2'2}$ can be derived as:

$$M_{2'k'} = M_{2'2}M_{2k}M_{kk'} =$$
$$= \begin{bmatrix} \sin\psi\sin\xi_2 & \cos\psi\sin\xi_2 & -\cos\xi_2 & R\cos\xi_2 \\ \sin\psi\cos\xi_2 & \cos\psi\cos\xi_2 & \sin\xi_2 & -R\sin\xi_2 \\ \cos\psi & -\sin\psi & 0 & h\left(\xi_2\right) \\ 0 & 0 & 0 & 1 \end{bmatrix}, \tag{12}$$

where, ψ is the rotating angle of cutter when the non-circular curved face gear rotates at an angle of ξ_2.

The rotation angle of the cutter can be obtained from the processing geometric relationships.

$$\psi = \frac{\pi}{2} - \xi_1 - \arctan\left(\frac{r\left(\xi_1\right)}{r'\left(\xi_1\right)}\right) +$$
$$+ \frac{\int_0^{\xi_1} \sqrt{r^2\left(\xi\right) + r'^2\left(\xi\right)}\,d\xi}{r_k}, \tag{13}$$

where $r'(\xi)$ is the derivative of $r(\xi)$ and r_k is the radius of the pitch curve of cutter gear.

3.1 Equation of the Equidistant Curve of the Pitch Curve

The equation of the normal equidistant curve can be derived from the pitch curve equation of the non-circular curved face gear.

In Fig. 7, curves 1, 2, 3 stand for the expansion of addendum line, pitch curve and dedendum line of a non-circular curved face gear, respectively. P_a is the intersection of the addendum line and the normal line

of the pitch curve through point P. P_f is the intersection of the dedendum line and the normal line of the pitch curve through point P. η is the angle of the normal and vertical direction and therefore η can be expressed as:

$$\eta = \arctan\left(\frac{en_1 \sin(n_1\xi_1)}{1 - en_1 \cos(n_1\xi_1)}\right). \quad (14)$$

Assuming that there are n normal equidistant curves between the addendum line and the dedendum line. The parametric equations of $n/2$ equidistant curves from the pitch curve to the addendum line and another $n/2$ equidistant curves from the dedendum line to the pitch curve can be derived from Eq. (9).

$$\begin{cases} x_1 = R\cos\left(\xi_2 - \dfrac{2t_1 h_a \sin\eta}{nR}\right) \\ y_1 = R\sin\left(\xi_2 - \dfrac{2t_1 h_a \sin\eta}{nR}\right), \\ z_1 = h(\xi_2) + \dfrac{2t_1 h_a}{n}\cos\eta \end{cases} \quad (15)$$

$$\begin{cases} x_2 = R\cos\left(\xi_2 - \dfrac{2t_2 h_f \sin\eta}{nR}\right) \\ y_2 = R\sin\left(\xi_2 - \dfrac{2t_2 h_f \sin\eta}{nR}\right), \\ z_2 = h(\xi_2) + \dfrac{2t_2 h_f}{n}\cos\eta \end{cases} \quad (16)$$

where, n is the number of the normal equidistant curves. The t_1 and t_2 represent respectively the $t_1 - th$ equidistant curve from the pitch curve to addendum line and the $t_2 - th$ equidistant curve from the pitch curve to dedendum line respectively. When $t_1 = n/2$, it is the addendum line. When $t_2 = n/2$, it is the dedendum line.
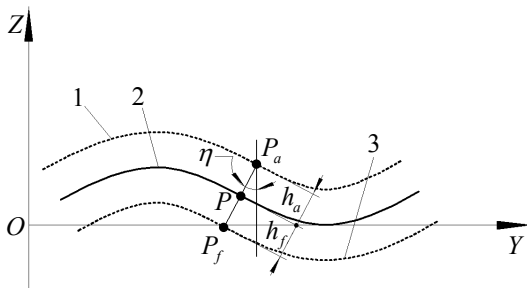
Fig. 7. *Planimetric pitch curve of non-circular curved face gear*

3.2 Using the Numerical Method to Solve the Tooth Profile

The tooth profile of the non-circular curved face gear can be derived by building the equation of the normal equidistant curve of the non-circular curved face gear using the method above. During the process, the intersection is at a given point if it satisfies the engagement conditions when the cylindrical cutter tooth profile associates with the equidistant curve of the pitch curve of the non-circular curved face gear.

According to mechanical principles, the tooth profile equation of an involute cylindrical gear cutter is [13]:

$$\begin{cases} x_k = \pm r_b \left[\sin(\theta_{ko} + \theta_k) - \theta_k \cos(\theta_{ko} + \theta_k)\right] \\ y_k = -r_b \left[\cos(\theta_{ko} + \theta_k) + \theta_k \sin(\theta_{ko} + \theta_k)\right], \quad (17) \\ z_k = u_k \end{cases}$$

where $\pm$ stands for left or right tooth profile of the cutter gear. r_b is the radius of the base circle, θ_k is the angle of any point on the involute, θ_{ko} is the angle from the involute-starting point to the center line of the gullet, $\theta_{ko} = \pi/2z + inv\alpha_k$, u_k is the parameter in the direction of tooth width and α_k is the pressure angle of the cutter gear.

When u_k is determined, the tooth profile of the cutter gear can be calculated by the software of Matlab. According to the coordinate transformation equation $P^{2\prime} = M_{2\prime k\prime} P^{k\prime}$, the tooth profile of the cutter gear is transferred to the following coordinates of the non-circular curved face gear. Thus, the intersections are calculated through the equations of the line of the points obtained above and the equidistant curve equation of the pitch curve of the non-circular curved face gear.

As shown in Fig. 8a, the left tooth profile of the cutter has four points, which equidistant from one another. $P_1^{2\prime}, P_2^{2\prime}, P_3^{2\prime}, P_4^{2\prime}$ are obtained by transforming the points to the coordinates $O_{2\prime} - X_{2\prime} Y_{2\prime} Z_{2\prime}$. Three lines can be obtained by linking the adjacent points. Intersections are calculated though the equations of the lines and equidistant curves.

The gear pair can be obtained through generating process. There also exist intersection points where the tooth profile of the cutter intersects with equidistant curves when the tooth space is processed. These points of tooth profile can be verified using the meshing condition. According to the principle of gear engagement, the points of the tooth profile of the non-circular curved face gear must satisfy the meshing

equation. So the intersection points obtained above should satisfy the meshing equation [1]:

$$\overline{N} \cdot \vec{v}_{2k} =$$
$$= r_b + \cos(\zeta - \lambda)\sqrt{r^2(\xi_1) + r_k^2 - 2r_k r(\xi_1)\sin\mu} -$$
$$- i_{21}(R + u_k)\cos\zeta = 0, \qquad (18)$$

where $\overline{N}$ stands for the normal line of cutter tooth surface and $\vec{v}_{2k}$ stands for the relative velocity of the cutter and the non-circular curved face gear. These two parameters need to be expressed in the same coordinate system. As shown in Fig. 8b $r_b = r_k\cos\alpha_k$ and $\zeta = \psi + \xi_1 - \theta_k - \theta_{ko}$.

Finally the points that satisfy Eq. (18) are on the tooth profile.

a)

b)
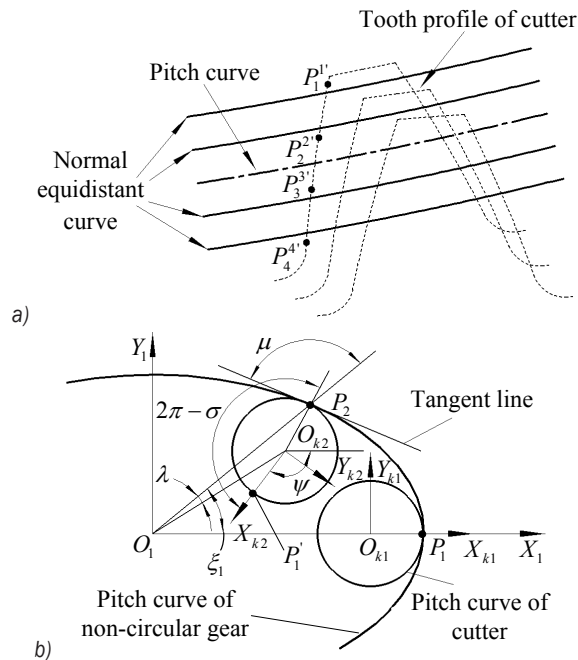
Fig. 8. *Numerical method for solving the tooth profile; a) intersection of the tooth profile and normal equidistant curves and b) space location of the gear shaper cutter*

3.3 Examples of Calculation

The 4-order non-circular curved face gear is processed using an involute cylindrical gear cutter where the parameters are the tooth number $z = 12$, the pressure angle $\alpha_k = 20°$, and the module $m = 4$. The gear pair is shown in Fig. 9.

As shown in Fig. 10a, according to the principle of using the numerical method to solve the tooth profile [10] to [12], the u_k is divided in accordance with

a tooth width of 72.5 mm, 74.5 mm, 76.5 mm, 78.5 mm, 80.5 mm. 5 equidistant curves used to divide the tooth are distributed 1.5 mm from one another along the tooth depth direction. The middle one of the 5 curves is coincide with the pitch curve.
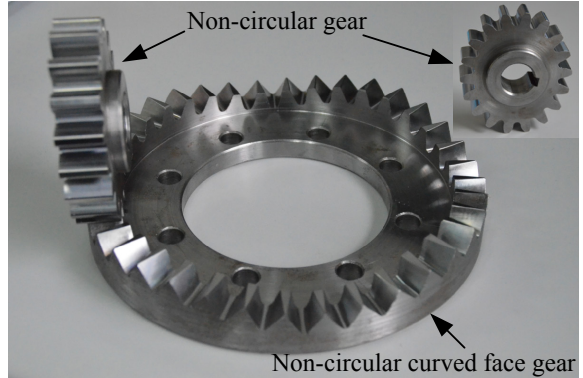
Fig. 9. *Material object of non-circular curved face gear*

Here we calculate the coordinate value of the left tooth surface of tooth 1. The results of the mesh generation are shown in Fig. 10b. The coordinate values are shown in Table 1.

a)

b)
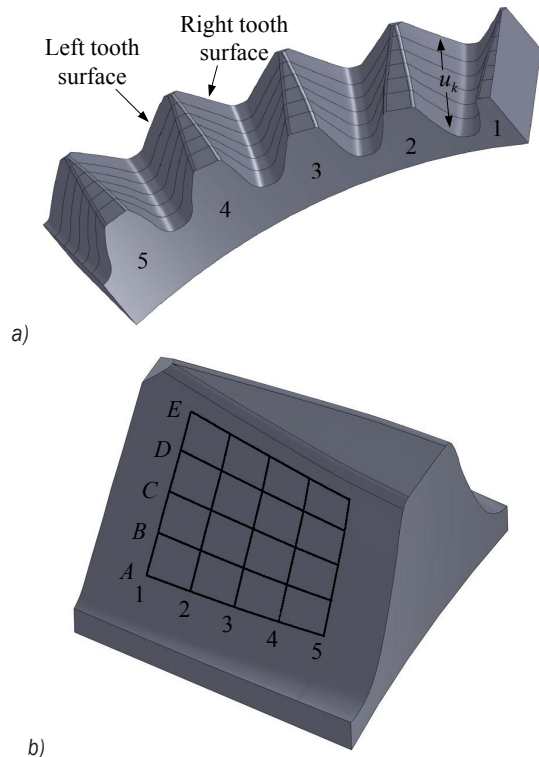
Fig. 10. *Division of measurement grids; a) mesh generation of tooth depth direction, and b) node number on tooth 1*

Table 1. *Coordinate values of theoretical points on the left surface of tooth 1 in [mm]*

	1	3	5
E	-80.49168, -1.13698, 3	-76.48175, -1.66847, 3	-72.46920, -2.11100, 3
C	-80.43873, -3.14385, 0	-76.43156, -3.23707, 0	-72.42771, -3.23691, 0
A	-80.32150, -5.35782, -3	-76.32929, -5.10585, -3	-72.34882, -4.67954,-3

3.4 Measurement of Non-Circular Curved Surface Gears

As shown in Fig. 11, the non-circular curved face gear was measured by the contour scanning software of a German Klingelnberg P26 automatic CNC controlled gear measuring center. Since each tooth profile in one cycle on the gear is different, contour scanning should be used as the measuring.
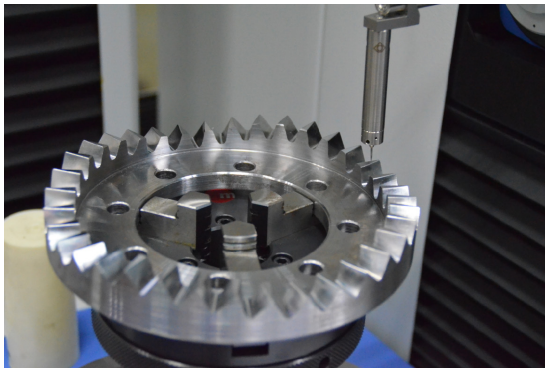
Fig. 11. *Profile measurement of the non-circular curved face gear*

Table 2. *Coordinate values of the measured points on the left surface of tooth 1 in [mm]*

	1	3	5
E	-80.477, -1.138, 3	-76.484, -1.661, 3	-72.459, -2.105, 3
C	-80.441, -3.132, 0	-76.434, -3.224, 0	-72.419, -3.227, 0
A	-80.323, -5.369, -3	-76.323, -5.106, -3	-72.349, -4.667, -3

According to the measurement and theoretical calculation process, the radius of tooth width, which is the motion trajectory of the probe, is the same as the one calculated above. The coordinate values of the grid nodes on the left tooth surface of tooth 1

are obtained using the measurement points from the neighboring space of the theoretical point from the measured data. The specific values are shown in Table 2.

3.5 Error Analysis of the Tooth Profile

Since there are errors in the actual processing, measurement and in the precision of the numerical method, there also exist errors between the measured values and the theoretical values.

Assuming that the normal distance between the measured point and the theoretical point is the normal error Δd, which is used to measure the deviation between two points. According to the following equation [3]:

$$\Delta d = \left(\vec{R}_m^* - \vec{R}_m\right) \cdot \vec{n}_m , \qquad (19)$$

where $\vec{R}_m^*$ is the coordinate value of the measured points, $\vec{R}_m$ is the coordinate value of the theoretical points and $\vec{n}_m$ is the normal direction of the tooth surface.

The deviation values are obtained by calculating for a real example. The results are shown in the Fig. 12.
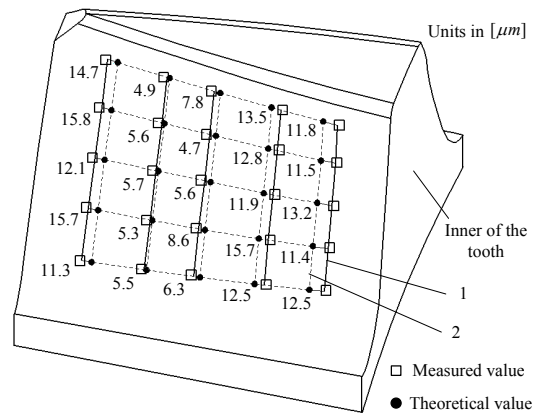
Fig. 12. *Error distribution (1 measured value grid, and 2 theoretical value grid)*

The normal deviation value is in the range of 5 μm to 16 μm. The precision of the deviation value satisfies the requirements of GB/T 10095.1-2001 precision class grade 6-7, and meets engineering demands. Therefore the numerical method of calculating tooth profiles has been shown to be accurate.

4 CONCLUSION

In the article, a new kind of gear was generated and geometric and mathematical models were established for this gear. A numerical method used to calculate the tooth profile of the non-circular curved face gear was developed. The correctness of the method was examined by an experiment. The results of the performed research allow the following conclusions to be drawn:

a) The relevant parameters of arbitrary curves were calculated in terms of the cylindrical coordinate system. The parametric equations of the pitch curve of the non-circular curved face gear and the normal equidistant curve equation were obtained.

b) The tooth profile of the non-circular curved face gear in the tooth width direction was obtained by changing the point on the tooth profile of the cutter to the coordinate system of the non-circular curved face gear through the method of coordinate conversion and where the intersection with its pitch curve and the normal equidistant curve occurs.

c) The error of the tooth profile between the theoretical calculations and the actual measurements was analyzed. The results showed that using the numerical method to solve the tooth profile of a non-circular curved face gear high precision and good universality. This calculation method will be of service in the field of error analysis of the tooth surface, accuracy assessment of tooth surface and manufacture, and so on.

5 ACKNOWLEDGEMENTS

6 REFERENCES

[1] Hai, G. (2012). *Transmission Design and Characteristic Analysis of Orthogonal Non-circular Face Gear Drive*. MSc Thesis, Chongqing University, Chongqing, p. 7-24. (in Chinese)

[2] Buckingham, E. (1988). *Analytical Mechanics of Gears*. Dover Publication, New York, p. 6-32.

[3] Litvin, F.L. Faydor, L. (2004). *Gear Geometry and Applied Theory*. Cambridge University Press, New York, p. 484-518, **DOI:10.1017/CBO9780511547126**.

[4] Guanghu, J., Rupeng, Z., Heyun, B. (2010). Nonlinear Dynamical Characteristics of Face Gear Transmission System. *Journal of Central South University (Science and Technology)*, vol. 41, no. 5, p. 1807-1813. (in Chinese)

[5] Chao, L., Shasha, L., Hai, G. (2014). Design and 3D modeling of orthogonal variable transmission ratio face gear. *Journal of Hunan University (Natural Sciences)*, vol. 41, no. 3, p. 49-55, **DOI:10.3969/j.issn.1674-2974.2014.03.009**. (in Chinese)

[6] Chao, L., Hai, G., Ning, N., Qinlong, Z., Lei, Z. (2013). Geometry design, three-dimensional modeling and kinematic analysis of orthogonal fluctuating gear ratio face gear drive. *Proceedings of the Institution of Mechanical Engineers*, vol. 227, no. 4, p. 779-793, **DOI:10.1177/0954406212453382**.

[7] Jiqiang, X., Yuanyuan, L., Chunming, G., Jiangbin, S. (2008). Noncircular bevel gear transmission with intersecting axes. *Journal of Mechanical Design*, vol. 130, no. 5, p. 054502, **DOI:10.1115/1.2885510**.

[8] Jiangang, L., Xutang, W., Shimin, M., Jingliang, H. (2005). Numerical computation of tooth profile of noncircular gear. *Journal of Xi'an Jiaotong University*, vol. 39, no. 1, p. 75-78. **DOI:10.3321/j.issn:0253-987X.2005.01.018**. (in Chinese)

[9] Ting, T., Fangyan, Z., Ke, S., Bing, Y. (2013). Non-circular gear teeth profile numeric method based on normal tooth profile. *Journal of Wuhan University of Technology (Transportation Science & Engineering)*, vol. 37, no. 3, p. 652-654, **DOI:10.3963/j.issn.2095-3844.2013.03.048**. (in Chinese)

[10] Guenther, A., Kniel, K., Härtig, F., Lindner, I. (2013). Introduction of a new bevel gear measurement standard, *CIRP Annals - Manufacturing Technology*, vol. 62, no. 1, p. 515-518, **DOI:10.1016/j.cirp.2013.03.083**.

[11] Guenther, A. (2011). Interpretation of bevel gear topography measurements. *CIRP Annals - Manufacturing Technology*, vol. 60, no. 1, p. 551-554, **DOI:10.1016/j.cirp.2011.03.060**.

[12] Jinliang, Z., Zongde, F., Xuemei, C., Xiaozhong, D. (2007). The modified pitch cone design of the hypoid gear: manufacture, stress analysis and experimental tests. *Mechanism and Machine Theory*, vol. 42, no. 2, p. 147-158, **DOI:10.1016/j.mechmachtheory.2006.09.008**.

[13] Yanan, W. (2013). *Research on Hobbing Method of Face Gear*. MSc Thesis, Harbin Institute of Technology, Harbin, p. 13-15. (in Chinese)

Three-Dimensional Characterization of Concrete's Abrasion Resistance Using Laser Profilometry

Dominik Kozjek[1] – Urban Pavlovčič[1] – Andrej Kryžanowski[2] – Jakob Šušteršič[3] – Matija Jezeršek[1,*]

[1] University of Ljubljana, Faculty of Mechanical Engineering, Slovenia
[2] University of Ljubljana, Faculty of Civil and Geodetic Engineering, Slovenia
[3] IRMA Institute, Slovenia

This paper presents development of three-dimensional characterization of concrete abrasion using the ASTM C1138 test method, which simulates underwater abrasion. To this effect, a measuring system was designed based on laser triangulation with linear illumination of the surface measured. The system allows for contactless, quick and precise measuring of average wear and other topological characteristics dependent on the type of the tested concrete. Validation results show that the system's precision is better as conventional weighting method (<15 gram) and furthermore it allows us to analyze the spatial distribution of wear.
Keywords: concrete's wear, abrasion resistance, 3D measurement, laser triangulation

Highlights
- *Concrete's abrasion measurement is improved using laser profilometry.*
- *Depth of wear and relief of abrased surface are measured in 3D.*
- *Upgraded system has higher precision compared to the conventional method.*
- *Analysis of spatial distribution of the wear is enabled.*

0 INTRODUCTION

The damage of the concrete surface due to the abrasion of the bed load transported by the flowing water is one of the main problems to be addressed in the operation of hydraulic structures. The problem of concrete's abrasion resistance was given special attention in the construction of the Sava river hydropower plants. During the construction of the dams on the Sava, the quality and resistance of concretes to the abrasive action of waterborne particles was specified using standard and non-standard abrasion resistance test methods, and field tests, by conducting test plot measurements in the Vrhovo hydroelectric power plant spillways. From the abrasion resistance tests of the concretes used on the Sava River it was concluded that the ASTM C1138 was the most appropriate test method [1] and [2]. The test method is designed to simulate the abrasive action of waterborne particles [3] and [4]. Circulating water moves the steel grinding balls on the surface of a concrete sample, producing the desired abrasion effects (Fig. 1). The water velocity and agitation effect are not sufficient to lift the steel balls off the surface of the concrete sample to cause any significant impact action against the surface. The test method can only be used to determine the relative resistance of the material to the abrasion action of waterborne particles. The standard procedure of the investigation provides for the measurement of the wear of specimen surface at 12-hour intervals; the

total investigation time is 72 hours [5]. The result of the test is the average depth of wear expressed by the average volume of wear on the surface of the specimen in the duration of the test [6]. The method is highly selective in analysing poor-performance concretes. The Sava river dams' spillways are installed with high-performance concrete where the measured values fall within the measurement accuracy limits due to the extremely low wear rates. In an effort to increase method selectivity in high-performance concretes, the investigations to date included various modifications to the standard procedure, such as: intensifying water mixing in the container [7], extending the test duration [7] and [8], and studying the possibilities of increasing the accuracy of wear measurements by using a contact, three-dimensional coordinate-measuring machine (CMM) [8]. The standard procedure measures wear by weighing the specimen with an accuracy tolerance of 25 g [5], while general purpose CMMs achieve the volumetric uncertainty of 1 µm [9].

The measurements using the 3D meter provide both the data on the wear volume size and the worn surface relief. In fact, the relief image of the concrete specimen's surface wear facilitates interpretation of the physical processes characteristic of the device's functioning and the movement of steel balls during the test. The accuracy of such a procedure depends on the size of the point data acquisition and increases with the densification of data acquisition; on the

other hand, the procedure using contact, high lateral resolution is extremely time-consuming.
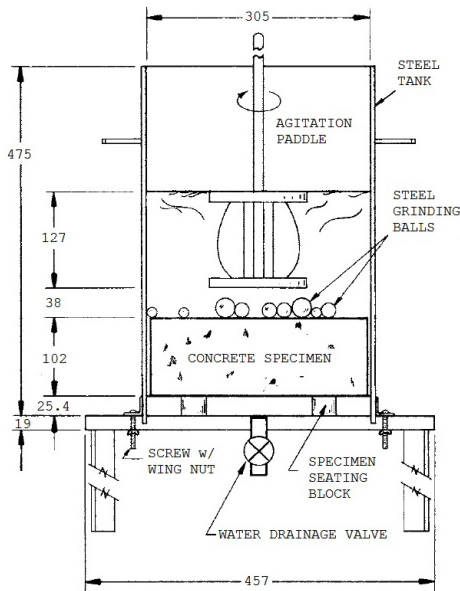
Fig. 1. *The test apparatus using the ASTM C1138 test method; all dimension are in mm* [3]
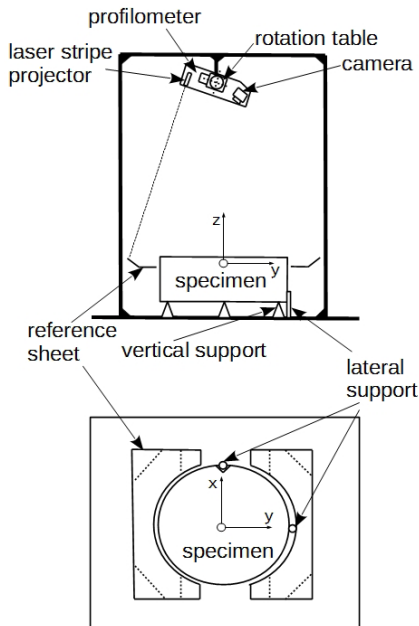
Fig. 2. *Experimental system for 3D measuring of concrete wear using laser triangulation*

In our study the method of measuring the specimen's surface wear was upgraded using a continuous 3D measurement based on laser triangulation and an advanced measurement analysis.

The advantage of three-dimensional profilometry against point acquisition is that it provides contactless, high-speed, and high-precision measurements. Because of the characteristics listed above, these methods can be used in geometry control of products with complex geometry [10] in medicine to monitor wound healing [11], regularity of breathing [12], foot shape [13] and [14], and for digitally archiving cultural heritage in 3D [15].

Below we describe the measuring system adapted to the requirements and needs of the ASTM C1138 test method, the measuring procedure, the analysis of measurements, the validation of the method in terms of repeatability of measurements, and the comparability of the results with those obtained using the standard prescriptive method.

1 MEASURING SYSTEM

The three-dimensional measuring system is based on the principle of laser triangulation [16], where the laser projector illuminates the surface along a line, while the camera aligned at a triangulation angle takes images of the illuminated surface. The shape of the surface is reflected in the laser contour curvature on the captured image. The entire surface is scanned while the profilometer rotates around the turntable axis (Fig. 2). The profilometer has an in-built camera with a sensor size of sensor size of $4.15\,mm \times 2.88\,mm$, pixel resolution of 752×480, and refresh rate of 64 Hz which allows for on-site processing of the captured image. The laser line projector allows for a line width of $< 0.1\,mm$, output power of $3.5\,mW$, and wavelength of $670\,nm$. The profilometer is positioned $800\,mm$ above the worn surface of the specimen. At this distance, the resolution is $0.66 \times 0.3\,mm^2$ in the X and Z directions. The rotation is performed via a turntable whose resolution is 0.6 arc minutes. This means that the resolution on the $800\,mm$ arm is about $0.14\,mm$ in the scanning direction. To measure a $500 \times 370\,mm^2$ surface, which corresponds to the specimen's surface, the profilometer must rotate by 26°. In doing so, the surface is measured in approx. 400,000 points over 8.2 seconds.

The system for measuring the wear of concrete specimens consists of a massive base plate onto which the stand with the laser profilometer and the reference sheet metal are attached (Fig. 2). The reference sheet metal is used for positioning and orienting the global coordinate system. This helps to compensate for any deformations of the laser profilometer stand due to thermal elongation, or due to any accidental impact

that could cause permanent displacement of the profilometer relative to the reference sheet metal.

The concrete specimen is a cylinder with a diameter of 295 mm and a height of 100 mm. Before the measurement, the specimen must be washed with a mild water jet and dried. Such a specimen is inserted into the measuring device and precisely positioned in the vertical direction with three point supports. Two lateral supports ensure repeatable positioning along the main coordinate axes in the horizontal plane (X-Y coordinates) and the rotation around the vertical axis (Z coordinate). In the C1138 test method the specimen's surface wear is measured in 12-hour test periods for a total of 72 hours, which is the full duration of the abrasion resistance test. In our study, the measurements of surface wear of the specimen were condensed by shortening the test periods to 3 h increments. The precision was also increased by performing a set of 10 stand-alone, independent measurements during each measurement period. This means that the specimen was reinserted into the measuring device. The final surface wear measurement per individual test period is the average value of all repetitions. The example of a three-dimensional concrete surface measurement and the reference sheet metal is shown in Fig. 3. The figure nicely illustrates the topography of the concrete surface and of the reference surface. The protrusions on the reference sheet metal are the heads of the mounting bolts.
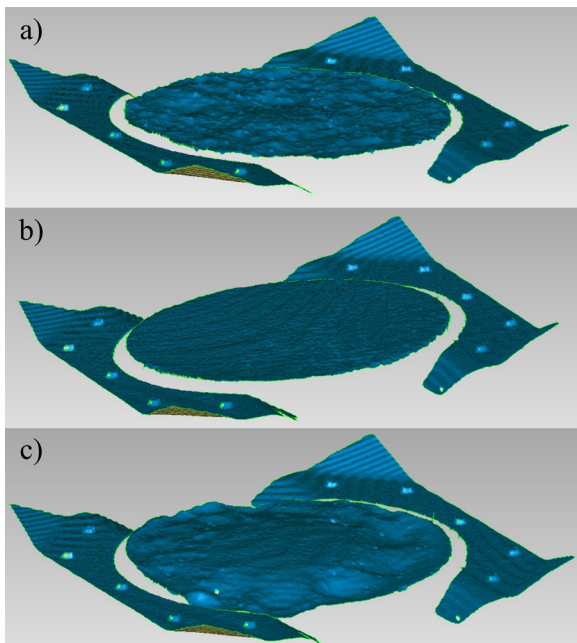
Fig. 3. *Examples of 3D measurements of concrete specimens; a) specimen with rubber aggregate, b) unworn specimen, and c) equally worn specimen*

2 PROCESSING OF MEASUREMENTS

The 3D measurements' processing procedure is schematically represented using a block diagram in Fig. 4. The testing of wear of concrete specimens takes a total of 72 hours, where the wear measurements using the abovementioned system are performed at 3-hour time increments. 10 repeated 3D measurement are performed and then averaged to improve the measuring accuracy at each time increment. The processing of measurements consists of the following steps: (1) spatial adjustment of all measurements according to the reference sheet metal; (2) calculation of the average shape based on repeated measurements; (3) calculation of wear over the entire surface, and (4) analysis of wear images, where the value and the position of the maximum wear, average wear on the chosen radius of the sample, and the total volume of the material lost are calculated. Steps (2) to (4) are carried out after each time increment, providing the time course of wear. These steps are described below.
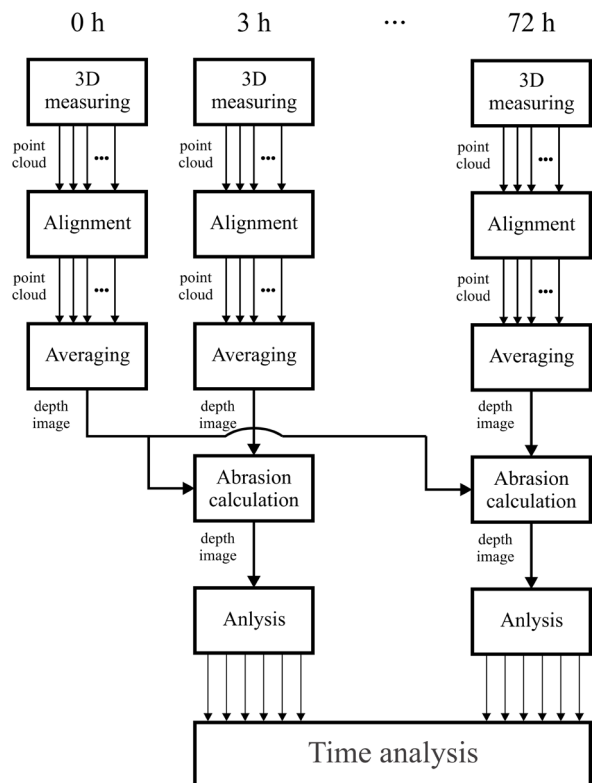
Fig. 4. *The block diagram of the characterization of concrete's abrasion based on 3D surface measurements*

The spatial adjustment is based on the minimization of the deviation between the first measurement of the reference sheet metal, and

the current measurement, where the deviation is calculated as the sum of squares of distances between the points along the Z axis. Only the points lying on the reference sheet metal are taken into account. Hence, this procedure makes up for any displacements of the profilometer relative to the reference sheet metal.
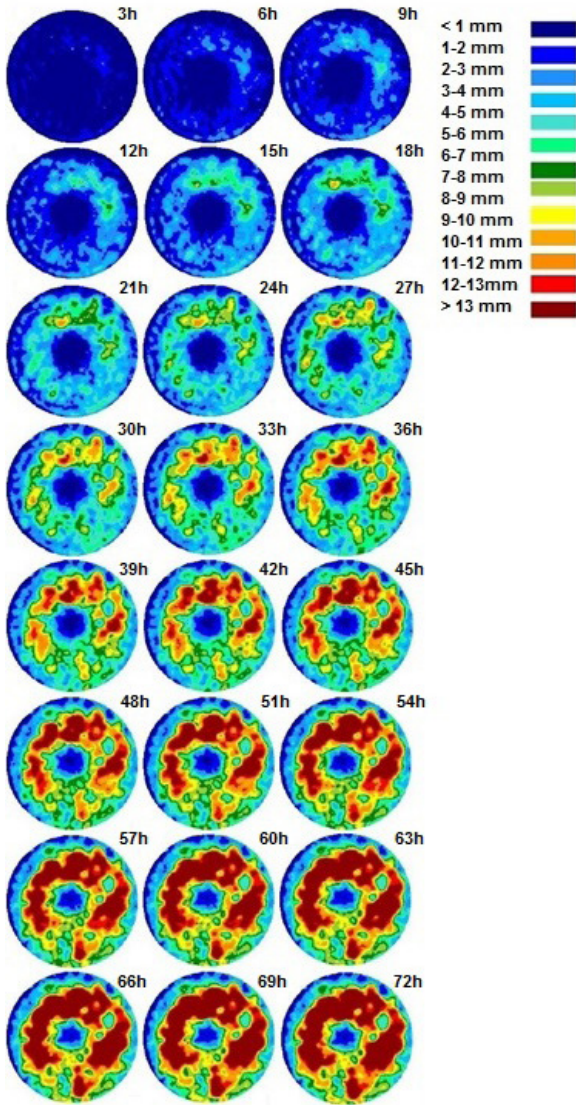
Fig. 5. *Color indication of increasing concrete's wear as a function of the time of wear*

The concrete surface's average 3D shape in the individual points is calculated in such a way that all the measurements that were performed at the same time increment are segmented in the horizontal plane (X-Y coordinates) to $2 \times 2\,mm^2$ square areas. The points within the individual areas are used to calculate the area's average height (Z coordinate), and the

standard deviation. In order to exclude statistically inconsistent points (outliers) we must calculate the difference between the height of the individual point and the average height. If the difference is more than 3-times the standard deviation, the point is excluded from the new calculation of the average height. Thus, we obtain a sequence of depth images which represent the shape of the concrete surface before the wear test and across the individual time increments of the abrasion resistance test. Notably, the depth images are aligned in the direction of the main X-Y coordinate axes.
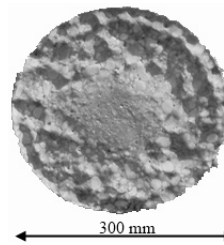
Fig. 6. *Photography of the concrete surface after 72 hours of the test*

a)

b)
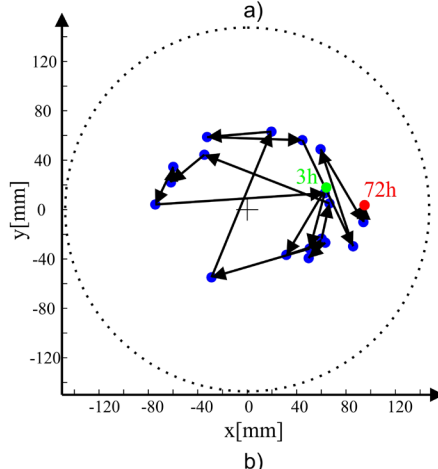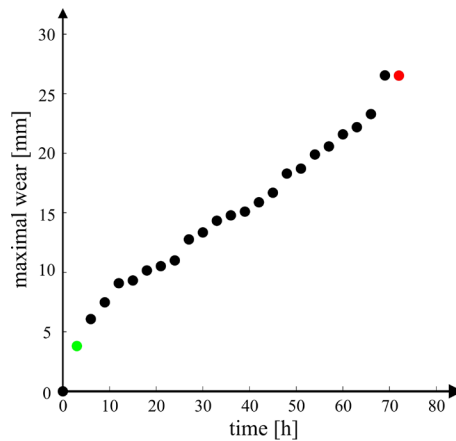
Fig. 7. *a) time course of maximum wear increase, and b) its location on the surface of the specimen*

This is followed by the calculation of surface wear, calculated as the difference of depth images of the specimen surface before the test, and the specimen surface in the individual time increments of testing. The example of the specimen's surface wear as a function of the duration of the abrasion resistance test is shown in Fig. 5, while the specimen after the completion of the test is shown in Fig. 6. The 3D illustration of the eroded surface gives considerably many more possibilities of interpreting the results of abrasion resistance measurements than the standard procedure, which only allows for qualitative interpretations of the damage to the surface based on photo documentation – such as position, depth, and the severity of wear. By contrast, the 3D measurement allows for a quantitative comparison of the results. An example of such analysis is shown in Fig. 7, where we analyzed the greatest depth of wear occurring on the surface of the specimen in the individual time increments of testing. Fig. 7a shows the time course of the increase of maximum wear, and Fig. 7b the position of the point where the wear was detected.

As seen in Figs. 5 and 6, surface wear is not uniform, but rather it changes with the distance from the center of the specimen. This can be explained with the operation mechanism of the abrasion resistance test using the ASTM C1138 test method. Due to the rotating agitation paddle in the container a potential vortex occurs as a combination of rotational and irrotational flows. Rotational flow occurs in the core of the vortex, limited by the operation area of the agitation paddle, while irrotational flow occurs outside of the vortex's core. The water's velocity in the core of the vortex increases directly proportionally to the distance from the axis of the container towards the rim, reaching its maximum at the outer rim of the container. In the area of the irrotational flow, the water's velocity decreases inversely proportionally to the distance from the core of the vortex towards the rim of the container where it reaches its minimum.

The wear propagation in radial direction shows Fig. 8, where the curves show the average wear of the specimen in the radial direction in the individual time increments. In the area of the paddle's operation, the wear of the concrete surface is smaller than that in the area of the irrotational flow where the damage to the surface increases over time, reaching its maximum approx. at the rim of the area of operation of the agitation paddle, which is, indeed, expected given that the water velocity in this area is the highest. The figure illustrates that initially the wear occurs approximately in the center of the irrotational flow area, gradually

nearing the inside edge of the area, which is reached after 72 hours of the apparatus's operation (Fig. 8).
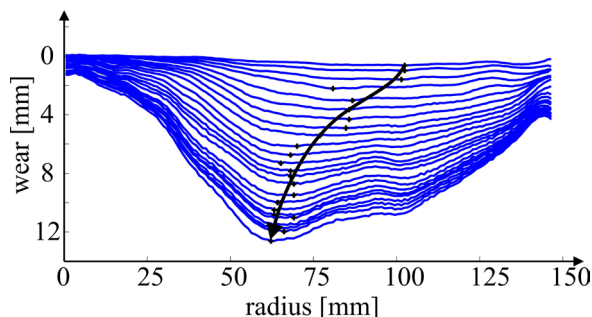
Fig. 8. Average wear in the radial direction of the specimen; the hatched arrow characterizes the wear progression over time

The volume of the material lost was determined in the last step of measurements' processing. The volume is calculated by integrating wear across the entire concrete surface. An example of the time course of the volume increase is shown in Fig. 9, which reveals the linear progression of the specimen wear up until approx. half of the test duration, followed by a gradual decrease of wear until the completion of the test.

The described method of measurement processing is implemented with stand-alone software that reads the series of 3D measurements from a working folder and automatically performs the steps described above. The final results are visually presented as a function of the time of wear, and stored into files as raster images and tables. The time of the measurements' analysis of the complete test, consisting of the results of measurements at 25 time increments or, including repetitions, 250 measurements, is approx. 5 minutes.
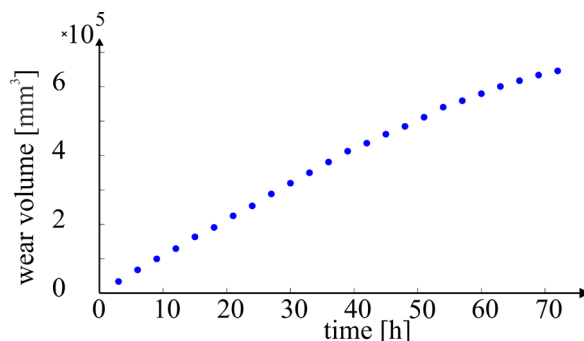
Fig. 9. Plot of wear volume increase versus time

3 VALIDATION

The precision of the measurement method was tested in two ways: (1) with assessment of repeatability, and (2) by comparison with the conventional weighing

method. In stage 1 we analyzed the repeatability of the measurement of the specimen surface at the same time of wear. To that end, we selected three specimens with typical worn surfaces (smooth, rough, and eroded surface – Fig. 3), and we repeated the measurement of the specimen surface 10 times, while each time the specimen was reinserted into the apparatus. First, all measurements were spatially adjusted, as described in the previous chapter, then the standard deviation in the vertical Z direction in individual points and the standard deviation of the average height of the entire surface were calculated.
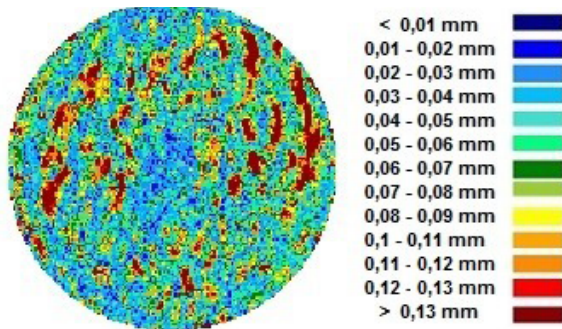
Fig. 10. *Standard deviation of the depth measurement across the surface; it is calculated for 10 repeated measurements*

Fig. 10 shows the standard deviation values in the individual points of the depth measurement for the case of the specimen with rough surface (example in Fig. 3a – concrete with rubber aggregate). It is apparent that at no point the standard deviation exceeds the value of 0.14 mm, which is more than

one size class less than the expected depth of wear during the individual time increments (Fig. 5). The reason for the relative variability in the standard deviation mainly lies in the limited resolution of the profilometer, and the positioning unreproducibility of the concrete samples in the cross-direction (X and Y).

The diagrams in Fig. 11 show the average height of the measured surface as a function of the consecutive repetition of measurement. It is apparent that the positioning in the vertical direction is another size class more precise, as the standard deviation of average heights is between 3 and 6 µm. The slope of the regression line also indicates that the average height is decreasing, i.e. by approx. 1 µm per measurement. The reason for this is probably that the contact area of the specimen is worn after each placement of the specimen on the point supports.

During the abrasion resistance test of concrete using the ASTM C1138 standard test method, the loss of material during the individual time increments was assessed by weighing. For this purpose, we used a scale with a measuring range up to 20 kg, and with an accuracy of ±1 g. The measured wear volumes, acquired using the 3D profilometer, were converted to mass of the material lost based on the known material characteristics of the specimens. The comparison results are given as the Bland-Altman plot in Fig. 12. The abscissa shows the average measurement values based on 3D measurements and weighing, and the ordinate the value differences between weighting and 3D measuring method. The plot reveals that the difference increases with the increase of wear: at the
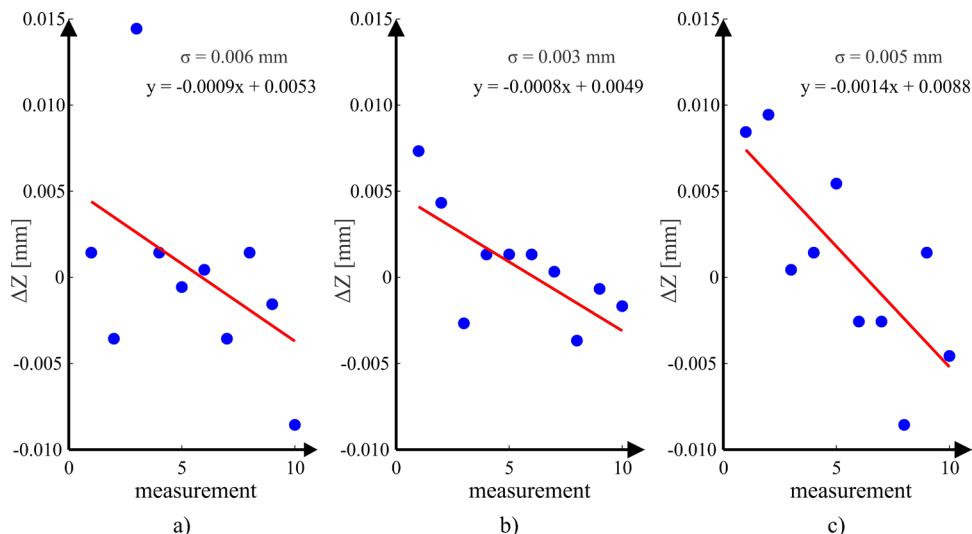
Fig. 11. *Average height of measured surfaces according to the consecutive measurement at the same duration of wear; a) specimen with rubber aggregate, b) unworn specimen, and c) equally worn specimen*

maximum wear of 1360 g it is approximately 15 g. According to our estimate, the systematic deviation is the consequence of the error in determining the diameter and density of the material in the volume-to-mass conversion of the material lost. If the mass of the material lost is converted into the average decrease of the surface height, the sample is on average worn by 10 mm, while the maximum height difference is 0.1 mm. We can conclude that the precision of the 3D method is completely comparable to the well-established method of weighing, while the 3D method also allows for topological characterization of abrasion.
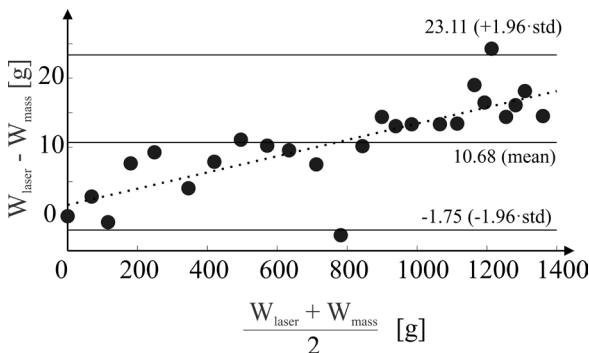
Fig. 12. *The comparison of wear measured using the laser profilometer (W_{laser}), and a scale (W_{mass})*

4 CONCLUSIONS

The paper demonstrates a new method of characterization of concrete's abrasion resistance based on laser 3D profilometry, and the analysis of the measured surfaces of concrete specimens as a function of the duration of wear. The method was developed for contactless, precise, and fast measurements compared to conventional methods. The entire measurement procedure (placement of the specimen and 3D measurement) takes approx. one minute. The measurement resolution is 0.66 mm, 0.14 mm, 0.3 mm in X, Y, and Z directions, respectively. The results of the measurements consist of three-dimensional images of surface wear, position, and size of maximum wear, average depth of wear on a specific radius of the sample, and the total volume of the material lost. All the data are measured as a function of wear duration. Repeatability tests of the measurement of the same concrete specimen show that it is approx. 0.005 mm. Compared to the weighing method, the results of average wear across the entire surface provide equivalent precision. There is a systematic bias (up to 15 g or 0.1 mm) due to the imprecisely determined

density of concrete. Based on this it may be argued that the method involving weighing can be replaced by the 3D measurements of wear. Moreover, the new method allows for the acquisition of data on the topography of the worn surface.

5 REFERENCES

[1] Kryžanowski, A., Mikoš, M., Šušteršič, J., Planinc, I. (2009). Abrasion resistance of concrete in hydraulic structures. *ACI Materials Journal*, vol. 106, no. 4, p. 349-356, **DOI:10.14359/56655**.

[2] Kryžanowski, A., Mikoš, M., Šušteršič, J., Ukrainczyk, V., Planinc, I. (2012). Testing of concrete abrasion resistance in hydraulic structures on the lower Sava river. *Strojniški vestnik - Journal of Mechanical Engineering*, vol. 58, no. 4, p. 245-254, **DOI:10.5545/sv-jme.2010.217**.

[3] ASTM C 1138-97 (2002) Standard test method for abrasion resistance of concrete (underwater method). *Annual Book of ASTM Standards*, vol. 04.02, ASTM, West Conshohocken.

[4] Kumar, G.R., Sharma, U.K. (2014). Standard test methods for determination of abrasion resistance of concrete. *International Journal of Civil Engineering Research*, vol. 5, no. 2, p. 155-162.

[5] Liu, T.C. (1981). Abrasion resistance of concrete. *Journal Proceedings – ACI*, vol. 78, no. 5, p. 341-350.

[6] Wu, C.H., Liu, Y.W., Huang, C.H., Yen, T., Hsu, T.H. (2010). Research on the abrasion erosion and impact resistance of fiber concrete. *Collected Papers on Building Technology*, 18th CIB World Building Congress, Salford.

[7] Kryžanowski, A. (2009). *Abrasion Resistance of Concrete on Hydraulic Structures*. PhD dissertation. University of Ljubljana, Faculty of Civil and Geodetic Engineering. (in Slovene)

[8] Horszczaruk, E. (2009). Hydro-abrasive erosion of high performance fiber-reinforced concrete. *Wear*, vol. 267, no. 1-4, p. 110-115, **DOI:10.1016/j.wear.2008.11.010**.

[9] Leach, R., Haycocks, J., Jackson, K., Lewis, A., Oldfield, S., Yacoot, A. (2001). Advances in traceable nanometrology at the National Physical Laboratory. *Nanotechnology*, vol. 12, no. 1, p. R1-R6, DOI:10.1088/0957-4484/12/1/201.

[10] Perdan, B., Bračun, D., Diaci, J., Možina, J. (2010). Online assessment of power transmission belt geometry by using laser triangulation and profile parameterisation. *The International Journal of Advanced Manufacturing Technology*, vol. 49, no. 1, p. 177-184, **DOI:10.1007/s00170-009-2378-z**.

[11] Kecelj-Leskovec, N., Jezeršek, M., Možina, J., Pavlović, M.D., Lunder, T. (2007). Measurement of venous leg ulcers with a laser-based three-dimensional method: Comparison to computer planimetry with photography. *Wound Repair and Regeneration*, vol. 15, no. 5, p. 767-771, **DOI:10.1111/j.1524-475X.2007.00300.x**.

[12] Povšič, K., Fležar M., Možina, J., Jezeršek M. (2012). Laser 3-D measuring system and real-time visual feedback for teaching and correcting breathing. *Journal of Biomedical Optics*, vol. 17, no. 3, p. 360041-360048, **DOI:10.1117/1.JBO.17.3.036004**.

[13] Novak, B., Možina, J., Jezeršek M. (2014). 3D laser measurements of bare and shod feet during walking.

Gait & Posture, vol. 40, no. 1, p. 87-93, **DOI:10.1016/j.gaitpost.2014.02.015**.

[14] Novak, B., Babnik, A., Možina, J., Jezeršek, M. (2014). Three-dimensional foot scanning system with a rotational laser-based measuring head. *Strojniški vestnik - Journal of Mechanical Engineering*, vol. 60, no. 11, p. 685-693, **DOI:10.5545/sv-jme.2014.1950**.

[15] Levoy, M., Pulli K., Curless, B., Rusinkiewicz, S., Koller, D., Pereira, L., Ginzton, M., Anderson, S., Davis, J., Ginsberg, J. (2000). The digital Michelangelo project: 3D scanning of large statues. *Proceedings of the 27th Annual Conference on Computer Graphics and Interactive Techniques*. ACM Press/Addison-Wesley Publishing Co, **DOI:10.1145/344779.344849**.

[16] Jezeršek, M., Možina, J. (2003). A laser anamorph profilometer. *Strojniški vestnik - Journal of Mechanical Engineering*, vol. 49, no. 2, p. 76-89.

Numerical Cooking for Pasteurized Soft Boiled Eggs

Marjan Jenko

University of Ljubljana, Faculty of Mechanical Engineering, Slovenia

The industrial preparation of pasteurized soft boiled eggs requires meticulous planning of the thermal process. Requirements on keeping the yolk liquid and on extinction of potential salmonella allow little leeway in the creation of this process. The variation of the eggs' properties adds to the complexity. Thermal simulation of heat transfer within an egg is needed to get correlation data between transient temperature distribution and the egg's dimensional and material properties. A fast simulator of conductive transient heat transfer with a fixed grid of cells is developed for this purpose. The motivation for achieving the highest simulation speed was the potential integration of a simulation tool for simulation based predictions into an embedded control system. The simulated volume is a cylinder. The simulated object (the egg) is defined within the cylinder. Simulation results are analysed and used in the creation of the thermal process which results in certified pasteurized soft boiled eggs. The presented approach to the design of transient simulation can be used for applications ranging beyond the transient thermal simulation of foods. It can be adapted for any transient simulation where the local temporal intensity of changes depends on gradients and the properties of the matter.
Keywords: fixed grid simulation, conductive heat transfer simulation, transient thermal simulation, Fourier's law of heat flow, pasteurized soft boiled eggs, foods processing

Highlights
- *The development of a faster than real-time transient thermal 2D simulation tool is presented in this paper.*
- *Faster than real-time simulation can be an integral part of a control system.*
- *The developed transient thermal simulation runs about 100 times faster than an equivalent commercial CFD simulation.*
- *The approach can be adapted for any transient simulation where the local temporal intensity of changes depends on gradients and on the properties of the matter.*
- *The test case is on sensitivity of temperature field dynamics to the dimensional and material properties of an egg.*
- *A unique patented thermal process for the production of pasteurized soft-boiled eggs is based on the results of the simulation.*

0 INTRODUCTION

Numerical methods of solving differential equations that describe real world events are just about as old as the differential calculus itself. In such problems it is not necessary to aim at absolute mathematical exactness, because theoretical results that exceed in accuracy the tolerances of the best available observational instrumentation are not needed. Thus, differentials may be substituted for finite differences. This reduces practically insolvable problems in analysis to finite numerical calculations that can be done by computer. Yet, even so, partial differential equations can be quite challenging, both to processing units and memory space. The general objective is to ensure the convergence of algorithms within the limitations of computers. The Finite Elements Method (FEM) has been developed to this end. It is a method where one adjusts to the given problem the sizes of the finite elements, making them as large as possible in regions of space where the relevant functions are very smooth and as small as necessary where they are not – for example, near sharp edges in boundary conditions. A disadvantage of the method of finite elements is the complexity of implementing it: not many engineers,

who may need it, can write their own. Moreover, general purpose commercial packages are never optimally adapted to a particular problem. However, optimal adaptation is essential in the battle between the steadily decreasing limitations of computers and our steadily increasing objectives.

Faced with a practical problem of designing an apparatus with conceptually new functionality for an industrial client, this author was considering different options for the control of a thermal process that would produce pasteurized soft boiled eggs. One of the considered options was the development of a faster than real time transient thermal simulator, which could add to the process control. Meshing would be replaced with a predetermined fixed grid of cells and iterative procedures of the simulated case would need to be heavily optimized for speed. The whole task ought to be feasible to even moderately proficient programmers. Writing a simulation program for the problem in question (heating of an egg in water) confirmed the feasibility speculation.

The basic aim in developing the simulation was to identify the correlation between an egg's spatial distribution of temperatures while being heated and the egg's dimensional and material properties. This

insight was needed firstly to decide on the viability of the new thermal process. Later the insight was essential in the design of the process and in the design of the control system.

Pasteurization is a delicate temperature-dependent process. It is different from sterilization where there are no active microorganisms left after the procedure. Pasteurization is aimed at a drastic decrease of the number of micro-organisms in foods – the reduction being in the range of multiple orders of magnitude. The remaining concentration of pathogens is supposed to be limited at such a low level that causing a disease is unlikely if foods are stored at a low enough temperature for a short enough time. In the case of eggs, one should be most concerned about a potential contamination with salmonella.

Different approaches have been studied and different procedures have been developed to decontaminate potentially contaminated eggs. A combination of temperature, time and possible additional stress is needed to decrease the live salmonella concentration to a harmless level. Pasteurization and dry heat are combined in [1] to destroy the bacteria. Refs. [2] to [4] define combinations of temperatures and times for pasteurization. Ref. [5] is about inactivating bacteria on the shell's surface by using temperature treatment. Other sources of energy have been studied for bacteria inactivation: Microwave heating [6], radio frequency (RF) energy [7], combination of pulsed electric fields and heat [8] and ionizing radiation [9].

To validate pasteurization, a thermometer is to be inserted into the coldest spot of the food. This point has to be at or above lowest pasteurization temperature for a shortest pasteurization time or longer [10]. The best protection against salmonella is processing foods at high temperatures. This is the reason why industrial preparation of eggs for breakfast and supper buffets in hotels and restaurants offer hard boiled and scrambled eggs (high temperature processing), but not soft boiled eggs (low temperature processing).

1 THEORY – PROTOTYPE PROBLEMS

While the final objective of the simulation project is to develop a fast interactive and potentially embedded simulator applicable to many practical problems, the development work is currently restricted to the conductive heating of an object. The specific model used is that of a cold egg being put in a pot of hot water. The simulator is to yield the temperature as the function of time for every point inside the egg – taking into account the different thermal properties of the

shell, of the white, of the yolk, and of the air pocket. At a subsequent stage of development, one could take into account the modifications of these properties during cooking, but it is important to realize that these modifications should not affect the underlying simulation engine.

In general, the egg problem is three-dimensional, but due to rotational symmetry with respect to the egg's axis, it reduces to a two-dimensional problem. For spherical eggs, it reduces to a one-dimensional problem. Thus, a problem's dimensionality is not necessarily the same as the dimensionality of the object in question. Thus, while all objects are three-dimensional, some may be modelled as if they were of lower dimension.

2 METHODS – DEVELOPMENT OF A FIXED GRID SIMULATOR FOR CONDUCTIVE HEAT TRANSFER

One assumes that the initial temperature of the egg is uniform and that the water bath is at a constant temperature.

The two dimensions are *radial* and longitudinal. The latter will be called *axial*.

For numerical simulation, the egg is centred in a slightly larger cylinder subdivided into small cells. We refer to this cylinder as the *frame*.

Each cell is labelled by two integers: The axial coordinate i, and the radial coordinate j. The corresponding coordinates in millimetres are x and y.

In the graphical representation, which shows an egg in longitudinal cross section, the pair of integers (i, j) represents a pixel.

This implies that the centre-to-centre distance of all neighbouring cells is the same along both coordinates. This universal distance is denoted by d and measured in millimetres. A value of about 0.15 mm (the thickness of a sheet of paper) seems intuitively small enough, and also works well.

Axial Decomposition:

The 'slicing' of the cylindrical frame along the axial direction is shown in Fig. 1.

The left-most slice is $i = 0$. The rightmost is $i = N$.
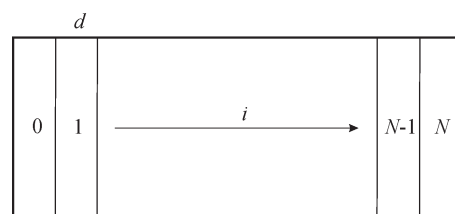
Fig. 1. *Axial decomposition of the cylindrical frame*

Radial Decomposition:

Fig. 2 shows the radial subdivision of the cylinder into rings. The central cells ($j=0$) are solid cylinders of radius d and height d. All other cells are rings of thickness d. The last ring is $j = M$.
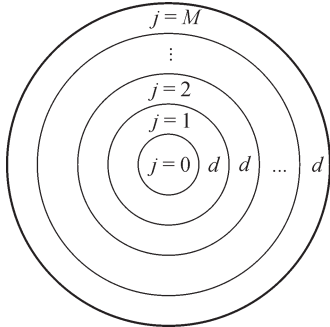
Fig. 2. *Radial decomposition of the cylindrical frame*

The geometric functions:

In Fig. 3, a typical cell ($j>0$) is shown in axial view as a ring of width d (and height d). The parameters specifying the cell are defined in Fig. 3.
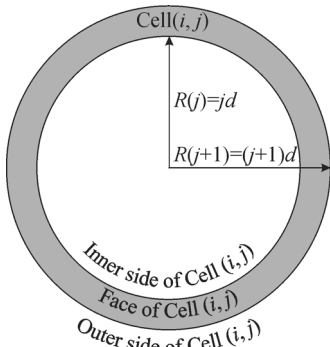
Fig. 3. *A typical cell in the axial view*

The cells are bounded by *sides* and by *faces*.

Radii: $R(j)$ is the radius of the inner bounding side of cell (i,j). Thus, $R(0) = 0$ because the central cells, cell ($i, 0$), are solid cylinders. In general,

$$R(j) = jd. \qquad (1)$$

Sides: $S(j)$ is the area of the inner side of cell (i,j). It is the perimeter $2\pi R(j)$ times the height d. Thus

$$S(j) = 2\pi R(j)d. \qquad (2)$$

Hence, by Eq. (1):
$$\text{inner side: } S(j) = 2\pi d^2 j, \qquad (3)$$

$$\text{outer side: } S(j) = 2\pi d^2 (j+1). \qquad (4)$$

Faces: $F(j)$ is the area of each of the two faces of cell (i,j). It is the difference of two disk areas:

$$F(j) = \pi\left(\left(R(j+1)\right)^2 - \left(R(j)\right)^2\right). \qquad (5)$$

Hence, by Eq. (1),

$$F(j) = \pi d^2 (2j+1). \qquad (6)$$

Volumes: $V(j)$ is the volume of cell (i,j). It is the area of face times the height d:

$$V(j) = F(j)d. \qquad (7)$$

Thus, by Eq. (6),

$$V(j) = \pi d^3 (2j+1). \qquad (8)$$

Distances between cells:

As shown in Fig. 1, the *axial distance* between cell (i,j) and cell ($i+1,j$) is d for all i and all j.

As shown in Fig. 2, the *radial distance* between cell (i,j) and cell ($i+1,j$) is d for all i and all $j > 0$. For $j = 0$, it is $3d/2$. Thus:

$$dist(0,1) = \frac{3}{2}d, \quad dist(1,2) = d \quad \text{etc.}$$

Fourier's law of heat flow and the energy as a function of temperature:

We are to apply the Fourier's law of heat flow:

$$\frac{dQ}{dt} = GA\frac{dT}{dx}, \qquad (9)$$

and the heat energy as a function of temperature:

$$Q = CVT, \qquad (10)$$

to our discrete problem.

Discretization:

The differentials in Eq. (9) are to be replaced by finite differences:

$$\Delta Q = GA\frac{\Delta T}{\Delta x}\Delta t, \qquad (11)$$

which must be sufficiently small for the simulation algorithm to converge.

In Eq. (11), Δx represents the axial as well as radial distance between the centres of neighbouring cells:

$$\Delta x = d. \qquad (12)$$

The elementary time interval is denoted by τ,

$$\Delta t = \tau. \qquad (13)$$

Implementation:

Let temperature and heat contents be stored in arrays $T(N,M)$ and $Q(N,M)$. The fundamental functions $T(x,r)$ and $Q(x,r)$ are thus represented by the array elements $T(i,j)$ and $Q(i,j)$.

In Eq. (10), the volumetric heat capacitance $C(i,j)$, the volume $V(i,j)$, and the temperature $T(i,j)$, all belong to the same cell (i,j).

In Eq. (11), different cells are involved: as shown in Fig. 4, A is the area of the bounding surface, G is the average conductivity of two cells, ΔT is the temperature difference between the cells, and ΔQ is the heat flow through A in the time interval τ. Specifically:

the average axial conductivity G_a of the cell (i,j) is:

$$G_a(i,j) = 2\frac{G(i,j)G(i+1,j)}{G(i,j)+G(i+1,j)}, \qquad (14)$$

and the average radial conductivity G_r of the cell (i,j) is

$$G_r(i,j) = 2\frac{G(i,j)G(i,j+1)}{G(i,j)+G(i,j+1)}. \qquad (15)$$
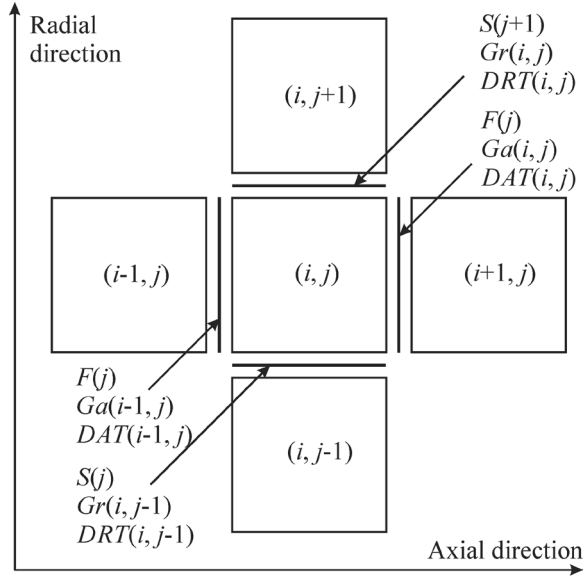
Legende: S - side area, F - face area,
Gr - average radial conductivity,
Ga - average axial conductivity,
DRT - difference radial temperature,
DAT - difference axial temperature.

Fig. 4. *The cell (i,j) and adjacent cells*

To see why, let us think in terms of thermal resistance from centre-to-centre.

The *temperature differences DAT* (difference axial temperature) and *DRT* (difference radial temperature) at any instant in time are defined as:

$$DAT(i,j) = T(i+1,j) - T(i,j), \qquad (16)$$

$$DRT(i,j) = T(i,j+1) - T(i,j). \qquad (17)$$

Fig. 4 and Eq. (9) yield the heat flowing in the time interval τ into the cell (i, j) from its four neighbouring cells:

$$DQ(i,j) = D_1Q(i,j) + D_2Q(i,j) + \\ + D_3Q(i,j) + D_4Q(i,j), \qquad (18)$$

where from top:

$$D_1Q(i,j) = +\frac{\tau}{d}S(j+1)G_r(i,j)DRT(i,j), \qquad (19)$$

from bottom:

$$D_2Q(i,j) = -\frac{\tau}{d}S(j)G_r(i,j-1)DRT(i,j-1), \qquad (20)$$

from right:

$$D_3Q(i,j) = +\frac{\tau}{d}F(j)G_a(i,j)DAT(i,j), \qquad (21)$$

from left:

$$D_4Q(i,j) = -\frac{\tau}{d}F(j)G_a(i-1,j)DAT(i-1,j). \qquad (22)$$

The T-Q relation:

By Eq. (10), the heat difference $DQ(i,j)$ produces a temperature difference $DT(i,j)$ in cell (i,j):

$$T(i,j) = \frac{DQ(i,j)}{V(j)C(i,j)}. \qquad (23)$$

By components, from top:

$$D_1T(i,j) = +\frac{\tau}{d}\frac{S(j+1)G_r(i,j)}{V(j)C(i,j)}DRT(i,j), \qquad (24)$$

from bottom:

$$D_2T(i,j) = -\frac{\tau}{d}\frac{S(j)G_r(i,j-1)}{V(j)C(i,j)}DRT(i,j-1), \qquad (25)$$

from right:

$$D_3T(i,j) = +\frac{\tau}{d}\frac{F(j)G_a(i,j)}{V(j)C(i,j)}DAT(i,j), \qquad (26)$$

from left:

$$D_4 T(i,j) = -\frac{\tau}{d}\frac{F(j)G_a(i-1,j)}{V(j)C(i,j)} DAT(i-1,j), \quad (27)$$

We next introduce the Eqs. (3), (4) (6) and (8) for $S(j)$, $F(j)$ and $V(j)$. After all cancellations, one obtains from top:

$$D_1 T(i,j) = +\tau\frac{2(j+1)G_r(i,j)}{d^2(2j+1)C(i,j)} DRT(i,j), \quad (28)$$

from bottom:

$$D_2 T(i,j) = -\tau\frac{2jG_r(i,j-1)}{d^2(2j+1)C(i,j)} DRT(i,j-1), \quad (29)$$

from right:

$$D_3 T(i,j) = +\tau\frac{G_a(i,j)}{d^2 C(i,j)} DAT(i,j), \quad (30)$$

from left:

$$D_4 T(i,j) = -\tau\frac{G_a(i-1,j)}{d^2 C(i,j)} DAT(i-1,j). \quad (31)$$

Thus, at the cell (i, j), the temporal temperature difference over the time interval τ is given in terms of the spatial temperature differences over the distance d to the four closest neighbours. Introducing the notations:

$$K_1(i,j) = \frac{\tau}{d^2}\frac{2j+2}{2j+1}\frac{G_r(i,j)}{C(i,j)}, \quad (32)$$

$$K_2(i,j) = \frac{\tau}{d^2}\frac{2j}{2j+1}\frac{G_r(i,j-1)}{C(i,j)}, \quad (33)$$

$$K_3(i,j) = \frac{\tau}{d^2}\frac{G_a(i,j)}{C(i,j)}, \quad (34)$$

$$K_4(i,j) = \frac{\tau}{d^2}\frac{G_a(i-1,j)}{C(i,j)}, \quad (35)$$

we have

$$DT(i,j) =$$
$$= K_1(i,j)DRT(i,j) - K_2(i,j)DRT(i,j-1) +$$
$$+ K_3(i,j)DAT(i,j) - K_4(i,j)DAT(i-1,j), \quad (36)$$

$$T(i,j)@(t+\tau) = T(i,j)@t + DT(i,j)@t. \quad (37)$$

Since τ/d^2 in Eqs. (32) to (35) can be treated as a given constant while the matrices $K_1(i, j)$ to $K_4(i, j)$ can be computed only once during simulation setup, the theoretical part of the problem is solved.

3 SIMULATION

3.1 The Simulator Itself

The simulator is coded in the environment of the C++Builder RAD tool. Most of its user interface, which is designed from the Visual Component Library objects, is displayed in [11]. The code itself consists of close to 2000 C lines. The majority of the code is about drawing results and facilitating user input. The actual micro stepping algorithm consists of less than 300 ANSI C lines of code. 5 seconds of real time is simulated in 1 second of simulation time on a platform with the Intel i3 processor.

Thermal data that are used in the simulation are in Table 1. Thermal conductivity and heat capacity data are derived from [12] to [15].

Table 1. *Thermal parameters used in the simulation*

	Thermal conductivity G [W/(mm K)]	Heat capacity C [J/(K mm³)]
Water bath	0.00060	0.00420
Shell	0.00050	0.00200
Egg white	0.00065	0.00120
Yolk	0.00040	0.00300
Air pocket	0.00010	0.00001

3.2 Simulated Cases

Table 2 shows 14 simulation scenarios. Simulation results are in Fig. 5. The purpose of these simulations is to learn the influence of the egg's properties on the heat-up time of the coldest spot within the egg. The initial temperature of the egg is 5 °C. The water bath is at 90 °C. In Fig. 5, a cross-section of the simulated egg is displayed at each of the 14 simulations. The line in the middle of the egg's cross section defines the position of the temperature profile, which is shown below the egg. The temperature profile is drawn each finished 30 seconds interval of the heat-up time. The time needed for the coldest spot within the egg to reach 60 °C, is marked and annotated.

Case 2: 60 °C @ 5 min, 14 s

Case 3: 60 °C @ 6 min, 26 s

Case 1: 60 °C @ 4 min, 12 s = time$_{REF}$

Case 4: 60 °C @ 4 min, 11 s

Case 5: 60 °C @ 4 min, 14 s

Case 6: 60 °C @ 4 min, 14 s

Case 7: 60 °C @ 4 min, 18 s

Case 8: 60 °C @ 3 min, 49 s

Case 9: 60 °C @ 4 min, 30 s

Case 10: 60 °C @ 4 min, 10 s

Case 11: 60 °C @ 4 min, 11 s

Case 12: 60 °C @ 4 min, 2 s @ time$_{REF}$: 62.53 °C

Case 13: 60 °C @ 4 min, 22 s @ time$_{REF}$: 58.70 °C

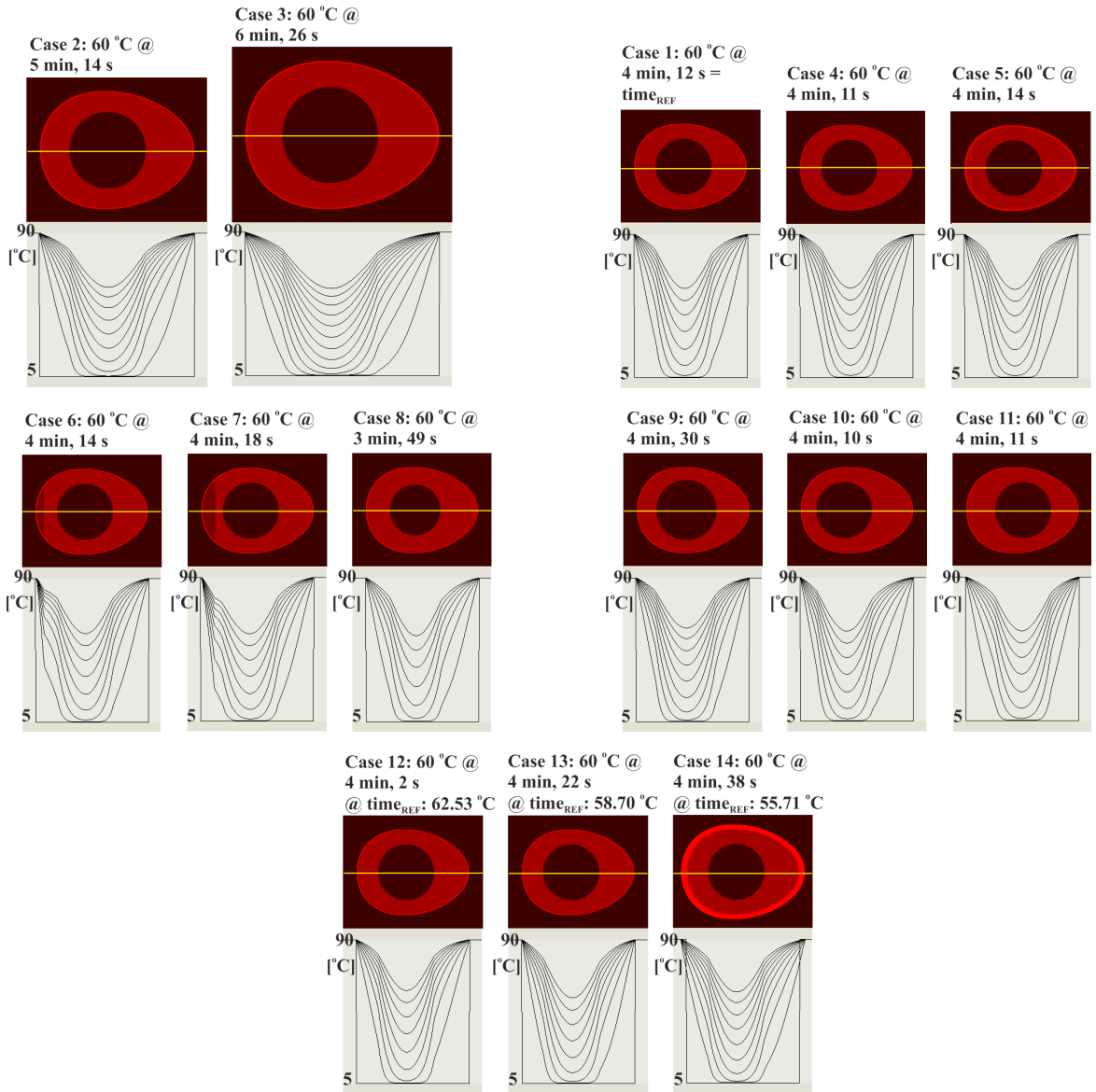**Case 14: 60 °C @ 4 min, 38 s @ time$_{REF}$: 55.71 °C**

Fig. 5. *Simulation results*

Fig. 6. *Mechanical hardware of the laboratory system*

Table 2. *Simulated cases of egg's variability*

Case No.	egg's variant
1	reference sized
2	larger 1
3	larger 2
4	shell thickness 50 %
5	shell thickness 200 %
6	air pocket 5 % egg's volume
7	air pocket 10 % egg's volume
8	yolk volume 90 %
9	yolk volume 110 %
10	yolk to left 10 %
11	yolk to right 10 %
12	white G 110 %, white C 90 %
13	white G 90 %, white C 110 %
14	water cooled by egg's surface

The simulated cases 1 to 3, size of an egg: influence of the egg's size on the heat up time is high. For a spherical object the surface area increases proportionally to the square of the radius and the volume increases proportionally to the cube of the radius. It is similar in the case of an egg. The volume takes up the heat energy, which first has to cross the surface. It is hence not surprising that heat up times of larger eggs are longer.

Cases 4 and 5, shell thickness halved and doubled: influence of shell thickness on the heat up time is not significant (–0.4 %, +0.8 %, compared with the reference time in the Case 1). The shell and other components of the egg have thermal properties of the same magnitude, but the shell is thin, compared to other geometries of the egg. Temperature distributions within an egg in simulated cases 4 and 5 are mostly similar. Halving and doubling the shell thickness has no significant influence either on the heat up time, or on the temperature distribution within an egg.

Cases 6 and 7, formation of an air pocket in an older egg: heat up times are increased by 0.8 % and 2.4 %, which is not significant. The air pocket does influence the temperature distribution within the egg. The air pocket does not influence the location of the coldest spot, which is at the centre of the yolk.

Cases 8 and 9, influence of the yolk's size on the heat up time: a case with a smaller yolk decreases the heat-up time by 9 %, a case with a bigger yolk increases the heat up time by 7 %. Compared to the egg white, the yolk has lower thermal conductivity and higher thermal capacity which is the primary reason for these results.

Cases 10 and 11, influence of yolk's position on the heat-up time: heat up times do not significantly differ at different yolk positions. The temperature distribution is significantly correlated to the position of the yolk, but the coldest spot remains in the centre of the yolk.

Cases 12 and 13, thermal properties of the egg's white: heat up time is within – 4 %, + 10 %. The temperature at the yolk's centre (coldest spot) after the reference heat up time is 1.30 °C and + 2.53 °C off the targeted 60 °C.

Case 14, taking into account water cooling at the egg's surface: the heat-up time is increased by 10 %, which is significant.

4 EXPERIMENTAL WORK

4.1 Design of Control System

The project of making pasteurized soft boiled eggs involves biotechnology, modelling of heat transfer, and design of a mechatronic product within domains of software, electronics and hardware. A unique thermal process had to be developed and implemented.

The corresponding laboratory system was built with the ambition of being as flexible as possible when it comes to experimentation and to be reusable in the design of the apparatus itself. The mechanical hardware of the laboratory system is in Fig. 6.

The hardware consists of two containers filled with water, water cooler, pumps and valves. The system was built with the aim of heating and cooling up to 30 eggs that are immersed in temperature regulated circulating water. The laboratory system has no embedded control system but it is equipped with sensors and actuators. The custom electronics was designed later in the project.

The simultaneous design of the thermal process and of the governing software, without available target embedded electronics could be challenging. We decided to use a PC for the development platform. A data acquisition (DAQ) board was used as an interface between the PC and the sensors and actuators of the experimental system. Temperatures were measured with a temperature meter that is connected to the PC via the serial interface. The project is structured in interrelated software components in Fig. 7. ANSI C was used for the coding, with the aim of portability to the target system, as it became available. MS Windows, which is not a real-time OS, was running on the PC. Since thermal processes are slow (compared to computers) and software process priorities can be set, the Windows OS fits the purpose of this process control. The DAQ board is addressed exclusively via its' ANSI C application programming interface (API).

Interrelated software components of the developed apparatus are in Fig. 8. About 40 % of the process development code was ported to the target system with merely small modifications.
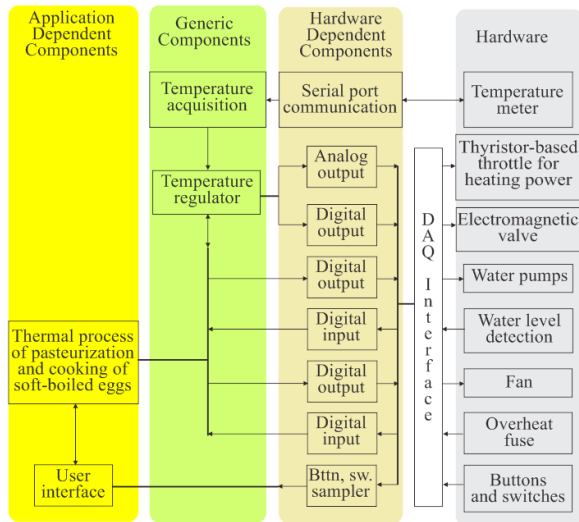

Fig. 7. *Interrelated software components of the laboratory system*
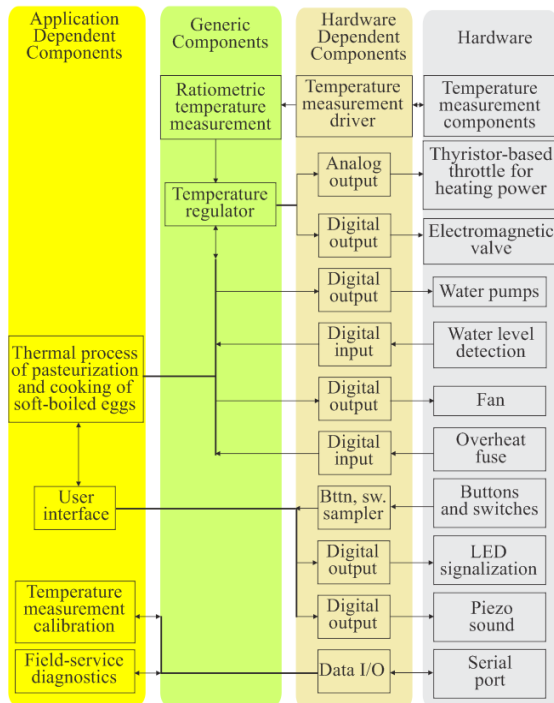
Fig. 8. *Interrelated software components of the apparatus*

4.2 Matching of Simulation and Cooking

The implemented temperature profile for the circulating water in the basin with eggs and measured temperatures in the centres of eggs are in Fig. 9. The designed temperature profile of the circulating water starts at a low enough temperature that the immersed eggs do not break due to thermal stress. The heating power is limited by the regulations imposed on electrical equipment (I_{MAX} = 16 A, single phase, 3700 W with a 230 V grid). Water temperature is limited to 90 °C. After selected times (for different egg sizes) the water temperature drops to 60 °C. At the same time, the coldest spot within an egg reaches 60 °C, which is the pasteurization temperature. 10 minutes later (not shown in Fig. 10) the temperature of the water bath drops to 57 °C, which is low enough for an egg to keep its' organoleptic properties and to stay warm till use.

The developed thermal process needs to be adjusted at the start of each run for the egg size (standard Euro size small (weight ≤ 53 g), medium (53 g < weight ≤ 63 g), large (63 g < weight ≤ 73 g), very large (73 g < weight), - all eggs in the basket are of the same declared size). The developed thermal process is regulated within ± 0.3 °C (temperature of the circulating water bath). This prevents variations in eggs' properties to have noticeable effects on the quality of the pasteurized soft boiled eggs. Fortunately, the thermal process does not have to be adjusted for the other egg parameters then size. Daily use of the apparatus in the field confirms the findings.

Legend:
WT - water temperature, regulated for mid size eggs,
CT_M - center temperature in a mid size egg,
S_CT_M - simulated center temperature in a mid size egg,
CT_S - center temperature in a small egg,
CT_L - center temperature in a large egg.

Fig. 9. *Measured and simulated temperature profiles*

5 DISCUSSION

We learned from the results of the thermal simulations that the heat-up time is significantly related to egg size, yolk size and water being cooled by the egg's surface.

The heat-up time is far less related to the position of yolk, shell thickness, the formation of an air pocket and temperature induced va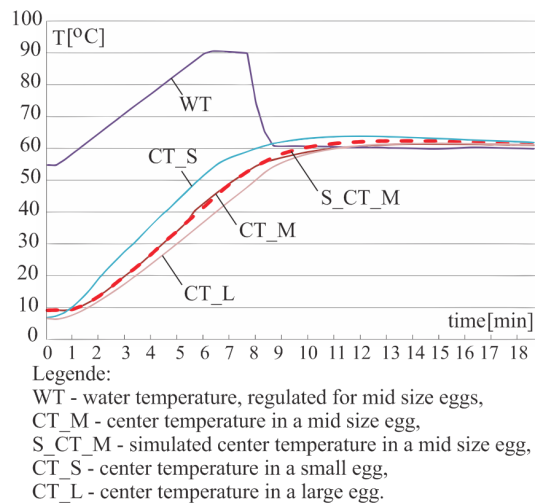riations of the egg white thermal properties. These relationships do not need attention in the production of pasteurized soft boiled eggs.

Heat is transferred by radiation, convection and conduction. Radiative heat transfer is not relevant when heating up an egg in a bucket of hot water. It is a different situation with convective heat transfer. Egg white is a thick liquid - as such it can contribute to heat transfer by convection. Nevertheless, we did not include this type of heat transfer in the simulation. Our reasoning for the exclusion of convective heat transfer from simulation is based on the results of previous experiments related to the thermal treatment of eggs. We had been experimenting with heating-up and cooking eggs of different sizes and ages and origins being stockpiled in a bucket made from a metal mesh. The bucket with the eggs was submersed into a reservoir with circulating hot water with a precisely regulated temperature. We did observe a strong correlation between egg size and invasively measured temperature in the centre of the egg. Measurements did have their own noise since the temperature sensor had to be installed in the centre of the egg. We did not observe significant correlation between the position of an egg in a bucket (laid on a side, on a sharp, on a soft tip) and by organoleptic properties of the produced soft boiled egg. This justifies the exclusion of convective heat transfer in the study.

The relevant similar literature on thermal simulation of eggs is provided in references [12] and [14] to [17].

The results of the CFD thermal simulation of an egg are compared to the thermal measurements in [14]. However, the test eggs are first hollowed out and then refilled with agar that has uniform thermal properties. The simulation correlates well with the measurements.

Ref. [15] presents a CFD thermal simulation of an egg, and studies the influence of the egg's rotation to the rate of the egg heating in water, with the aim of shortening the pasteurization process. Experimental work, i.e., temperature measurements are performed on eggs without yolk.

Ref. [16] is about another CFD thermal simulation and studies heat transfer from the egg's interior to the environment. This study is relevant to the embryotic development within an egg. Experimental work is performed with the help of an instrumented egg with built-in electrical resistors for heat generation.

Ref. [17] presents a CFD thermal simulation, which studies the combined conductive and convective heat transfer in model eggs that are filled with a sodium carboxy-methyl cellulose suspension with well-known uniform thermal properties.

Ref. [12] reports simulation and measurements of pasteurization process for liquid yolk, which is obtained from broken eggs.

Using the aforementioned published research, experimental verification of simulation results is not straightforward. Installing a grid of temperature sensors in an egg, without significantly changing its thermal properties, has not yet been achieved.

On the simulator itself:

Fourier heat equation dates from 1822. For the last thirty years the FEM and to the less extent the Finite Difference Method (FDM) have been utilized for steady state and transient modeling of heat transfer. In the case of both methods one firstly generates a grid with nodes. Secondly, the node temperatures are calculated for each time t of the analysis. The whole simulated structure is analyzed as a unity, which implies that a system of equations is solved for each time t of the transient analysis. To implement algorithms that solve a relatively large system of equations one needs a substantial amount of computer memory and processing power.

In the presented simulation there is no system of n linearly independent equations to calculate n variables at each time t. The objective is to have a faster than real-time transient thermal simulation that runs on a moderate computer platform - a lap top or an embedded system. The final motivation for this objective is the potential integration of a simulation tool for simulation-based predictions into an embedded control system of a modern high-tech mechatronic apparatus. Speed is always needed in interactive simulations.

The performance of embedded systems and personal computers is improving, but there will always be a certain lag between these systems and high end workstations. When it comes to the design of software that is to run on relatively modest platforms for real time applications (embedded systems), a) one needs to be careful about memory use, b) the frequently iterated segments of code need to be optimized for speed, and c) code has to be designed from the beginning with the aim of portability between different platforms – the code is developed on a capable workstation and then it runs in an embedded system. It is a de-facto standard to write code in ANSI C (compilation or cross-compilation for different platforms). Pre-compiled libraries need to be available for all platforms of the project.

We did a test of simulation speed for an area of 50 mm × 20 mm (size of the egg simulation) with the presented simulator (PS) and asked for evaluation of speed and memory using Dassault's ABAQUS for the same case. The ABAQUS speed and the requirement on memory are copied from the received file. Results are presented in Table 3.

Table 3. *PS and ABAQUS, speed and resources*

	Case 1	Case 2	Case 3	Case 4
memory [MB]	10	3	28	80
1 s of simulation time at $\Delta t = 15$ ms	5.00 s of real time	2.10 s of real time	0.05 s of real time	0.003 s of real time

Legende:
Case 1: PS, optimized for speed: cell dimensions: 0.15 mm × 0.15 mm, 44000 cells, CPU Intel i3 2.2 GHz (3 MB cache)
Case 2: PS, optimized for RAM: cell dimensions: 0.15 mm × 0.15 mm, 44 000 cells, CPU Intel i3 2.2 GHz (3 MB cache)
Case 3: ABAQUS, mesh 0.50 mm × 0.50 mm, 4000 nodes, CPU Intel i7 2.2 GHz (8 MB cache)
Case 4: ABAQUS, mesh 0.15 mm × 0.15 mm, 44000 nodes, CPU Intel i7 2.2 GHz (8 MB cache)

Dividing the simulated area into *n* areas, that are simultaneously simulated (depending on capabilities of the platform), divides the simulation time with the same factor *n* (some 10 % added for synchronization of threads). It is realistic to simulate 10 seconds of simulated time in 1 second of real time on a budget platform. With this speed the simulation can become part of a real time control system. What is the technical cost for this fast simulation? Optimal dimensions of cells and length of Δt have to be selected and verified in the simulation of the reference case. Adding the obvious: bigger cells and longer Δt introduce larger errors for mathematical reasons, smaller cells and shorter Δt introduce larger errors for rounding reasons and prolong the simulation time.

Fig. 10. *Golden egg – producer of pasteurized soft boiled eggs*

The derived thermal process is implemented in the apparatus in Fig. 10. The Golden egg produces pasteurized soft boiled eggs in batches of up to 30 eggs in 15 minutes intervals. Based on major industrial food preparation exhibitions, it is currently the only apparatus of its sort. The thermal process is patented.

6 CONCLUSION

A faster than real-time simulator of conductive heat transfer in a cylinder with a fixed simulation grid is developed. The presented simulation framework can be used for simulations of conductive heat transfer in different technical fields. It can be adapted to any problem where the local temporal intensity of changes depends on gradients and the properties of the matter. The case study is a simulation of heating-up an egg in hot water. The results of the study are used in the creation of a thermal process that is implemented in the Golden Egg apparatus which produces certified pasteurized soft boiled eggs.

7 ACKNOWLEDGEMENT

8 REFERENCES

[1] Barbour, E.K., El Jurdia, L., Issab, C., Tannousb, R. (2001). Preliminary attempts towards production of table eggs free from Salmonella enteritidis. *Journal of Cleaner Production*, vol. 9, no. 1, p. 69-73, **DOI:10.1016/S0959-6526(00)00033-0**.

[2] Hou, H., Singh, R.K., Muriana, P.M., Stadelman, W.J. (1996). Pasteurization of intact shell eggs. *Food Microbiology*, vol. 13, no. 2, p. 93-101, **DOI:10.1006/fmic.1996.0012**.

[3] Manas, P., Pagán, R., Alvarez, I., Condón Usón, S. (2003). Survival of Salmonella senftenberg 775W to current liquid whole egg pasteurization treatments. *Food Microbiology*, vol. 20, no. 5, p. 593-600, **DOI:10.1016/S0740-0020(02)00088-6**.

[4] Schuman, J.D., Sheldon, B.W., Vandepopuliere, J.M., Ball, Jr.H.R. (1997). Immersion heat treatments for inactivation of Salmonella enteritidis with intact eggs. *Journal of Applied Microbiology*, vol. 83, no. 4, p. 438–444, **DOI:10.1046/j.1365-2672.1997.00253.x**.

[5] James, C., Lechevalier, V., Ketteringham, L. (2002). Surface pasteurization of shell eggs. *Journal of Food Engineering*, vol. 53, no. 2, p. 193–197, **DOI:10.1016/S0260-8774(01)00156-X**.

[6] Dev, S.R.S., Raghavan, G.S.V., Gariepy, Y. (2008). Dielectric properties of egg components and microwave heating for in-shell pasteurization of eggs. *Journal of Food Engineering*, vol. 86, no. 2, p. 207–214, **DOI:10.1016/j.jfoodeng.2007.09.027**.

[7] Gao, M., Tang, J., Villa-Rojas, R., Wang, Y., Wang, S. (2011). Pasteurization process development for controlling Salmonella

in in-shell almonds using radio frequency energy. *Journal of Food Engineering*, vol. 104, no. 2, p. 299–306, **DOI:10.1016/j.jfoodeng.2010.12.021**.

[8] Monfort, S., Saldana, G., Condon, S., Raso, J. (2012). Inactivation of Salmonella spp. in liquid whole egg using pulsed electric fields, heat, and additives. *Food Microbiology*, vol. 30, no. 2, p. 393–399, **DOI:10.1016/j.fm.2012.01.004**.

[9] Verde, S.C., Tenreiro, R., Botelho, M.L. (2004). Sanitation of chicken eggs by ionizing radiation: HACCP and inactivation studies. *Radiation Physics and Chemistry,* vol. 71, no 1-2, p. 27–31, **DOI:10.1016/j.radphyschem.2004.03.064**.

[10] Silva, F.V.M., Gibbs, P.A. (2012). Thermal pasteurization requirements for the inactivation of Salmonella in foods. *Food Research International*, vol. 45, no. 2, p. 695–699, **DOI:10.1016/j.foodres.2011.06.018**.

[11] Jenko, M. (2014). GUI of the Thermal Simulator, *from http://www2.arnes.si/~mjenko9/SimT/GUI.jpg* , accessed on 2014-11-28.

[12] Gut, J.A.W., Pinto, J.M., Gabas, A.L., Telis-Romero, J. (2005). Continuous pasteurization of egg yolk: thermo physical properties and process simulation. *Journal of Food Process Engineering*, vol. 28, no. 2, p. 181-203, **DOI:10.1111/j.1745-4530.2005.00416.x**.

[13] Romanoff, A.L., Romanoff, A.J. (1949). *The Avian Egg.* John Wiley and Sons, Hoboken, p. 150-169.

[14] Denys, S., Pieters, J.G., Dewettinck, K. (2003). Combined CFD and experimental approach for determination of the surface heat transfer coefficient during thermal processing of eggs. *Journal of Food Science*, vol. 68, no. 3. p. 943-951, **DOI:10.1111/j.1365-2621.2003.tb08269.x**.

[15] Ramachandran, R., Malhotra, D., Anishaparvin, D, Anandharamakrishnan, C. (2011). Computational fluid dynamics simulation studies on pasteurization of egg in stationary and rotation modes. *Innovative Food Science and Emerging Technologies*, vol. 12, no. 1, p. 38-44, **DOI:10.1016/j.ifset.2010.11.008**.

[16] Ozcan, S.E., Andriessens, S., Berckmans, D. (2010). Computational study of the heat transfer of an avian egg in a tray. *Poultry Science*, vol. 89, no. 4, p. 776–784, **DOI:10.3382/ps.2009-00230**.

[17] Denys, S., Pieters, J.G., Dewettinck, K. (2004). Computational fluid dynamics analysis of combined conductive and convective heat transfer in model eggs. *Journal of Food Engineering*, vol. 63, no. 3, p. 281–290, **DOI:10.1016/j.jfoodeng.2003.06.002**.

Six-Axis Linkage Strategy and Its Models
for Non-Circular Helical Gears Based on Diagonal Hobbing

Youyu Liu[1,2,*] – Jiesheng Diao[1,2]

[1] School of Mechanical and Automotive Engineering, Anhui Polytechnic University, China
[2] AHPU Institute of Technology Robotics Industry, Anhui Polytechnic University, China

Among cutter teeth of the hob when hobbing non-circular helical gears, there are some issues such as uneven load and wear. To solve those problems, a simultaneous six-axis hobbing model had been developed based on diagonal hobbing. Four probable working conditions were provided. Linkage models corresponding to the four conditions were verified by virtual hobbing, in which the profile accuracies were compared and analyzed. The four working conditions were analyzed including linear (or angular) velocities and linear (or angular) accelerations. Consequently, two implementation strategies including repeating axial shift and reciprocating axial shift were offered. The linkage models and their strategies have been verified by hobbing testing. Experimental results show that diagonal hobbing is superior to non-diagonal hobbing in that the hob life of the former is 3.68 longer than that of the latter, and the micro-topography in the teeth surface of the former is more stable during transmission.

Keywords: non-circular helical gears, diagonal hobbing, linkage models, hob life

Highlights
- *A simultaneous six-axis hobbing model has been developed based on diagonal hobbing.*
- *Four linkage models corresponding to four working conditions have been verified respectively by virtual hobbing.*
- *The tool paths display that the tooth accuracies under four working conditions are uniform.*
- *Two implementation strategies including repeating axial shift and reciprocating axial shift have been offered.*
- *The hob life of diagonal hobbing is 3.68 larger than that of non-diagonal hobbing.*
- *The micro-topography in the teeth surface using diagonal hobbing contributes to stable drive.*

0 INTRODUCTION

As a result of the comprehensive combination of circular gears and cams, non-circular gears can deliver high output power accurately with continuously variable transmission and have been widely used in vehicles [1], agricultural machinery [2], fluid machinery [3], light industrial machinery [4], and so on. Numerous in-depth studies on the design and applications of non-circular gears have been carried out with great academic achievements in recent ten years [5] to [7]. However, the practical applications of non-circular gears are not commensurate with their numerous advantages with manufacturing technology lagging behind the research. Shaping and hobbing are two kinds of efficient cutting methods available for gears. We have realized the machining of non-circular helical gears using gear shaping [8] and [9]. Tan et al. [10] have developed a basic mathematical model only for hobbing non-circular spur gears. Tian et al. [11] have built some basic mathematical models for hobbing non-circular helical gears, with helical teeth, by a generating method of helical tooling rack based on non-diagonal hobbing, but provided no processing program for them. We have constructed some hobbing schemes and linkage models based on a four-axis

linkage [12] and a five-axis linkage [13], and have singled out two excellent strategies with their linkage models. All in all, those works make hobbing non-circular (spur or helical) gears possible and greatly improve the production efficiency in contrast to the classic wire electric discharge machining [14] that is used to machine non-circular spur gears. All the hobbing models above keep hobs fixed in their axial positions. Thus, only parts of the cutter teeth on the hob take part in hobbing. Moreover, it is a small fixed section of the cutting edge for each cutter tooth that actually takes part in hobbing. These cutting edges will be abraded continuously during the hobbing process, which will affect the shape accuracy of the tooth profile and its roughness. Load and wear among the cutter teeth of the hob are seriously uneven in hobbing using non-diagonal hobbing. The hob life depends on the cutter tooth that has the largest amount of wear. Thus, hob life in non-diagonal hobbing is extremely low.

In order to solve this problem, and to make the most use of all cutter teeth and make load and wear among them equal, a six-axis linkage strategy and its models for hobbing non-circular helical gears are developed according to a principle of diagonal hobbing in this paper. In this linkage strategy, the hob

moves along its axis continuously while it is moving in a vertical direction. The linkage strategy and its linkage model have been verified to be correct and feasible by virtual hobbing, dynamics analysis, and hobbing testing. Finally, some practical applications are offered.

1 LINKAGE STRATEGY BASED ON DIAGONAL HOBBING

A simultaneous five-axis hobbing scheme [13] for non-circular helical gears is shown in Fig. 1. The projection of the hob in the cross-section of the gear billet is a rack. Thus, the hob spinning as ω_b can form a tooling rack. ω_c of the gear billet generates a meshing movement with ω_b, and both of them keep a strict transmission ratio. As shown in Fig. 2, the rotation of the pitch curve of the gear billet is a pure rolling along the midline of the tooling rack without slipping. The midline of the tooling rack is tangent to point P with the pitch curve of gear billet. To create a pure rolling, the gear billet should move along both x-axis (namely $\mathbf{v}_x$) and y-axis (namely $\mathbf{v}_y$) while it is spinning as ω_c. In order to cut a full-depth tooth, the hob should move along the z-axis (namely $\mathbf{v}_z$). $\mathbf{v}_z$ has a strict linkage with $\Delta\omega_c$, which can form a helical tooling rack to cut non-circular helical gears. In this scheme, the hob is fixed along its axle and the meshing point of the pitch curve is located on the fixed point P in space, and then only part of the cutter teeth around point P actually take part in the hobbing, which will radically reduce hob life and teeth accuracy.
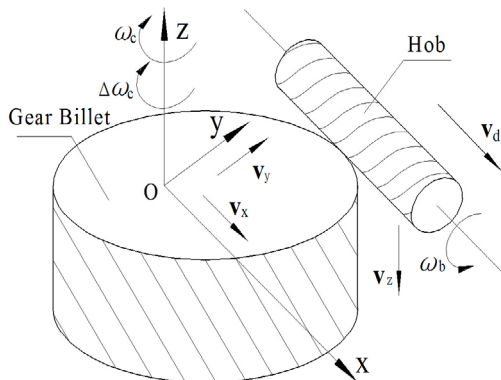

Fig. 1. *Schematic diagram of hobbing process*

Diagonal hobbing implies that hob continuously moves along its own axis so that all of cutter teeth take part in hobbing without damaging the original simultaneous five-axis motion. As shown in Fig. 2, a diagonal feedrate ($\mathbf{v}_d$) along the hob axis is added to the linkage system. The direction of $\mathbf{v}_d$ along the hob axis conforms to the rule of right-hand corkscrew with

ω_b (marked as 'U'), and can also conform to a rule of a left-hand corkscrew (marked as 'V') [15]. From Fig. 2, we can see:

$$\mathbf{v}_b^* = \mathbf{v}_b + \mathbf{v}_{dx}. \tag{1}$$
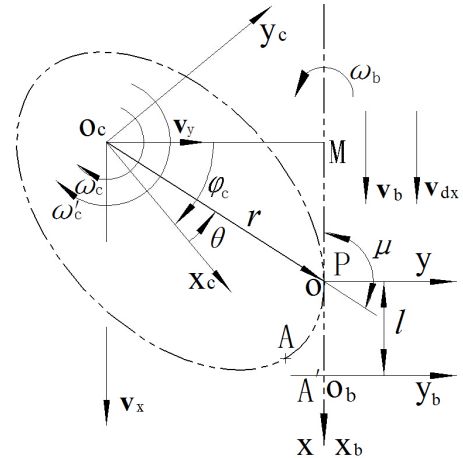
Fig. 2. *Cross-section of gear billet*

The original vertical movement $\mathbf{v}_z$ of the hob creates a resultant velocity $\mathbf{v}_z^*$ with $\mathbf{v}_{dz}$. That is to say,

$$\mathbf{v}_z^* = \mathbf{v}_z + \mathbf{v}_{dz}. \tag{2}$$

Just like circular helical gears, non-circular helical gears can be divided into two types: left-hand gears (marked as 'L') and right-hand ones (marked 'R'). As shown in Fig. 3:

$$v_{dz} = v_d \sin(\lambda_b \pm \beta_c), \tag{3}$$

where the '−' is adopted for left-hand helical gears, the '+' for right-hand ones.

Fig. 3. *Common tangent plane of hobbing*

A reasonable $\mathbf{v}_z^*$ can be chosen according to the requirements of axial tooth accuracy, and then a proper $\mathbf{v}_z$ can be determined by the value of $\mathbf{v}_{dz}$. For a non-circular helical gear, the gear billet should rotate an additional cycle when $\mathbf{v}_z^*$ moves a screw lead along the axle of the gear billet [16], from which the value of $\Delta\omega_c$ is determined.
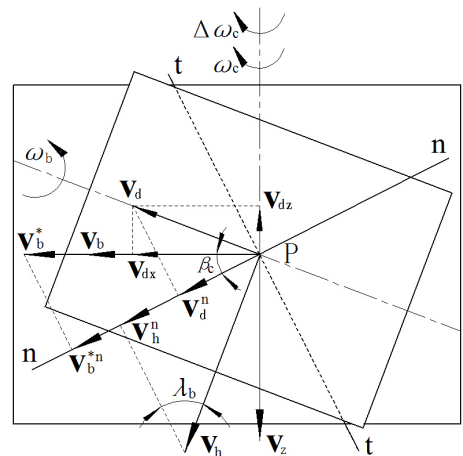
Thus, this diagonal hobbing is a simultaneous six-axis linkage method, which includes two implementing schemes: 'U' and 'V'.

2 LINKAGE MODELS BASED ON DIAGONAL HOBBING

As shown in Fig. 2, $S(o-xyz)$ is located at point P, where the x-axis and the z-axis are parallel to the pitch line of the hob and the shaft of the gear billet respectively. $S_c(o_c-x_cy_cz_c)$ revolves with the gear billet, in which the origin lies in the rotation center of the gear billet and each axis is parallel with that of $S(o-xyz)$ at the beginning. $S_b(o_b-x_by_bz_b)$ moves with the the tooling rack of the hob, which coincides with $S(o-xyz)$ at the beginning. The polar equation of the pitch curve is $r=r(\theta)$. At the beginning, the polar axis and the y-axis are kept in superposition. The forward direction of φ_c, θ, and ω_c are shown in Fig. 2. μ can be calculated according to Eq. (4) [16].

$$\tan\mu = r/(dr/d\theta) \qquad (0 \leq \mu < \pi),\qquad(4)$$

hence,

$$\begin{cases} \sin\mu = r \Big/ \sqrt{r^2 + (dr/d\theta)^2} \\ \cos\mu = (dr/d\theta) \Big/ \sqrt{r^2 + (dr/d\theta)^2} \end{cases},\qquad(5)$$

from Fig. 2,

$$\theta = \varphi_c - \mu + \pi/2.\qquad(6)$$

From Eq. (4),

$$\frac{d\mu}{dt} = \frac{(dr/d\theta)^2 - r(d^2r/d\theta^2)}{r^2 + (dr/d\theta)^2} \cdot \frac{d\theta}{dt}.\qquad(7)$$

Consequently, ω is as follows:

$$\omega = \frac{d\theta}{dt} = \frac{r^2 + (dr/d\theta)^2}{r^2 + 2(dr/d\theta)^2 - r(d^2r/d\theta^2)}\omega_c.\qquad(8)$$

As shown in Fig. 2, since the midline of the tooling rack makes a pure rolling at point P with the pitch curve of gear billet, l should be equal to s, as follows.

$$l = s = \int_0^\theta \sqrt{r^2 + (dr/d\theta)^2}\, d\theta.\qquad(9)$$

Then, $\mathbf{v}_b^*$ is as follows:

$$v_b^* = v_b + v_{dx} = \frac{dl}{dt} = \sqrt{r^2 + (dr/d\theta)^2} \cdot \frac{d\theta}{dt}.\qquad(10)$$

Eq. (8) is substituted in Eq. (10):

$$v_b^* = \frac{\Big[r^2 + (dr/d\theta)^2\Big]^{3/2}}{r^2 + 2(dr/d\theta)^2 - r(d^2r/d\theta^2)}\omega_c,\qquad(11)$$

v_x and v_y are as follows:

$$\begin{cases} v_x = \dfrac{d(r\cos\mu)}{dt} = -r\sin\mu\dfrac{d\mu}{dt} + \cos\mu\dfrac{dr}{d\theta}\dfrac{d\theta}{dt} \\ v_y = \dfrac{d(r\sin\mu)}{dt} = \sin\mu\dfrac{dr}{d\theta}\dfrac{d\theta}{dt} + r\cos\mu\dfrac{d\mu}{dt} \end{cases}.\qquad(12)$$

Eqs. (5), (7) and (8) are substituted in Eq. (12),

$$\begin{cases} v_x = \dfrac{r^3(d^2r/d\theta^2) + (dr/d\theta)^4}{\sqrt{r^2 + (dr/d\theta)^2}\Big[r^2 + 2(dr/d\theta)^2 - r(d^2r/d\theta^2)\Big]}\omega_c \\ v_y = \dfrac{r(dr/d\theta)}{\sqrt{r^2 + (dr/d\theta)^2}}\omega_c \end{cases}.\qquad(13)$$

Due to the pure rolling, the tangent velocity of the gear billet at point P should be equal to the translational speed $\mathbf{v}_b^*$ of the tooling rack. As shown in Fig. 3, the normal components of the velocities $\mathbf{v}_d$, $\mathbf{v}_b^*$, and $\mathbf{v}_h$ are $\mathbf{v}_d^n$, $\mathbf{v}_b^{*n}$, and $\mathbf{v}_h^n$ are on the meshing point P. The normal velocity of the gear billet at point P should be equal to that of the hob [11]. Thus,

$$v_h^n + v_d^n = v_b^{*n}.\qquad(14)$$

The value of $\mathbf{v}_h$ is as follows:

$$v_h = Km_t\omega_b/2 = Km_n\omega_b/(2\sin\lambda_b).\qquad(15)$$

From Fig. 3, and Eqs. (11), (14) and (15):

$$\frac{Km_n\omega_b}{2} + \kappa v_d\cos\lambda_b = \frac{\Big[r^2 + (dr/d\theta)^2\Big]^{3/2}\cos\beta_c}{r^2 + 2(dr/d\theta)^2 - r(d^2r/d\theta^2)}\omega_c.\qquad(16)$$

For scheme 'U', $\kappa=1$ in Eq. (16); for scheme 'V', $\kappa=-1$.

As mentioned, the gear billet should rotate for an additional cycle when $\mathbf{v}_z^*$ moves a screw lead along the axle of the gear billet. Therefore,

$$\int_0^t r\Delta\omega_c\, dt = \int_0^t \tan\beta_c v_z^*\, dt \quad . \text{ Thus,}$$

$$\Delta\omega_c = \left(v_z^* \tan\beta_c\right)/r. \tag{17}$$

Consequently, ω_c^* can be deduced from Eqs. (2) and (17).

$$\omega_c^* = \omega_c \pm \left(\left(v_z - \kappa v_{dz}\right)\tan\beta_c\right)/r, \tag{18}$$

where the '+' is adopted as the helix direction of the hob, which is in accordance with that of the gear; otherwise, the '−' is adopted.

According to Eqs. (13), (16) and (18), a six-axis linkage model based on diagonal hobbing is built by use of a method of equal arc-length for the gear billet such that the velocity of the hob remains constant [12]. ω_b, v_d and v_z are three independent fundamental frequencies, and the other axes move with them in a strict transmission ratio. The linkage model is as follows.

$$\begin{cases} v_x = \dfrac{r^3\left(d^2r/d\theta^2\right)+\left(dr/d\theta\right)^4}{\left[r^2+\left(dr/d\theta\right)^2\right]^2\cos\beta_c}\xi \\[2ex] v_y = r\dfrac{dr}{d\theta}\dfrac{r^2+2\left(dr/d\theta\right)^2-r\left(d^2r/d\theta^2\right)}{\left[r^2+\left(dr/d\theta\right)^2\right]^2\cos\beta_c}\xi \\[2ex] \omega_c^* = \dfrac{r^2+2\left(dr/d\theta\right)^2-r\left(d^2r/d\theta^2\right)}{\left[r^2+\left(dr/d\theta\right)^2\right]^{3/2}\cos\beta_c}\xi \pm \\[2ex] \qquad \pm \dfrac{\left(v_z-\kappa v_{dz}\right)\tan\beta_c}{r} \end{cases}, \tag{19}$$

where $\xi = Km_n\omega_b/2 + \kappa v_d\cos\lambda_b$.

3 VERIFYING BY VIRTUAL HOBBING

According to linkage model (Eq. (19)), there are two implementing methods corresponding to the schemes 'U'($\kappa=1$) and 'V' ($\kappa=-1$). Both of the two types of gears ('L' or 'R') can be hobbed by use of the two implementing methods, thus the possible arrangements are as follows: UL, UR, VL, VR. We want to verify these four working conditions by virtual hobbing using MATLAB before their use in practical applications.

A 3rd order elliptic helical gear is a kind of typical non-circular helical gear for which the polar radius r of the pitch curve changes with differing polar angles θ, and has the essential characteristics of any non-circular helical gear. Consequently, a 3rd order elliptic helical gear is analyzed as an example in this article and the conclusions drawn can be expanded to other non-circular helical gears with free pitch curve. The equation of the pitch curve of a 3rd order elliptic helical

gears is shown in Eq. (20) [16]. Its key parameters are as follows: $A=140$ mm; $e=0.1$; $m_n=8$ mm; $\beta_c=10°34'$; $Z=35$; b$=50$ mm; $K=1$; $\lambda_b=3°19'$.

$$r = A\left(1-e^2\right)/\left(1-e\cos3\theta\right). \tag{20}$$

The motion of each axis is determined according to Eq. (19). Each working condition will take 15 seconds to hob one cycle along the pitch curve of the gear and 300 seconds for the whole process. The processing parameters are shown in Table 1. A tool rack is shown in Fig. 4e), which can keep in pure rolling along the pitch curve of the non-circular gears in linkage models and then the tooth profile of gears can be enveloped. The tool paths are shown in Figs. 4a to d, which show that a non-circular helical gear can be hobbed correctly based on a diagonal process under each working condition.

**Table 1.** *Processing parameters of the four working conditions*

Working conditions	ω_b [rad/s]	v_z [mm/s]	κv_d [mm/s]
UL	14.661	−0.230	5.000
UR	14.661	−0.047	5.000
VL	14.661	−0.104	−5.000
VR	14.661	−0.287	−5.000

As shown in Fig. 2, according to pure rolling, the linear velocity of the pitch curve at point P is constant when both ω_b and v_d (v_{dx}) are constant, which can still meet the requirement of equal arc-length for the gear billet. Therefore, the tool paths of all four working conditions shown in Fig. 4 are evenly distributed along their pitch curves, and the profile accuracy of each tooth is uniform under every working condition. v_z is controlled by an independent fundamental frequency and makes a linkage with other axes, which is assigned according to Table 1 for every working condition. Thus, $\mathbf{v}_z^*$ determined by Eq. (2) is always −0.167 mm for every working condition. Therefore, the axial accuracy of all teeth is also uniform under every working condition.

In short, a non-circular helical gear whether 'L' or 'R' can be hobbed by use of the scheme 'U' or 'V'. Moreover, their tool paths show that the tooth accuracies under the four working conditions are uniform.

4 DYNAMICS ANALYSIS FOR THE FOUR WORKING CONDITIONS

For the four working conditions, the characteristics of linear (or angular) velocities (or accelerations) of each axis are analyzed respectively to compare their
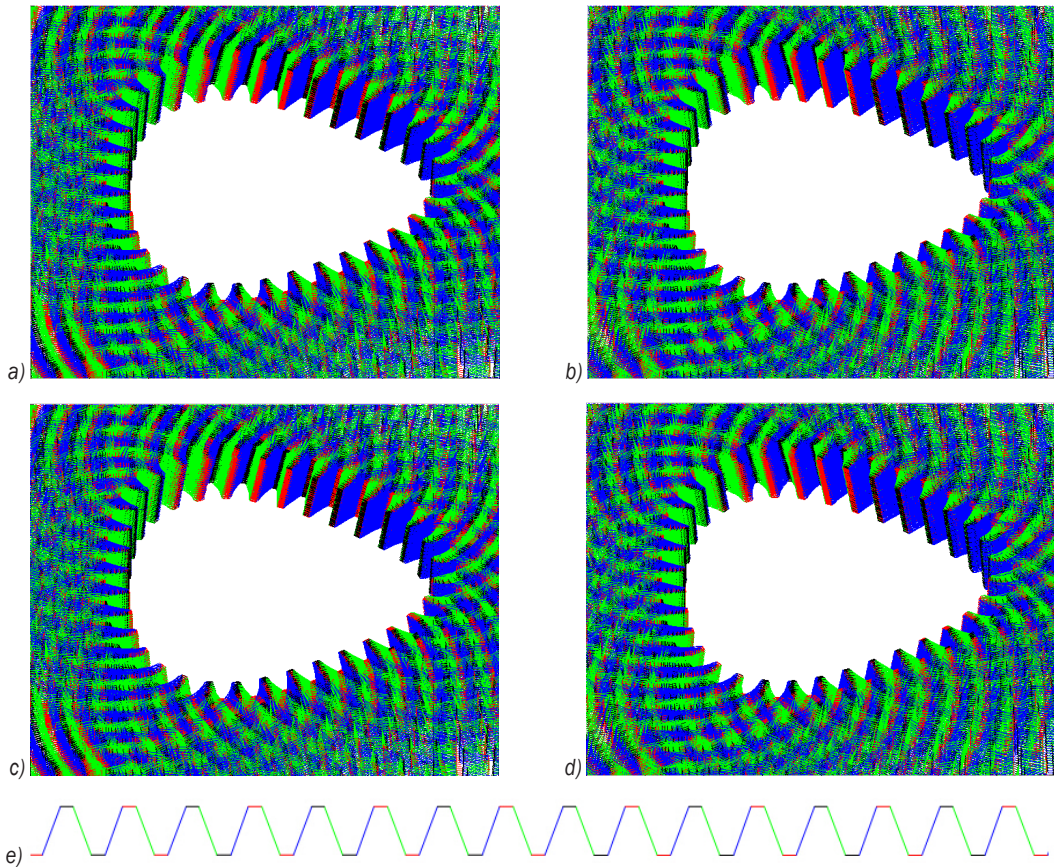
Fig. 4. *Virtual hobbing non-circular helical gears based on a diagonal process; a) working condition 'UL', b) working condition 'UR', c) working condition 'VL', d) working condition 'VR', e) tool rack*

dynamic performances. We work with the 3rd order elliptic helical gear mentioned above by taking the values in Table 1 for ω_b, v_z and v_d.

4.1 Performance Analysis for Linear (or Angular) Velocities

As shown in Fig. 5, curves ω_c^*, v_x and v_y under the four working conditions are drawn respectively using MATLAB as the polar angle of the pitch curve changes from 0 to 2π. As for ω_c^*, shown in Fig. 5a, the largest difference between the working condition 'UL' and that of 'UR' is only about 0.3%, while that between working condition 'VL' and 'VR' is about 0.4%. An implication can be drawn that tendency to variation of curves ω_c^* in 'UL' and 'UR' are approximate, the same as in 'VL' and 'VR'. However, the range of ω_c^* in scheme 'U' ('UL' and 'UR') is significantly larger than that in scheme 'V' ('VL' and 'VR'). The former is about 1.2 times as much as the latter. As shown in Fig. 5b, it was found that curve v_x in 'UL' accords well with that in 'UR', and curve v_x in 'VL' tallies totally with that in 'VR'. As shown in Fig.

5c, curve v_y in 'UL' accords similarly well with that in 'UR', and curve v_y in 'VL' tallies totally with that in 'VR'. This is because the helix direction of a gear has nothing to do with its pitch curve, and thus the different rotating direction of the teeth has no effect on v_x or v_y. As for v_x, the largest difference between scheme 'U' and scheme 'V' in Fig. 5b is approximately 16.0%; as for v_y, the largest difference between scheme 'U' and scheme 'V' in Fig. 5c is about 17.0%. It is thus clear that different scheme ('U' or 'V') have different effects on v_x, as well as v_y.

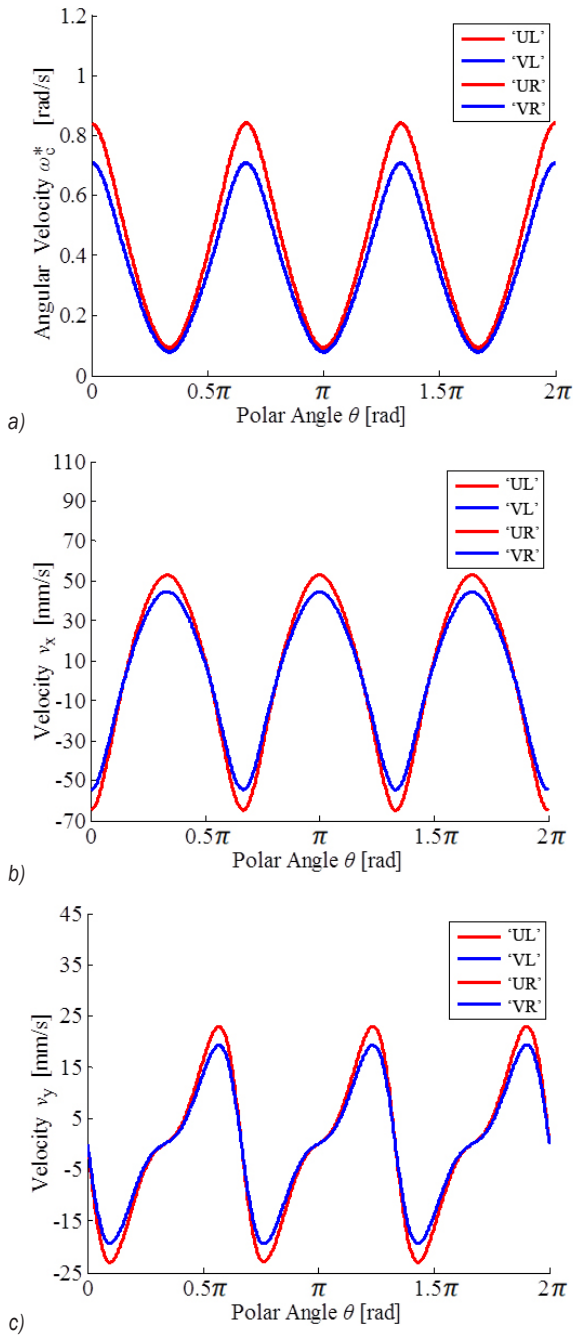### 4.2 Performance Analysis for Linear (or Angular) Accelerations

From Eqs. (9) and (16),

$$\int_0^\theta \sqrt{r^2 + (dr/d\theta)^2}\, d\theta = \frac{Km_n\omega_b + 2\kappa v_d \cos\lambda_b}{2\cos\beta_c} t. \quad (21)$$
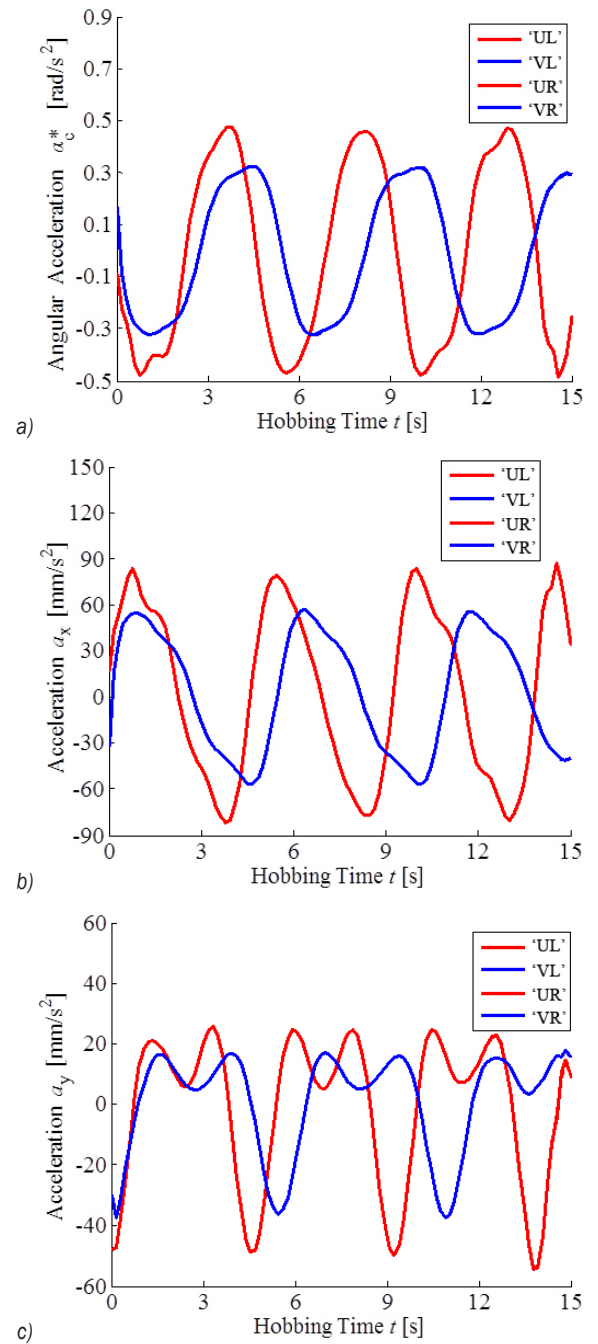
Horizontal axis θ in Fig. 5 can be transformed into corresponding hobbing time t according to Eq. (21). Thus, all of curves $v(\omega)-\theta$ in Fig. 5

Fig. 5. Curves of $v(\omega)-\theta$; a) curve of $\omega_c^* - \theta$, b) curve of $v_x - \theta$, c) curve of $v_y - \theta$

Fig. 6. Curve of $a(\alpha)-t$; a) curve of $\alpha_c^* - t$, b) curve of $a_x - t$, c) curve of $a_y - t$

can be converted into curves $v(\omega)-t$. The curves characterized by some discrete points are fitted into some n-order polynomials by means of a function $p=\text{polyfit}(t,v(\omega),n)$ in MATLAB [17]. The polynomials thus derived are differentiated by use of $pp=\text{polyder}(p)$, of which the differential values $a(\alpha)$ at sequence time t can be calculated using a function

$a(\alpha)=\text{polyval}(pp,t)$. Curves $a(\alpha)-t$ are derived and shown in Fig. 6.

As for α_c^* shown in Fig. 6a, the largest difference between the working condition 'UL' and that of 'UR' is less than 0.1%. Similarly, curve α_c^* in working condition 'VL' is almost the same as that in working

condition 'VR'. Nevertheless, the range of α_c^* in scheme "U" ("UL" and "UR") is about 1.4 times as much as that in scheme 'V' ('VL' and 'VR'). As shown in Fig. 6b, curve a_x in 'UL' accords well with that in 'UR', and curve a_x in 'VL' tallies totally with that in 'VR'. As shown in Fig. 6c, similarly, curve a_y in 'UL' accords well with that in 'UR', and curve a_y in 'VL' tallies totally with that in 'VR'. As shown in Fig. 6b, however, the value of a_x in scheme 'U' is about 1.36 times as much as that in scheme 'V'. As shown in Fig. 6c, the value of a_y in scheme 'U' is about 1.38 times as much as that in scheme 'V'.

In brief, as for ω_c^*, v_x, v_y and α_c^*, a_x, a_y in scheme 'V', their variation ranges are relatively narrow, which is in favor of speed control for high speed hobbing and can thus ensure that the system has a better dynamic quality. The speed value of every axle in scheme 'U' is no more than 120% of the corresponding one in scheme 'V'. The acceleration value of every axle in scheme 'U' is no more than 140% of the corresponding one in scheme 'V'. Since it may not result in a drop in control performance, scheme 'U' can also be adopted for medium-low speed. As for high speed, however, scheme 'U' is not suitable because excessive hobbing speeds or accelerations will reduce the control accuracy and dynamic quality of system. Moreover, a conclusion can be drawn that the speeds and accelerations of every axle in scheme 'U' or scheme 'V' will have no effect on the different rotating direction of the teeth.

5 IMPLEMENTATION STRATEGIES FOR LINKAGE MODELS

Being subject to the influences of cutter material, main shaft bearing, machine stiffness and so on, a gear hobbing machine should give priority to scheme 'V' ('VL' or 'VR'), although all four working conditions mentioned can be adopted when hobbing speed is not high. The length of a hob axis should not be too long given the stiffness of the process system, which means that the length of many hob axes cannot meet the hobbing demand of gears with too long pitch curves or too wide teeth. That is because hobs move along only one direction in their axes under the four working conditions.

For higher speeds, a method called repeating axial shift can be applied to solve the above problem. Only scheme 'V' is used in this method. The hob cuts along (or perpendicular to) its shaft at the beginning. As the meshing point P moves to the end of the hob axis, the hob will cut off along (or perpendicular to) its shaft and go back to the beginning with no cutting

stroke and then cut in again. Thus, the meshing point P goes back to the beginning of hob axis, and so forth. In this method, a long idle travel time is indispensable. Moreover, because of the secondary feed, there are lots of connective cutting marks on the tooth flanks.

As for medium-low speed, a method called reciprocating axial shift can be applied to solve the above problem. Scheme 'V' is adopted firstly. When the meshing point P moves to the end of the hob axis, scheme 'U' is subsequently applied, in which point P moves in reverse from the end to the beginning. When point P reaches the beginning, scheme 'V' is adopted again, and so forth. Because this gets rid of the deficiencies of repeating axial shift, this method should be given priority in applications.

6 ANALYSIS FOR HOBBING EXPERIMENTS

According to the linkage model in Eq. (19), a manufacturing module (including repeating axial shift and reciprocating axial shift) for non-circular helical gears has been developed based on a hobbing platform using ARM & DSP & FPGA [18], which has been used in a gear hobbing machine (STAR-2014 G). The 3rd order elliptic helical gear mentioned using the method of reciprocating axial shift ('VL' & 'UL') and the processing parameters shown in Table 1 is shown in Fig. 7. Four standard hobs [19] connected in series are installed on the hob axis, the parameters of which are as follows: $m_n = 8$ mm, $L_b = 132$ mm, $Z_b = 10$. This shows that non-circular helical gears can be hobbed correctly.

Fig. 7. *3rd order elliptic helical gear, hobbed*

To compare and analyze the properties of diagonal hobbing for non-circular helical gears, we conducted another experiment based on the method of non-diagonal hobbing at the same time. The non-diagonal hobbing experiment can be transformed from the diagonal one with the same efficiency by setting $v_d = 0$ and $v_z = -0.167$ mm/s.

6.1 Hob Life

In the two experiments, the material used for the gear billets is 45 carbon steel and that of the hobs high-speed steel coated TiN. The wear standard of a hob is a permissible value VB_{per} of flank wear at a normal wear stage [20]. The prescribed limits of VB_{per} is 0.2 mm. 3rd order elliptic helical gears are hobbed using diagonal hobbing and non-diagonal hobbing separately in the range of wear standard. The measured values of wear width VB on the flanks of the hobs are shown in Fig. 8 in the two experiments. On the one hand, the wear mass loss on the flank of hob reach VB_{per} after hobbing 12 gears in non-diagonal hobbing. Therefore, L_m is 21358 mm according to Eq. (22) [20]. On the other hand, L_m is 311466 mm in diagonal hobbing up to the VB_{per} after hobbing 175 gears.

$$l_m = \frac{Zbn}{\cos(\beta_c)}. \tag{22}$$

It was found that wear parts are mostly focused on the 8th to the 21st cutter teeth in non-diagonal hobbing. Moreover, wear appears particularly severe around the 16th one. However, the 1st to the 7th cutter teeth and the 22nd to the 35th ones do not participate in hobbing and their wear is nearly zero. On the other hand, there is certain wear from the 2nd cutter tooth to the 34th one in diagonal hobbing. Particularly, the wear width VB of the 6th to the 31st cutter teeth generally remains at around 0.193 mm. A formula for hob life T is shown in Eq. (23) [20], from which we can see that the hob life in diagonal hobbing is about 14.58 times longer than that in non-diagonal hobbing. In view of this, there is actually only one standard hob involved in cutting for non-diagonal hobbing and the other three hobs can be used latter, the actual ratio is about 3.68.
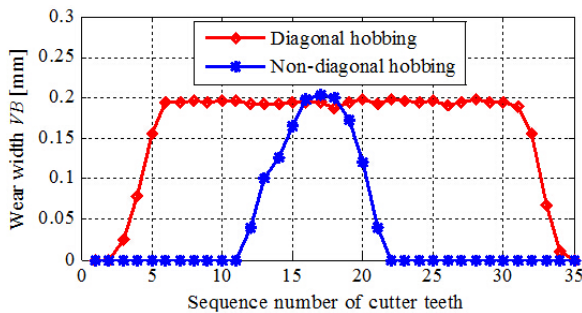

Fig. 8. *Wear width of flank surface for two kinds of hobbing*

$$T = \frac{VB_{per}}{v_h} \cdot \frac{l_m}{VB}. \tag{23}$$

Obviously, the meshing point P (see Fig. 2) moves at a constant velocity along the pitch line of the hob in diagonal hobbing, in which every cutter tooth participates in hobbing equally and then stress or heat is uniformly distributed. Thus, hob life can be improved significantly.

6.2 Accuracy of Teeth Profile

As shown in Fig. 9, a pitch curve is drawn on the theoretical model of a gear in cross-section, which is then offset proportionally by a distance of 3 mm and 6 mm separately inwardly and outwardly [21]. Consequently, curves such as a, b, c, d, and e are formed. There are two intersections between each curve with both sides of each tooth, as shown in Fig. 9. Therefore, there are 350 intersections in all. The corresponding curves a, b, c, d, and e are curved slightly on the cross-section of the 3rd order elliptic helical gear hobbed using a miniature milling cutter on an NC milling machine. The absolute coordinates of the intersections mentioned above on the x-axis and y-axis can be measured by a coordinate measuring machine separately.
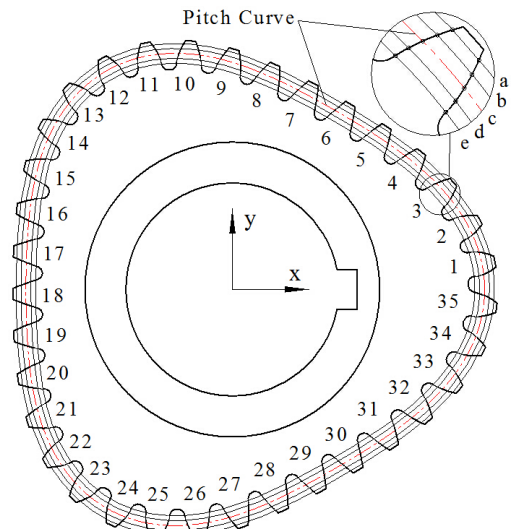
Fig. 9. *Detecting point of teeth profile in cross-section*

Order $\{\delta_x\}$ is a set of errors between the measured values and the theoretical ones on the x-axis, and $\{\delta_y\}$ is that for the y-axis. Frequency distribution of $\{\delta_x\}$ and that of $\{\delta_y\}$ are shown in Tables 2 and 3 separately. As shown in Fig. 10, an error-distribution image of $\{\delta_x\}$ and $\{\delta_y\}$ is developed with the median of intervals as a horizontal axis and frequency as a vertical one. From Fig. 10, it can be found that both $\{\delta_x\}$ and $\{\delta_y\}$ are basically at a normal distribution

[22], the errors of more than 99.43 % points measured are in the interval of [−0.100, 0.100], which implies that the actual teeth profiles are consistent with the theoretical ones and have a high precision. Moreover, the errors of measured values in 1st, 12th, 13th, 23th, 24th, and 35th tooth are concentrated in the interval [−0.140, −0.060) or (0.060, 0.140] in Tables 2 and 3. This indicates that the measured values on the teeth have a large error for the part of the pitch curve with a small curvature radius. That is to say, the larger the curvature radius of the part of pitch curve, the higher the precision of tooth accuracy.

Table 2. *Frequency distribution of $\{\delta_x\}$*

No.	Interval [mm]	Median [mm]	Freq.
1	[−0.140, −0.100)	−0.120	1
2	[−0.100, −0.060)	−0.080	19
3	[−0.060, −0.020)	−0.040	85
4	(−0.020, 0.020)	0	141
5	(0.020, 0.060]	0.040	84
6	(0.060, 0.100]	0.080	18
7	(0.100, 0.140]	0.120	2

Table 3. *Frequency distribution of $\{\delta_y\}$*

| No.	Interval [mm]	Median [mm]	Freq.
1	[−0.140, −0.100)	−0.120	1
2	[−0.100, −0.060)	−0.080	17
3	[−0.060, −0.020)	−0.040	83
4	(−0.020, 0.020)	0	149
5	(0.020, 0.060]	0.040	81
6	(0.060, 0.100]	0.080	19
7	(0.100, 0.140]	0.120	0
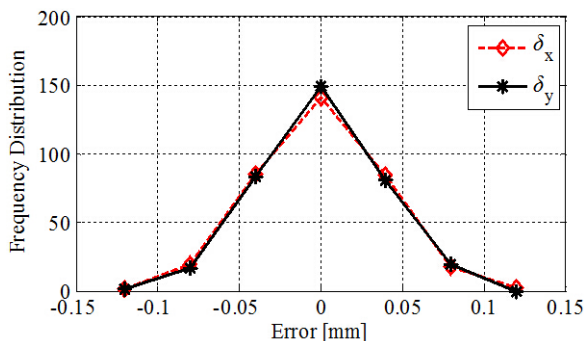
Fig. 10. *Error-distribution of $\{\delta_x\}$ & $\{\delta_y\}$*

6.3 Microtopography of Tooth Flank

As shown in Fig. 11, the 1st tooth flanks of the 3rd order elliptic helical gears obtained by the two hobbing methods are imaged respectively using a Scanning Electron Microscope (SEM, 5.0 kV 8.0 mm × 8.00 k). The tooth flank shown in Fig. 11a is cut using non-diagonal hobbing, in which the cutting marks are approximately parallel with the gear axis. When two gears with the same surface features mesh together, their cutting marks occlude mutually and usually make the gear train vibrate, which not only reduces the stability of the gear driving system, but also increase the system noise [23]. In some cases, some troubles such as gear vibration and ultimately result in failures can be caused [24]. The tooth flank shown in Fig. 11b is cut by the diagonal hobbing, in which the cutting marks are not parallel with the gear axis, and are mainly distributed as some S-shaped curves. Because of having different cutting-mark direction, pair of gears engage stably and do not occlude.
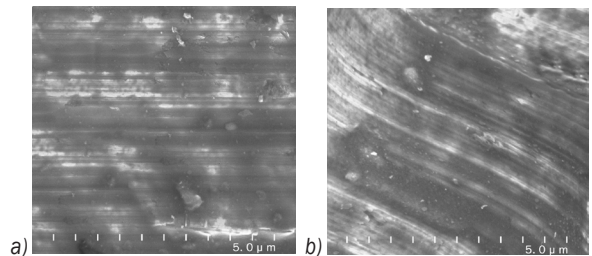
Fig. 11. *SEM image of tooth flanks; a) non-diagonal hobbing, b) diagonal hobbing*

7 CONCLUSIONS

Hobbing is a highly effective machining process. The traditional non-circular hobbing process keeps the hobs fixed in their axial positions, which means that the load and wear on the cutter tooth of the hob are extremely uneven. The hob life depends on the cutter tooth that has the largest amount of wear and thus hob life is extremely low.

1) The strategy of diagonal hobbing offers a possible solution, which can completely solve the issues mentioned. Moreover, four kinds of probable working conditions and linkage models have been provided, which have been verified by virtual hobbing. Their tool paths show that the tooth accuracies under the four working conditions are uniform.

2) Some conclusions drawn from the dynamics analysis: As for high-speed hobbing, scheme 'V' should be given priority in applications because it has better dynamic qualities of velocity and acceleration versus scheme 'U'. As for medium-low speed hobbing, both scheme 'U' and 'V' can be used, although scheme 'V' is better. The

speed and acceleration for every axle in scheme 'U' or scheme 'V' has no effect on the different rotating direction of the teeth. As a result, two implementation strategies including repeating axial shift and reciprocating axial shift have been offered. The latter has been used in this article because it leaves no connective cutting marks on the tooth flanks and has no idle travel of the hob compared to the former.

3) These hobbing experiments demonstrate that the linkage model in Eq. (19) and its implementation strategies are both accurate and feasible. Moreover, diagonal hobbing is superior to non-diagonal hobbing in that the hob life of the former is 3.68 times longer that of the latter and the micro-topography on the teeth surface of the former can be more stable for transmission.

8 NOMENCLATURE

a	acceleration [mm×s^{-2}]
A	semi-major axis [mm]
b	tooth width [mm]
e	eccentricity
K	lobe of hob
l	translational distance of tooling-rack midline [mm]
l_m	length of hobbing route [mm]
L	length [mm]
m	module [mm]
n	number of gears
r	polar radius [mm]
s	turned arc-length of pitch curve of gear billet [mm]
$S(o-xyz)$	machine coordinate system
$S_b(o_b-x_by_bz_b)$	cutting tool coordinate system
$S_c(o_c-x_cy_cz_c)$	workpiece coordinate system
T	hob life [s]
v	velocity [mm×s^{-1}]
VB	value of flank wear [mm]
VB_{per}	permissible value of flank wear [mm]
Z	number of teeth

Greek symbols

α	angular acceleration [rad×s^{-2}]
β	helical angle [rad]
φ	rotating angle [rad]
κ	symbol coefficient
λ	lead angle [rad]
μ	angle between polar radius and tangent of pitch curve [rad]
θ	polar angle [rad]
ω	angular velocity [rad×s^{-1}]
$\Delta\omega$	extra angular velocity [rad×s^{-1}]

Subscripts

b	hob
c	gear billet
d	hob axis
h	pitch circle of hob
max	maximum
n	normal parameter
t	transverse parameter
x	x-direction
y	y-direction
z	z-direction

Superscripts

n	normal component
*	resultant parameter

9 ACKNOWLEDGMENTS

10 REFERENCES

[1] Jia, J.M., Gao, B. (2012). A novel non-circular planetary differential for off-road vehicles. China Mechanical Engineering, vol. 23, no. 3, p. 346-348, **DOI:10.3969/j. issn.1004-132X.2012.03.021**. (in Chinese)

[2] Qian, M., Yu, G., Jiang, C., Zhao, Y. (2014). Work principle and parameter optimization of rice-seedling transplanter with non-circular gears. Transactions of the Chinese Society for Agricultural Machinery, vol. 45, no. 6, p. 64-69, **DOI:10.6041/j. issn.1000-1298.2014.06.011**. (in Chinese)

[3] Lin, C., Hou, Y., Gong, H., Zeng, Q., Nie, L. (2011). Flow characteristics of high-order ellipse bevel gear pump. Journal of Drainage and Irrigation Machinery Engineering, vol. 29, no.5, p.379-385, **DOI:10.3969/j.issn.1674-8530.2011.05.003**. (in Chinese)

[4] Chen, J.N., Zhao, H.C., Wang, Y., Xu, G.H., Zhou, M. (2013). Kinematic modeling and characteristic analysis of eccentric conjugate non-circular gear & crank-rocker & gears train weft insertion mechanism. Journal of Donghua University (English Edition), vol. 30, no. 1, p. 15-20.

[5] Litvin, F.L., Gonzalez-Perez, I., Fuentes, A., Hayasaka, K. (2008). Design and investigation of gear drives with non-circular gears applied for speed variation and generation of functions. Computer Methods in Applied Mechanics and Engineering, vol. 197, no. 45-48, p. 3783-3802, **DOI:10.1016/j.cma.2008.03.001**.

[6] Mundo, D., Gatti, G., Dooner, D.B. (2009). Optimized five-bar linkages with non-circular gears for exact path generation.

Mechanism and Machine Theory, vol. 44, no. 4, p. 751-760, **DOI:10.1016/j.mechmachtheory.2008.04.011**.

[7] Li, J.G., Wu, X.T., Mao, S.M. (2007). Numerical computing method of noncircular gear tooth profiles generated by shaper cutters. *The International Journal of Advanced Manufacturing Technology*, vol. 33, no. 11-12, p. 1098-1105, **DOI:10.1007/s00170-006-0560-0**.

[8] Liu, Y.Y. (2014). Research on Gear Shaping Strategy for Internal Helical Non-Circular Gears and Performance Analyses for Linkage Models. *Journal of Mechanical Science and Technology*, vol. 28, no. 7, p. 2749-2757, **DOI:10.1007/s12206-014-0514-7**.

[9] Liu, Y.Y. (2015). Study of Optimal Strategy and Linkage Model for External Non-Circular Helical Gears Shaping. *Proceedings of IMechE Part C: Journal of Mechanical Engineering Science*, vol. 229, no. 3, p. 493-504, **DOI:10.1177/0954406214536700**.

[10] Tan, W.M., Hu, C.B., Xian, W.J., Ou, Y. (2001). Concise mathematical model for hobbing non-circular gear and its graphic simulation. *Chinese Journal of Mechanical Engineering*, vol. 37, no. 05, p. 26-29, **DOI:10.3901/JME.2001.05.026**. (in Chinese)

[11] Tian, F.Y., Hu, C.B., Jiang, Y.C. (2011). The simplest mathematical model and simultaneous-control structure for hobbing helical non-circular gear. *Applied Mechanics and Materials*, vol. 42, p. 284-288, **DOI:10.4028/www.scientific.net/AMM.42.284**.

[12] Liu, Y.Y., Han, J., Xia, L., Tian, X.Q. (2012). Hobbing strategy and performance analyses of linkage models for non-circular helical gears based on four-axis linkage. *Strojniški vestnik - Journal of Mechanical Engineering*, vol. 58, no. 12, p. 701-708, **DOI:10.5545/sv-jme.2012.524**.

[13] Liu, Y.Y., Han, J., Xia, L., Zhang, G.Z. (2013). Research on Hobbing Process Strategy for Non-Circular Helical Gears and Performance Analyses for the Functional Models. *Transactions of the Chinese Society for Agricultural Machinery*, vol. 44, no. 5, p. 281-287, **DOI:10.6041/j.issn.1000-1298.2013.05.049**. (in Chinese)

[14] Gupta, K., Jain, N.K. (2014). Analysis and optimization of micro-geometry of miniature spur gears manufactured by wire electric discharge machining. *Precision Engineering*, vol. 38, no. 4, p. 728-737, **DOI:10.1016/j.precisioneng.2014.03.009**.

[15] Radi, H.A., Rasmussen, J.O. (2013). *Principles of Physics*. Springer, Berlin Heidelberg, New Delhi, **DOI:10.1007/978-3-642-23026-4**.

[16] Litvin, F.L., Fuentes, A. (2004). *Gear Geometry and Applied Theory*. Second ed. Cambridge University Press, New York, **DOI:10.1017/CBO9780511547126**.

[17] Vosoughifar, H.R., Dolatshah, A., Shokouhi, S.K.S., Nezhad, S.R.H. (2013). Evaluation of fluid flow over stepped spillways using the finite volume method as a novel approach. *Strojniški vestnik - Journal of Mechanical Engineering*, vol. 59, no. 5, p. 301-310, **DOI:10.5545/sv-jme.2012.669**.

[18] Santos, M.J.S.F., Santos, J.B.D. (2011). FPGA-based control system of an ultrasonic phased array. *Strojniški vestnik - Journal of Mechanical Engineering*, vol. 57, no. 2, p. 135-141, **DOI:10.5545/sv-jme.2010.178**.

[19] GB/T 28252-2012 (2012). *Hobs for Pre-Grinding Gear*. China National Standardization Management Committee, Beijing. (in Chinese)

[20] Editorial board for gearing book. (2004). *Gearing book*. Volume two. China Machine Press, Beijing.

[21] Elise, M. (2014). *Autodesk Autocad 2014 Fundamentals*. Createspace, New York.

[22] GB/T 4889-2008 (2008). *Statistical interpretation of data – Techniques of estimation and tests relating to means and variances of normal distribution*. China National Standardization Management Committee. Beijing. (in Chinese)

[23] Ognjanović, M., Kostić, S.Ć. (2012). Gear unit housing effect on the noise generation caused by gear teeth impacts. *Strojniški vestnik - Journal of Mechanical Engineering*, vol. 58, no. 5, p. 327-337, **DOI:10.5545/sv-jme.2010.232**.

[24] Ognjanović, M.B., Ristić, M., Vasin, S. (2013). BWE traction units failures caused by structural elasticity and gear resonances. *Technical Gazette - Tehnički vjesnik*, vol. 20, no. 4, p. 599-604.

Conceptual Design and Preliminarily Structural Analysis of Inflatable Basket for an Asteroid Capturing Satellite

Alessandro Ceruti[1,*] – Siro Pettenuzzo[2] – Marco Tuveri[3]

[1] Industrial Engineering Department - DIN, University of Bologna, Italy
[2] School of Engineering and Architecture, University of Bologna, Italy
[3] Interdepartmental Centre for Industrial Research in Aeronautics, University of Bologna, Italy

This paper presents a conceptual design of a satellite device to be used for capturing asteroids, based on inflatable structures. The mission requirements, the conceptual design, the methodology for the selection of the best solution, and simulations for the preliminarily structural analysis of the device are described within. Several finite element analyses have been carried out in order to find the best strategy to model flexible materials under internal pressure, and the device structure has been changed accordingly in order to obtain the best trade-off between weight and strength. This paper presents the sizing and the weight breakdown of the satellite inflatable components, which are quite complex to model with regards to the structural simulation. The results obtained seem to confirm the feasibility of such a structure and motivates further studies and experimental tests.

Keywords: conceptual design, inflatable structure, FEM, MADM, fabric, α damping

Highlights
- *Development of a methodology for conceptual design.*
- *CAD modelling and evaluation of different configurations.*
- *Tests with several FEM analysis strategies and settings.*
- *Preliminary sizing and shape prediction of a soft structure.*

0 INTRODUCTION

Several studies have been carried out to study a manned mission to capture asteroids and deflect them into a low earth orbit. This can be useful in developing technologies to deflect asteroids impacting the earth or to study the mineral composition of objects coming from deep space. The feasibility of such a space mission has been demonstrated through the studies by the Keck Institute [1] and [2], by NASA [3] and by several other authors, such as [4]. For instance, the driving idea of Keck's work is to capture an asteroid with a diameter of 7 metres, by launching into orbit a satellite with an inflatable structure to expand in space to envelope the rock. Several vehicles could be useful for launching into orbit such a satellite: e.g. the American Atlas V, the European Ariane V, the Japanese Mitsubishi H-IIA, and the Russian Zenit-2M are able to carry payloads up to 15,000 kg of mass, with a maximum diameter ca. 4 m to 4.5 m. This limit in diameter motivates the use of foldable or inflatable devices for space applications in which a large structure is needed. However, all these conceptual studies require a step into a more detailed design of the mission profile, on the systems to carry and on the structure of such a satellite. Details about the mission trajectory can be studied, following the classic equations of orbital mechanics [5]. However,

the design of the satellite configuration and structure needs a more inventive process in which the shape of the inflatable part of the satellite has to be sketched and sized. This paper focuses the attention on this latter aspect, describing the methodology to design and simulate the behaviour of the inflatable part of the satellite through finite element analysis (FEM). A great deal of literature can be found dealing with inflatable structures. The work in [6] presents the development of a mathematical approach to studying the mechanics of plain-woven fabrics, applied to inflated structures; a similar work by Apedo et al. [7] focuses the attention on the vibration modes of inflatable beams built with orthotropic woven fabric. Applications of inflated structures range from space and aeronautical [8] applications (e.g. inflated wings) to civil engineering (bridges with Tensairity technology) to food processing. In this latter topic, it is worth citing the work by [9] in which the design of inflatable open-ocean-aquaculture cages is carried out in a rigorous way, by applying the leading edge technologies related to the numerical modelling and simulation of inflatable structures. Focusing the attention on the modelling of inflatable structure for space applications, for instance, another paper [10] compares two off-the-shelf simulation codes (LS-DYNA and ADAMS) in predicting the behaviour of inflatable space structures. An example of the

*Corr. Author's Address: University of Bologna, DIN Department, Viale del Risorgimento 2, Bologna, Italy, alessandro.ceruti@unibo.it

341

design, FEM analysis and testing of an inflatable space structure is presented in [11], in which the development of an inflatable re-entry vehicle based on a cone-shaped configuration made by a series of inflated rings is described in theoretical, numerical and experimental aspects. The paper [12] shows a good agreement between simulation results obtained with the LS-DYNA code and the experimental tests on the airbag structure of the Orion crew module; the work by [13] also describes a review of the methods for the structural analysis of airbags, focusing the attention on the problem of reducing the effects of the landing on the Mars surface, topic faced by [14] as well. The use of inflatable structures and methods for its structural analysis are also described with reference to expandable lunar habitats [15], and to antennas for small Cubesat satellites [16]. The papers [17] and [18] represent some of the most recent studies on the structural analysis of inflatable structures for space applications. The concepts and experiences presented by these authors in the design and structural modelling of inflatable structures have been taken into account in the work described in this paper.

The structure of the paper is as follows: the first section describes the design requirements of the device, the second presents the deployment of the design phase and shows some sketches of the proposed configurations. After the selection of the most promising inflatable shape, the third section describes the methodologies explored to carry on the structural analysis and to set the thickness of this structure. A final section includes a conclusion and some comments on the most significant results obtained in this work.

1 DESIGN REQUIREMENTS

The aim of this work is to present a possible methodology to size and test the structure of the inflatable section of a satellite conceived to capture an asteroid. Following the studies by [1] and [2], attention was focused on the design of a structure to capture an asteroid of a free form shape, with a main length of 7 m, and a mass of about 500,000 kg; the real asteroid mass could range between 250,000 kg and 1,000,000 kg, depending on its composition [1]. A conceptual layout of the satellite components is presented in Fig. 1. The satellite core contains the inflatable structure during launch, compressed gas or chemical powders for inflation, electronics, batteries, thrusters, and propellant. A Stewart platform between the inflatable basket and the satellite core could be used to align the asteroid centre of gravity with the axis of symmetry of

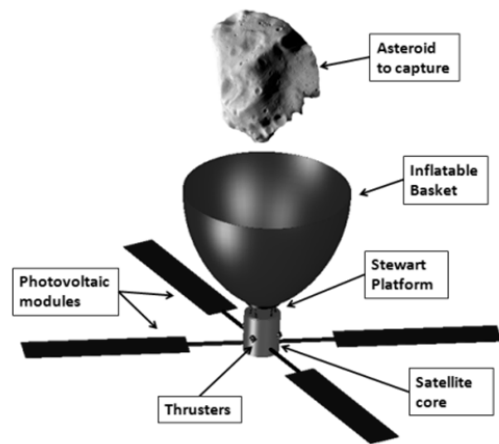the satellite itself to reduce eccentric effects during the thrust phase.

Fig. 1. *Conceptual layout of the device*

Fig. 2 presents the main dimensions of the satellite core, based on what is suggested by literature [1], and an average sizing of the basket.
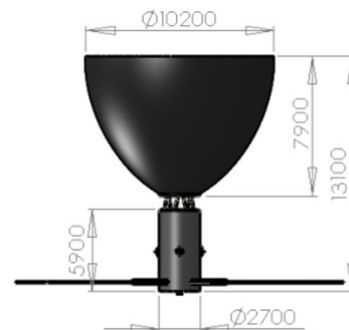

Fig. 2. *Average dimensions of the satellite*

The satellite should approach the asteroid, envelope it with the inflatable structure, and finally secure and block it inside the basket to change its trajectory: a complex docking algorithm [1] controlling the thrusters will be used to reduce the impact forces between the asteroid and the basket. The selected configuration is based upon a main inflatable structure shaped like a cone, with internal appendices that could be further pressurized up to touching the external surface of the asteroid; in such a manner, the contact force between the appendices and the asteroid assures a friction force blocking the rock into the satellite. A detailed design of the basket, starting from the above-described requirements is presented in the following. The materials for the basket have been initially selected according to the literature: a sandwich of fabrics in Vectran® and Kevlar® seems to be the most

effective solution available. The properties of these materials are included in the following Table 1. Thin thermal insulation layers in Aerogel® and airtight in Kapton® can also be added.

Table 1. *Material properties*

Name	Vectran	Kevlar
Elastic module [N/mm²]	103000	127500
Tensile strength [N/mm²]	2900	3600
Poisson's Coefficient [-]	0.3	0.34
Density [kg/m³]	1400	1400

2 CONCEPTUAL DESIGN AND METHODS FOR BEST SOLUTION DEFINITION

After the clarification of the design scope, the state-of-the art analysis, and the definition of design requirements, a set of conceptual sketches of possible configurations of the basket has been carried out. Finally, these shapes have been evaluated in order to select the most suitable one and to proceed with its structural sizing.

2.1 CAD Modelling of Configurations

Some conceptual configurations have been initially sketched by hand, and in the following they have been modelled within a computer-aided design (CAD) software. In the first configuration C1 (Fig. 3), named "Bubble", a thin basket with a conical shape is added by a set of spheres whose function is to soften the impact of the asteroid and further to block it inside the device.
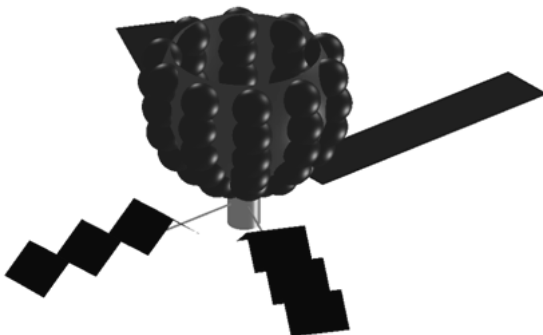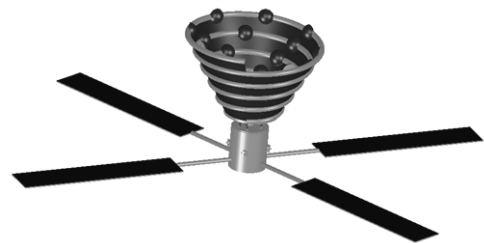

Fig. 3. *Conceptual CAD model of the "Bubble" configuration*

The second configuration C2 (Fig. 4), named "Reticular", is based on a reticular structure obtained through wires inclined 45° respect to the axis of the cone. They stiffen a series of 12 inflatable strips, each one equipped with 7 semi-spheres.
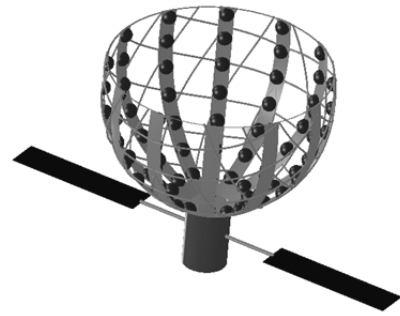
Fig. 4. *Conceptual CAD model of the "Reticular" configuration*

The third configuration C3 (Fig. 5), called "Spiral", is made by an inflatable spiral tube dressing all the cone, from the base to the top. Along the tube, a series of inflatable balls helps in damping the impact of the asteroid and the satellite, blocking it inside. A thin layer of fabric is connected to the tube to maintain the conical shape.

Fig. 5. *Conceptual CAD model of the "Spiral" configuration*

The fourth proposed configuration C4, called "Spheres & Cones", is similar to the first one, since it is based upon an inflatable cone; the main difference is that it is equipped with inflatable semi-spheres and large cones whose function is to block the asteroid inside.

Fig. 6. *Conceptual CAD model of the "Spheres & Cones" configuration*

2.3 MADM Approach to Select the Best Configuration

A Multi Attribute Decision Making (MADM) approach [19] and [20] has been followed to evaluate the most effective configuration. It will be sized and verified with FEM analysis in the following of the paper. The MADM's first step is to interview experts on the topic asking for the attributes they consider critical for a product. After the interview, a series of attributes are collected; similar concepts are usually condensed into a single attribute to reduce their number N to a manageable value.

Table 2. *MADM matrix of attributes relative importance (R.I.)*

	A_1	A_i	A_N	Sum	R.I.
A_1	$S_{1,1}$	$S_{1,i}$	$S_{1,N}$	$S_1 = \sum_{i=1}^{N} S_{1,i}$	$RI_1 = \dfrac{S_1}{SS}$
A_j	$S_{j,1}$	$S_{j,i}$	$S_{j,N}$	$S_j = \sum_{i=1}^{N} S_{j,i}$	$RI_j = \dfrac{S_j}{SS}$
A_N	$S_{N,1}$	$S_{N,i}$	$S_{N,N}$	$S_N = \sum_{i=1}^{N} S_{N,i}$	$RI_N = \dfrac{S_N}{SS}$
				$SS = \sum_{j=1}^{N} S_j$	

In the following, these attributes $(A_1, A_2, A_i, \dots, A_N)$ are listed in row and column in a matrix, as Table 2 shows. A score of 0 is assigned to the intersection between line and column if the attribute in the row (A_j) is less important than that in the column (A_i), 1 if the comparison is a draw, and 2 in the opposite case. Finally, the scores are summed row by row, and the result is assigned to the attribute in the row of the matrix. By summing all the scores of the single attributes and dividing the single attribute score (S_j) by this sum (SS), the relative importance of the attribute (RI_j) is found.

Afterward, each configuration is evaluated by assigning a score (V) from 1 to 5 to the satisfaction of each single attribute.

The final configuration suitability (FS) is found by multiplying the score times the relative importance $(R.I.)$ of the attribute and summing all these terms (see Table 3). The following methodology has been applied to the case study: after an interview with several experts in the field of space structures and missions, seven attributes for the basket have been detected as significant for the selection of the configurations, as can be seen in Table 4. The attributes (from A_1 to A_7)

have been evaluated using the matrix of Table 2, and relative importance indexes have been obtained.

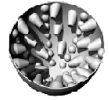**Table 3.** *MADM evaluation of configurations*

	A_1	A_i	A_N	Sum
Conf. #1	$V_{1,1}$	$V_{1,i}$	$V_{1,N}$	$FS_1 = \sum_{i=1}^{N} RI_i \times V_{1,i}$
Conf. #j	$V_{j,1}$	$V_{j,i}$	$V_{j,N}$	$FS_j = \sum_{i=1}^{N} RI_i \times V_{j,i}$
Conf. #M	$V_{M,1}$	$V_{M,i}$	$V_{M,N}$	$FS_N = \sum_{i=1}^{N} RI_i \times V_{M,i}$

Table 4. *List of attributes*

#	Description
A_1	Symmetry of the basket
A_2	Stability of the basket shape under external loads
A_3	Capability of blocking free form shaped asteroids
A_4	Folded volume (before expansion)
A_5	Easiness of inflation
A_6	Weight and surface
A_7	Retaining of debris eventually detached by asteroid

Finally, using the matrix described in Table 3, all the four configurations (C_1 to C_4) have been scored: the "Spheres & Cones" configuration obtained the best score, as Table 5 shows.

Table 5. *Relative importance of attributes and final suitability of configurations*

	R.I. [%]	Conf. #	Configuration icon	FS [-]
A_1	9.8			
A_2	21.6	C_1		3.94
A_3	19.6			
A_4	11.8	C_2		3.47
A_5	11.8			
A_6	9.8	C_3		3.1
A_7	15.7			
		C_4		4.16

2.3 Architecture and Layout of the Most Promising Solution

Following this evaluation phase, the configuration C_4 has been selected for further analysis and it has been modelled with a higher detail. The configuration C_1 achieved a good score, but the absence of cones would reduce the capability to block the asteroid; the configuration C_2 presents the drawback of releasing eventual debris detached from the asteroid in the outer space with the risk of impacts on the satellite structure or solar panels. Finally, the configuration C_3 is highly asymmetric and seems to be problematic in the case of heavy impacts.
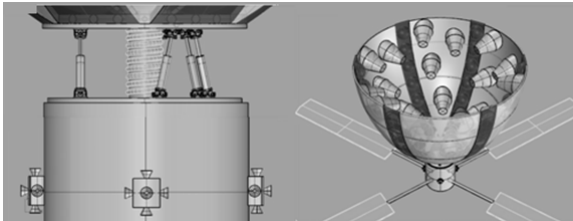

Fig. 7. *Satellite details (bubbles in dark strips)*

The dimensions of the semi-spheres have been preliminarily set equal to 1 m, while the cones present a height of 1.5 m, a base and top diameter of 1 m and 0.6 m respectively.

3 METHODOLOGIES FOR INFLATABLE STRUCTURAL ANALYSIS

Several strategies have been evaluated to size the structure and test its strength. The system, which is fully inflatable, is composed of a fabric made by a dense network of multilayer fibres of Vectran and Kevlar. The Nastran/Patran environment and the explicit solver of the Dytran module have been used to obtain the results presented in the following of the paper.

3.1 Load Evaluations and Rationale

The load evaluation on the structure of the satellite basket during a mission of asteroid capturing is a very complex task. Following the study [21] describing criticalities on trajectories for capturing missions, there are several issues to consider: the shape of the asteroid which can be spherical or more likely oblong, its inertia matrix and rotational speed, its solidity, possible impacts during docking, and the change in centripetal acceleration due to the rotational speed of the satellite during the engagement phases.

Due to all these uncertainties, it is extremely difficult to simulate a real scenario of docking. The structure we have conceived has a conical part, which should keep its shape during the capturing, and cones and spheres whose pressure depends on the gripping force needed to block the asteroid.

The amount of this force depends on the solidity of the rock, which can be affected by its rotational speed, the friction coefficient, which changes with the external shape and material of the rock, and the inertial loads due to the thrusters, which are usually very low. According to the study [1] and [21], it can take months or years to de-spin or de-tumble asteroids. Due to this framework of uncertainties, what we present in this paper is a comparative study of several structural implementations of the basket structure to evaluate the withstanding of the internal pressure and the final shape after inflation: a series of analysis has been carried out by simulating the stresses and deformations following the inflation of the basket with an increasing pressure; the main inflatable structure, consisting of two internal and external conical surfaces connected by ribs, has been constrained at the base to simulate the connection with the satellite. The structure has been tested with an internal proof pressure of 0.5 bar, i.e. a value similar to what presented in [12] where a pressure discharge test from 0.55 bar up to 0 bar in a time of 0.12 s is described for an inflatable space structure. As already stated, the inflation pressure of the spheres and cones is variable depending on the mission profile and asteroid features; however, some simulations for this appendices with the same pressure used for the main inflatable structure, which is considered a worst case study, have also been carried out.

3.2 Analysis with Equivalent Isotropic Material and 12 Vertical Ribs

In the first set of analyses, the structure has been simplified for FEM analysis by removing the semi-spheres and cones, which will be analysed later. Twelve vertical ribs (one every 30°) have been modelled to stiffen the structure, which is essentially composed of two parallel inflated conical surfaces (see Fig. 7). The ribs are flexible plain strips of the same material used for the envelope spanning between the internal and external conical surfaces. The mesh has been obtained panelling the surfaces of the basket and the internal ribs with triangular shell elements.
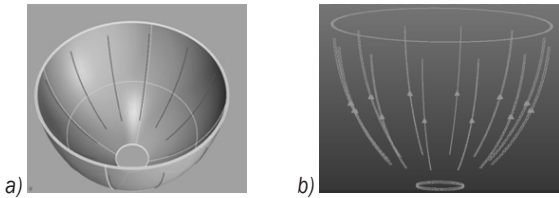
Fig. 8. *Structure with 12 vertical ribs; a) CAD and b) meshing of the ribs*

At first, as suggested by literature, **[12]**, a homogeneous isotropic material was used instead of a fabric modelling. The material model (Young modulus and Poisson modulus) adopted in this first set of tests, has been computed with the formula:

$$\bar{x} = \sum_{i=1}^{n} \frac{x_i \cdot s_i}{s_{tot}}, \qquad (1)$$

where x_i represents a generic property of the laminated; s_i is the thickness of the material layer, s_{tot} is the total thickness of the stacking. In these tests, the fabric thickness is set equal to 2 mm, with a mixture 1:1 of Kevlar and Vectran in thickness. From this non-linear analysis, a high deformation is noticed, since the structure withstands the pressure loads poorly: a maximum displacement of 1.7 m is detected, with a maximum stress of 1250 MPa (see Fig. 9), and some peaks up to 2380 MPa, close to the breaking stress of the material.
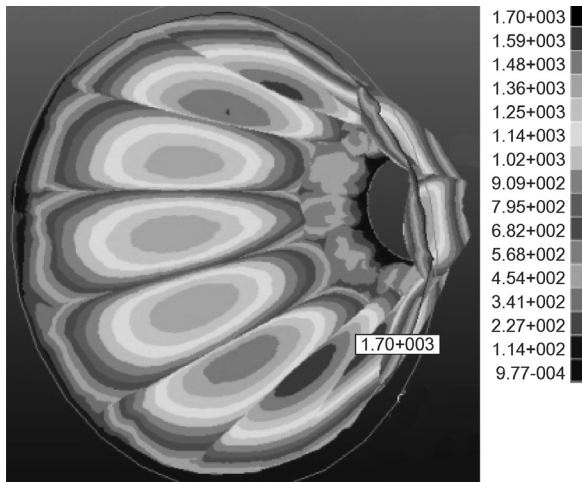
Fig. 9. *FEM analysis of the internal envelope only with 12 vertical ribs: displacements in mm*

This result is due to the modelling of the fabric with a homogenous isotropic material: it withstands both compression and traction loads, so that the element used for these simulations increases the stress due to the compression of the fabric. Following the

physics of the problem, the compression strength of the fabric is well below the tensile one, so that it does not present resistance to the compression. In this first set of tests with equivalent isotropic material, a Von Mises breaking criteria, which keeps into account both compression and tensile stresses, has been used:

$$\sigma_v = \sqrt{\frac{1}{2}[(\sigma_{11} - \sigma_{22})^2 + (\sigma_{22} - \sigma_{33})^2 + (\sigma_{33} - \sigma_{11})^2 + 6(\sigma_{12}^2 + \sigma_{23}^2 + \sigma_{31}^2)]}, \qquad (2)$$

where σ_v is the Von Mises stress, and σ_{ij} are the elements of the 3×3 stress matrix. With a thickness of the structure of 2 mm, the mass of the basket is 1188 kg (38 kg for the ribs, 579 kg for the external structure, 560 kg for the internal structure, 11 kg for the top and down closing edge surfaces).

3.3 Equivalent Isotropic Material and 24 Vertical Ribs

Following the goal of reducing the displacement of the structure under internal pressure, a second structural layout has been implemented with 24 vertical ribs, one every 15°, as Fig. 10 shows, and the same material properties, loads and constraints of the previous set of FEM analyses.
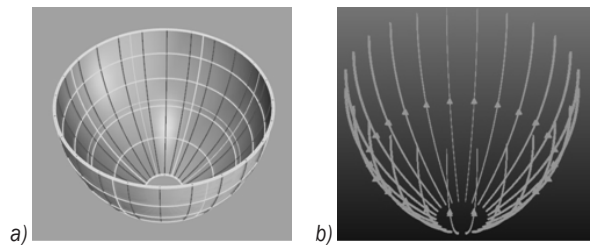
Fig. 10. *Structure with 24 vertical ribs; a) CAD and b)meshing of the ribs*
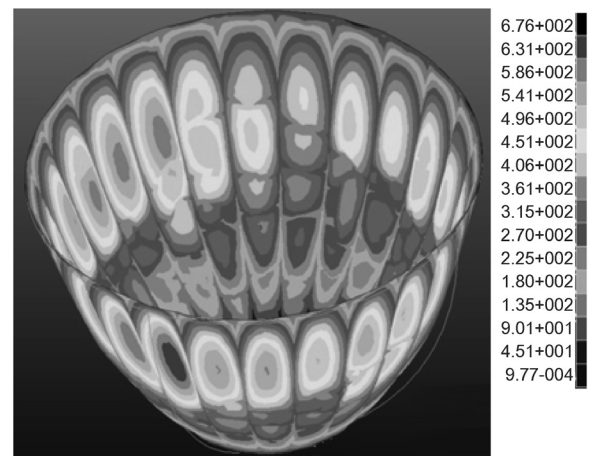
Fig. 11. *FEM analysis with 24 vertical ribs: displacements in mm*

By introducing 24 ribs, the structure displacement is reduced to 0.68 m: a peak stress of 2090 MPa in the basket internal part is observed. Similarly to the previous analysis, in this case the trend of the displacement of a test point of the structure also presents an oscillation (see Fig. 12), showing an instability in the solution and a partial convergence of the results. However, better results with respect to the 12 ribs case has been achieved.
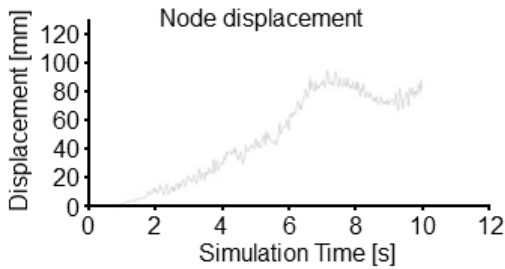

Fig. 12. *Convergence of the displacement of a node as a function of simulation time*

3.4 Basket with 9 Horizontal Ribs

The need for a reduction in structure weight has led to the testing of other configurations. As Fig. 13 shows, the basket has been stiffened with 9 horizontal parallel ribs, perpendicular to the basket vertical axis of symmetry.
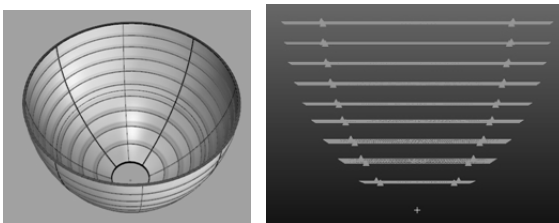

Fig. 13. *Structure with 9 horizontal ribs: CAD and meshing of the ribs*

The FEM analysis (Fig. 14) showed a maximum deformation of 292 mm, and a maximum stress of 1300 MPa. However, problems in solution stability and convergence remain; the structure is unstable under the pressure load, and an equilibrium is not found even for simulation times well beyond the end of the pressurization process.

3.5 Damping Coefficient and Modal Analysis

Following literature suggestions [22] related to analysis of non-linear structures [23], two methods can be followed in non-linear analysis requiring

damping: the α damping, and the global C-matrix or system damping.
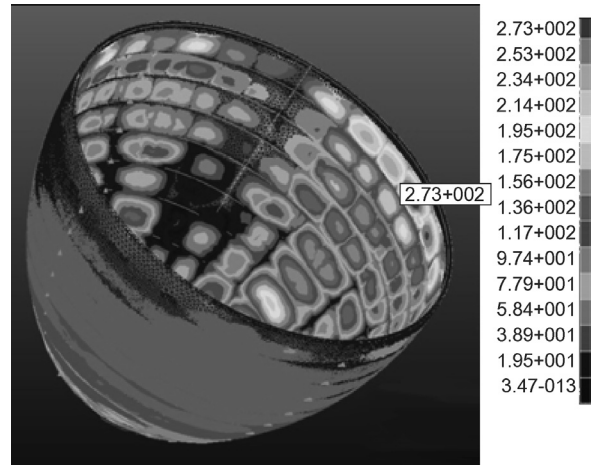

Fig. 14. *FEM analysis of the structure with 9 horizontal ribs: displacements in mm*

The C-matrix approach is based upon a mass spring system whose motion equation is:

$$Ma^n + Cv^n + F_{int}^n = F_{ext}^n. \qquad (3)$$

The M matrix represents the masses matrix, F_{int} the elastic internal forces due to springs' deformation, F_{ext} the external forces, and C is the damping matrix (diagonal).

In the α damping, selected in this study, the solver uses a single damping parameter, which is introduced in the central differences solution scheme. The equation is:

$$v^{n+1/2} = v^{n-1/2}(1-\alpha) + a^n \Delta t, \qquad (4)$$

where v represents the speed of the single node, a its acceleration, Δt the integration step, while α is the dynamic relaxing parameter. Literature, [19], suggests that the α coefficient should be equal to 5/3 times the critical damping of the whole system, or, in other words, 5/3 times the system natural frequency multiplied by the integration step Δt.

For instance, the natural frequency (f_i) of a single-degree-of-freedom system can be computed with:

$$f_i = \frac{\omega_i}{2\pi} = \frac{1}{2\pi}\sqrt{\frac{k_i}{m_i}}. \qquad (5)$$

When a complex structure with many degrees of freedom is analysed, usually the lowest natural frequency (f_1) is considered.

A modal analysis of the configurations with vertical and horizontal ribs has been carried out, aiming to find the natural frequencies of these structures (see Fig. 15).
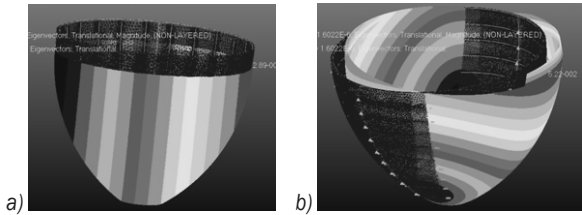

Fig. 15. *Basket deformations for the first natural frequency with a) vertical and b) horizontal ribs solutions*

For the structure with 24 vertical and 9 horizontal ribs, the first three resulting frequencies were found respectively: 1.465E-6, 2.28E-4, 3.945E-4, 1.60E-6, 1.5685E-6 and 1.28E-6.

It was possible to compute the α damping coefficient:

$$\alpha = \frac{5}{3} f_{nat} \Delta t. \tag{6}$$

The Δt used in the above equation has been set using the equation:

$$\Delta t = \frac{th}{\sqrt{E/\rho}}. \tag{7}$$

It represents the time a sound wave takes to pass through the thinnest element of the structure, represented by the fabric thickness. E is the elastic module of the material, ρ its density and th stands for the fabric thickness. Table 6 lists the computed values for the first natural frequencies (f_1) and α damping coefficients.

Table 6. *Damping coefficients*

Structure	f_1	Δt	α
Vertical ribs (24)	1.465E-6	2.90E-5	7.1E-11
Horizontal ribs (9)	1.602E-6	3.971E-5	1.06E-10

Some convergence tests have been carried out in order to check the structural behaviour of the basket during non-linear analysis. The theoretical value of the α parameter of relaxation (equal to 7.1E-11) does not provide solution convergence, so a systematic analysis was carried out to find a value providing the nodes displacement convergence. Five values of the α parameter were tested: 7.1E-11, 1E-5, 1E-4, 1E-3 and 1E-2.
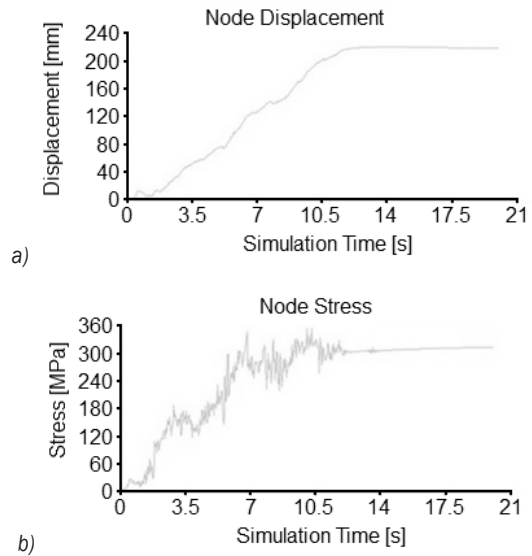
Fig. 16. *Example of a) node displacement, and b) stress convergence with α damping*

The best results have been obtained with α = 1E-4: the value suggested by literature seems to be too small, while the 1E-3, 1E-2 values provide an over-damped response of the structure. In this case, the analysis presents a stable value for nodes displacement and stress, as Fig. 16 shows. Nevertheless, as Fig. 17 shows, there are quite large zones where the compression stresses are high. As stated before, this is not a real effect since the fabric opposes a small resistance to the compression; according to the real material behaviour, the fabric deforms up to equilibrate stable configuration, keeping low compression stresses.

Fig. 17. *Vertical ribs configuration FEM analysis with damping coefficient: compression zones, Stresses in MPa*

3.6 Analysis with Fabric Model

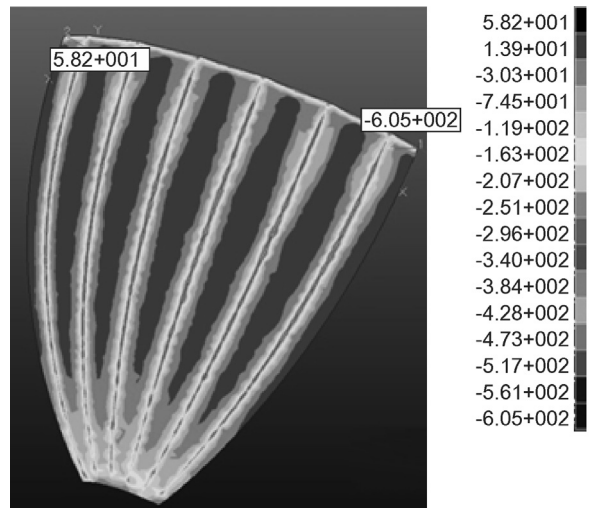The previously presented analysis showed that good structural behaviour can be obtained with the horizontal ribs configuration. It was also observed that the damping coefficient is fundamental in order to achieve the solution stability. However, to better simulate the compression behaviour of the material, a final improvement in the model should be carried out. The compression weakness of the fabric should be in fact considered to obtain a solution closer to the real physic of the problem (in [12] the compressing stress elimination setting of LS-DYNA was selected).
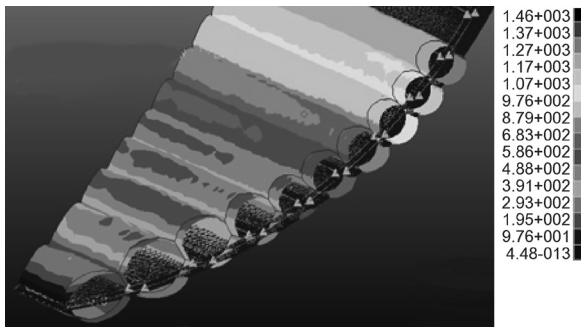
Fig. 18. *Horizontal ribs model FEM analysis with damping and fabric element: displacements in mm*

In a new set of tests, the structure with horizontal ribs was modelled with an orthotropic fabric material model, and a membrane element of Patran/Nastran, with a ±90° stacking: the fabric thickness was set equal to 2 mm, with an equal mixture of Kevlar and Vectran sheets and a symmetric lay-up with regards to the mid-plane.

The FEM analysis (see Fig. 18) showed behaviour consistent with the physics of the problem, and a maximum displacement of 1.46 m, with a tensile stress of 98.2 N/mm². The behaviour of displacements and stresses (as a function of time and inflation process) presents a very smooth trend up to the convergence to a final value. Thanks to the low values of stress in the structure, the thickness of the fabric was reduced to 0.5 mm, and further analyses following the Tsai-Hill criterion were carried out. With this new setting, a maximum displacement of 1.91 m (mainly vertical deformation of the structure), and a maximum tensile stress of 235 MPa in one of the sheets of Vectran (along the interface between rings where the horizontal ribs lie) have been detected. The structure assumes a shape based on a set of toroidal rings, whose section is circular, as expected with a uniform internal pressure (see Fig. 19).
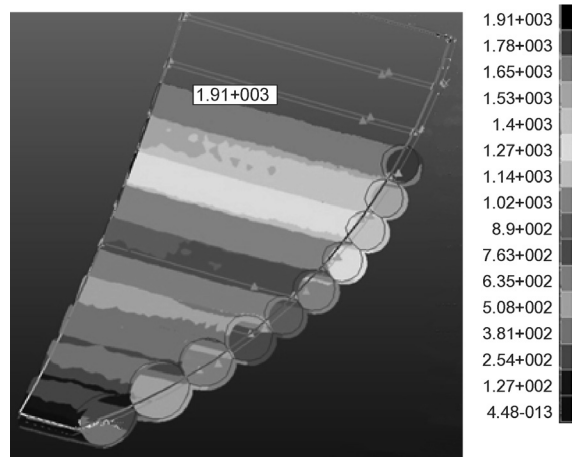
Fig. 19. *Horizontal ribs final configuration FEM analysis with damping and fabric element: displacements in mm*

The final mass breakdown of the inflatable structure, excluding semi-spheres and cones was computed to be 315 kg, divided into 145 kg for the external conical surface, 140 kg for the internal one, 30 kg for the ribs. The analyses have been carried out by increasing from 0 bar to 0.5 bar the internal pressure and continuing the simulation for 10 more seconds after the end of the inflation in order to let it completely relax.

3.7 Semi-Spheres and Cones

The final step of the analysis was to compute the stress over the semi-spheres and cones in order to size the thickness of its fabric. The cones and spheres are joined to the main structure, and eventually reinforcing strips can be adopted to increase the strength of the connection zone. After several FEM analyses, using a thickness of 0.5 mm and an internal pressure of 0.5 bar, the maximum tensile stress on the spheres and cones has been evaluated below 100 MPa (see Fig. 20), with maximum displacement of 0.1 m in the top of the cones. The weight of the cones and spheres has been evaluated equal to 100 kg, so that the mass of the inflatable part of the satellite structure is less than 420 kg. Due to the uncertainties in the load modelling (impacts of the asteroids, local peaks of stress, junctions, fatigue), the high coefficient of safety obtained with Tsai-Hill criterion for 0.5 bar pressure load seems to be acceptable, at least for preliminarily analyses.

Such a weight of the satellite inflatable part (Fig. 21) is concurrent with the mass breakdown proposed by [1] and justifies further studies and experimental

simulations to better detail the design of the inflatable basket.

a)

b)
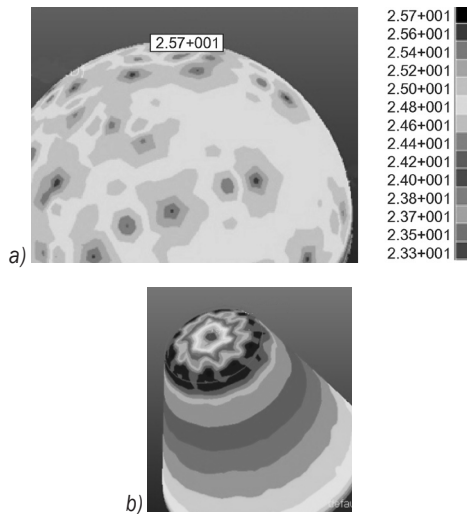
Fig. 20. *Horizontal ribs configuration FEM analysis with damping and fabric element: a) sphere: displacements in mm and b) cones: stresses, colour map from light (13.6MPa) to dark (75.5 MPa)*
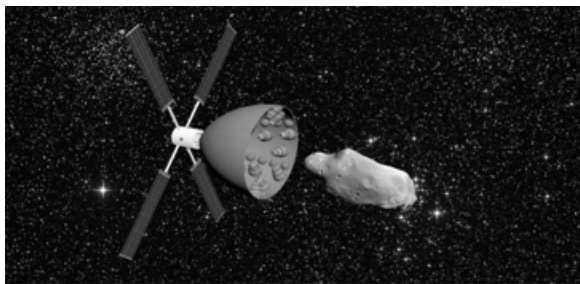
Fig. 21. *Artistic impression of the authors of the inflatable structure and satellite in space*

4 RESULTS DISCUSSION AND CONCLUSION

This paper presents a methodology to design, select, size and simulate, through FEM analyses, the inflatable section of a satellite whose mission is to capture an asteroid with a diameter of 7 m. Damping should be applied to the FEM model to obtain the convergence of the displacements and stresses: in this study, the α damping is adopted and values for the α coefficient higher than what suggested by literature seem to improve the convergence. A fabric model keeping into account the compression behaviour of the fabric is necessary to simulate the weakness in compression and the following reduced stresses, so that a membrane element is suggested in FEM analyses. The final weight of the structure obtained after this study is in agreement with conceptual studies found in literature [1]. A further reduction in

weight could be obtained with a better definition of the operative loads scenarios. The outcome of this study is the development of a methodology to rank possible configurations, the proposal of a shape for the inflatable basket, a list of guidelines to follow in FEM analysis of inflatable structures, and the definition of a feasible fabric thickness, valid for this case study. The use of inflatable structures for asteroids capturing presents weights compatible with the payload typical of a satellite, but further analysis and experimental tests to tune the FEM model are necessary. Further details, such as the modelling of the junction between fabric elements, and the simulation of impacts between asteroid and satellite should be better addressed in future works. Detailed trade-off studies to define the most suitable inflation pressure could be carried out once a real case-based simulation of asteroid capturing will be available in the relevant literature.

5 ACKNOWLEDGMENTS

6 REFERENCES

[1] Asteroid Retrieval Feasibility Study (2012) prepared for Keck Institute For Space Studies, California Institute of Technology, Jet Propulsion Laboratory, Pasadena, available at: *http://www.kiss.caltech.edu/study/asteroid/asteroid_final_report.pdf*, accessed, 2013-11-01.

[2] Brophy, J., Gershman, R., Landau, D., Polk, J., Porter, C., Yeomans, D., Allen, C., Williams, W., Asphaug, E. (2011). Asteroid Return Mission Feasibility Study, *47th AIAA/ASME/SAE/ASEE Joint Propulsion Conference & Exhibit*, American Institute of Aeronautics and Astronautics, **DOI:10.2514/6.2011-5665**.

[3] Stich, S. (2013). Asteroid Redirect Mission and Human Space Flight, Briefing to National Research Council Committee for Study on Human Space Flight (NASA-United States of America), available at *http://www.nasa.gov/pdf/756678main_20130619-NRC_Tech_Panel_Stich.pdf*, accessed on 2014-01-28.

[4] Landis, R.R., Abell, P.A., Korsmeyer, D.J., Jones, T.D., Adamo, D.R. (2009). Piloted operations at near-Earth object (NEO), *Acta Astronautica*, vol. 65, no. 11-12 pp. 1689-1697, **DOI:10.1016/j.actaastro.2009.04.022**.

[5] Curtis, H. (2005). *Orbital Mechanics for Engineering Students*. Butterworth-Heinemann, Oxford.

[6] Cavallaro, P.V., Johnson, M.E. and Sadegh, A.M. (2003). Mechanics of plain-woven fabrics for inflated structures.

Composite Structures, vol. 61, no. 4, p. 375-393, **DOI:10.1016/S0263-8223(03)00054-0**.

[7] Apedo, K.L., Ronel, S., Jacquelin, E., Tiem, S. (2014). Free vibration analysis of inflatable beam made of orthotropic woven fabric. *Thin-Walled Structures*, vol. 78, p. 1-15, **DOI:10.1016/j.tws.2013.12.004**.

[8] Lachenmeier, K.S., Murai, K. (2004). Development of three-dimensional reinforced membrane technology for high performance balloon and inflatable applications. *Advances in Space Research*, vol. 33, no. 10, p. 1732-1735, **DOI:10.1016/j.asr.2003.07.045**.

[9] Suhey, J.D., Kim, N.H., Niezrecki, C. (2005). Numerical modelling and design of inflatable structures: application to open-ocean-aquaculture cages. *Aquacultural Engineering*, vol. 33, no. 4, p. 285-303, **DOI:10.1016/j.aquaeng.2005.03.001**.

[10] Salama, M., Kou, C.P., Lou, M. (2000). Simulation of deployment dynamics of inflatable structures. *AIAA Journal*, vol. 38, no. 12 p. 2277-2283, **DOI:10.2514/2.896**.

[11] Lindell, M.C., Hughes, S.J., Dixon, M., Wiley, C.E. (2006). Structural analysis and testing of the inflatable re-entry vehicle experiment (IRVE). *47th AIAA/ASME/ASCE/AHS/ASC Structures, Structural Dynamics, and Materials Conference*, AIAA-2006-1803, **DOI:10.2514/6.2006-1699**.

[12] Timmers, R., Hardy, R., Welch, J. (2009). Modeling and simulation of the second-generation Orion crew module airbag landing system. *20th AIAA Aerodynamic Decelerator Systems Technology Conference and Seminar*, **DOI:10.2514/6.2009-2921**.

[13] Stein, J., Sandy, C. (2003). Recent developments in inflatable airbag impact attenuation systems for Mars exploration. *44th AIAA/ASME/ASCE/AHS Structures, Structural Dynamics, and Materials Conference*, AIAA-2003-1900, **DOI:10.2514/6.2003-1900**.

[14] Cadogan, D., Sandy, C., Grahne, M. (2002). Development and evaluation of the Mars pathfinder inflatable airbag landing system. *Acta Astronautica*, vol. 50, no. 10, p. 633-640, **DOI:10.1016/S0094-5765(01)00215-6**.

[15] Hinkle, J., Timmers, R., Dixit, A., Lin, J., Watson, J. (2009). Structural design, analysis, and testing of an expandable lunar habitat. *50th AIAA/ASME/ASCE/AHS/ASC Structures, Structural Dynamics, and Materials Conference*, **DOI:10.2514/6.2009-2166**.

[16] Babuscia, A., Corbin, B., Knapp, M., Jensen-Clem, R., Van de Loo, M., Seager, S. (2013). Inflatable antenna for cubesats: Motivation for development and antenna design. *Acta Astronautica*, vol. 91, p. 322-332, **DOI:10.1016/j.actaastro.2013.06.005**.

[17] Lampani, L., Gaudenzi, P. (2010). Numerical simulation of the behavior of inflatable structures for space. *Acta Astronautica*, vol. 67, no. 3-4, p. 362-368, **DOI:10.1016/j.actaastro.2010.02.006**.

[18] Cui, D., Yan, S., Guo, X., Chu, F. (2012). An overview of dynamics modeling of inflatable solar array. *Energy Procedia*, vol. 14, p. 1967-1972, **DOI:10.1016/j.egypro.2011.12.1195**.

[19] Rao, R.V. (2007). *Introduction to multiple attribute decision-making (MADM) methods - decision making in the manufacturing environment*, Springer, London, p. 27-41.

[20] Ceruti, A., Marzocca, P. (2014). Conceptual approach to unconventional airship design and synthesis. *Journal of Aerospace Engineering*, vol. 27, no. 6, **DOI:10.1061/(ASCE)AS.1943-5525.0000344**.

[21] Joldes, G.R., Wittek, A., Miller, K. (2009). Computation of intra-operative brain shift using dynamic relaxation. *Computer Methods in Applied Mechanics and Engineering*, vol. 198, no. 41-44, p. 3313-3320, **DOI:10.1016/j.cma.2009.06.012**.

Vsebina

Strojniški vestnik - Journal of Mechanical Engineering

Razširjeni povzetki

Osebne vesti

Ročni optični sistem za merjenje topografije kože z uporabo Fourierjevo transformacijske profilometrije

Jernej Laloš* – Marko Mrak – Urban Pavlovčič – Matija Jezeršek

Univerza v Ljubljani, Fakulteta za strojništvo, Slovenija

V članku je predstavljena nova ročna optična naprava, ki uporablja Fourierjevo transformacijsko profilometrijo z belo svetlobo za merjenje topografije kože.

V medicini in kozmetiki se pojavlja potreba po natančnem, hitrem, enostavnem in široko uporabnem sistemu za tridimenzionalno *in-vivo* merjenje površine kože. Taka optična naprava bi dajala natančne in konsistentne informacije o topografiji in barvi kože, pri čemer bi bilo brezdotično in neinvazivno merjenje globine njena najpomembnejša novost.

Najbolj praktične in zato tudi najbolj razširjene metode za *in-vivo* analizo površine kože spadajo v kategorijo tako imenovanih projekcijskih površinskih topografij – ena izmed takih merskih metod je Fourierjevo transformacijska profilometrija. Pri tej metodi se na merjeno površino projicira droben črtast vzorec, nato se posname sliko te projekcije, naposled pa se z ustreznim računalniškim programom posneto sliko obdela.

Posneta slika je sestavljena iz množice merskih točk in se interpretira kot množica vrstic, pri čemer vsaka vrstica predstavlja signal intenzitete svetlobe, ki je moduliran v fazi in amplitudi, in ima neko prostorsko nosilno frekvenco. Signal iz vsake vrstice se razvije v Fourierjevo vrsto, prostorsko Fourierjevo transformira, filtrira okoli nosilne frekvence ter inverzno Fourierjevo transformira v prečiščen kompleksni signal. V argumentu tega signala se skriva fazni zamik, ki vsebuje informacijo o globinskem položaju merskih točk. Informacijo o ravninskem položaju merskih točk pa se enostavno prebere iz njihovih položajev na sliki. Tridimenzionalna oblika površja se tako rekonstruira iz ene same slike.

Naprava je bila razvita predvsem za natančno in objektivno ocenjevanje izgleda površine kože pred raznimi laserskimi terapijami ter po njih. V iskanju enostavne, dostopne in cenovne ugodne zasnove je bila ta naprava povečini razvita in sestavljena iz tržno dostopnih produktov. Tako temelji na digitalnem zrcalnorefleksnem (DSLR) fotoaparatu Nikon D90 z vgrajeno bliskavico kot izvorom svetlobe. Fotoaparat dopolnjuje optični sistem s projektorjem, ki projicira Ronchijev črtni vzorec na merjeno površino, in objektivom, ki preslika sliko vzorca na senzor fotoaparata.

Meritve z novo napravo so bile izvedene na petih vzorcih (ki so skupno pripadali trem ljudem) kože na obrazu – pred lasersko terapijo kože in po njej. Smisel te terapije je glajenje kože; njeni učinki na hrapavost vzorcev pa so bili eksperimentalno merjeni in ocenjevani. Ker je koža polprosojna in nehomogena, je bil na vzorce nanešen kožni puder, ki je bistveno izboljšal njene optične lastnosti za tako meritev.

Topografija kože je v tej analizi opisana s štirimi parametri hrapavosti površine: s povprečnim absolutnim odstopanjem R_a, s povprečnim kvadratnim odstopanjem R_q, z asimetričnostjo R_{sk} in s sploščenostjo R_{ku}. Za njihovo določitev je bilo najprej potrebno izračunti idealizirano referenčno površino kože, ki je povsem gladka.

Izračunani parametri hrapavosti površine kože so pokazali, da ima večina vzorcev povprečno absolutno odstopanje R_a med 45 μm in 80 μm ter povprečno kvadratno odstopanje R_q med 55 μm in 110 μm. Parametri tudi kažejo, da imajo vzorci kože večinoma nizke vrhove in globoke vdolbine ($R_{sk} < 0$) ter da so ti vrhovi in vdolbine relativno koničasti ($R_{ku} > 0$).

Kar se tiče laserske terapije in njenih učinkov na hrapavost površine kože, je jasno razvidno, da imajo vzorci po terapiji izrazito manjše vrednosti parametrov R_a in R_q kot pred njo. To nakazuje, da ima laserska terapija želen učinek in resnično zmanjšuje hrapavost kože. Pri primerjavi ostalih dveh parametrov, R_{sk} in R_{ku}, pa se ne more povedati nič gotovega.

Rezultati so tako pokazali zmožnosti in predvsem uporabnost razvitega optičnega sistema za merjenje topografije kože.

Ključne besede: Fourierjevo transformacijska profilometrija, optična triangulacija, topografija kože, parametri hrapavosti površine

---

*Naslov avtorja za dopisovanje: Univerza v Ljubljani, Fakulteta za strojništvo, Aškerčeva 6, 1000 Ljubljana, Slovenija, jernej.lalos@fs.uni-lj.si

Raziskava razvoja rezalne fronte abrazivnega vodnega curka z uporabo modela dvodimenzionalnega celičnega avtomata

Marko Jerman[1],* – Joško Valentinčič[1] – Andrej Lebar[1,2] – Henri Orbanić[1]

[1] Univerza v Ljubljani, Fakulteta za strojništvo, Slovenija
[2] Univerza v Ljubljani , Zdravstvena fakulteta, Slovenia

Za obdelovance izdelane z abrazivnim vodnim curkom (AVC) je značilna brazdava površina, usmerjena v nasprotni smeri rezanja. Ukrivljenost in debelina brazd sta v glavnem odvisni od materiala obdelovanca, prereza AVC, njegove intenzitete ter hitrosti rezanja. Proces odvzemanja materiala vsebuje erozijo trdnih delcev in ga je zaradi kompleksnosti težko teoretično popisati. Posledično je bilo razvitih veliko modelov, ki skozi simuliranje procesa rezanja z AVC skušajo izboljšati poznavanje procesa. Glavni izziv predstavlja razviti model, ki dobro popisuje nastanek brazd, katerih nastanek želimo zmanjšati.

Pojav nastanka brazd smo raziskovali posredno, z uporabo modela dvodimenzionalnega celičnega avtomata (CA). Za izračun oblike rezalne fronte model CA uporablja naslednje vhodne parametre: hitrost rezanja, jakost AVC in vrsto materiala. Proces rezanja smo popisali v obliki pravil CA z uporabo poenostavljenih modelov odvzema materiala in širjenja toka AVC. Pravila zajemajo sposobnost AVC, da erodira material obdelovanca in obratno, odpornost materiala na proces erodiranja.

Predstavljeni model upošteva preusmeritev toka AVC ob stiku z materialom, kar omogoča simuliranje situacij, kjer obdelovanca, zaradi previsoke rezalne hitrosti, curek ne prereže. Tega scenarija z uporabo prejšnjega modela ni bilo možno simulirati, ker je baziral izključno na energijskem modelu, ki ni upošteval vpliva toka abraziva ob rezalni fronti. V realnosti, pri dovolj velikih rezalnih hitrostih in določeni debelini materiala, obdelovanca ne prerežemo, četudi ima AVC dovolj energije za odvzem materiala. Pojav je posledica preusmeritve curka na dnu zareze in ne zmanjšanja jakosti AVC.

V prispevku smo pokazali, da lahko z uporabo CA uspešno popišemo proces rezanja z AVC za različne materiale. Za uspešno simuliranje razvoja rezalne fronte ob spreminjanju procesnih parametrov je potrebno ustrezno določiti mehanizme odvzema materiala in toka AVC. Model odvzema materiala zajema proces erozije s trdimi delci in njihovimi parametri, medtem ko model toka AVC upošteva tako energijski potencial kot tudi smer toka curka. Na ta način je možno z modelom predvidevati spremembe smeri toka AVC, primere, kjer AVC obdelovanca ne prereže in učinkovitost rezanja različnih materialov. Pokazali smo tudi, da je zaradi majhnih vpadnih kotov abrazivnih zrn na rezalni fronti, odvisnost med vpadnim kotom in stopnjo odvzema materiala, ki se uporablja za žilave materiale, na mikro skali možno uporabiti tudi za krhke materiale kot je steklo. V primerjavi z ostalimi modeli je glavna prednost metode CA poenostavljen in učinkovit model makro-mehanizma rezanja z AVC, ki ga lahko uporabimo za nadaljnje študije procesa. Zaradi popisa problema v 2D prostoru lahko z modelom le delno potrdimo vpliv oblike površine rezalne fronte na nastanek brazd. Mehanizem nastanka brazd je namreč tri dimenzionalni problem, zaradi česar je potrebno za popolni popis mehanizma, model CA razširiti v 3D prostor, kar se izvede z uporabo dodatnih enačb za popis tretje dimenzije.

Model smo potrdili s preverjanjem trenda ukrivljenosti brazd na rezalni fronti pri različnih vhodnih parametrih. Predvidena ukrivljenost brazd na rezalni fronti se dosledno ujema z odzivom v realnem procesu. Predstavljeni model predstavlja korak v smeri modeliranja mehanizma nastanka brazd v 3D prostoru.

Ključne besede: abrazivni vodni curek, rezalna fronta, nastanek brazd, celični avtomati, simuliranje

*Naslov avtorja za dopisovanje: Univerza v Ljubljani, Fakulteta za strojništvo, Aškerčeva 6, 1000 Ljubljana, Slovenija,marko.jerman@fs.uni-lj.si

Numerični izračun profila zob zobnika z valovito razdelno ploskvijo

Chao Lin* – Dong Zeng – Xianglu Zhao – Xijun Cao

Univerza v Chongqingu, Državni laboratorij za mehanske prenose, Kitajska

Zobniške dvojice z valovito razdelno ploskvijo so nova vrsta zobniških dvojic. Sestavljene so iz neokroglega pastorka in zobnika z valovito razdelno ploskvijo, prenašajo pa vrtilno gibanje sekajočih se osi. Različne zasnove omenjenih zobnikov so predmet številnih raziskav in članek podaja numerični izračun profila zob z namenom izpopolnitve teorije teh zobnikov, postavitve natančnega modela zobnikov in njihove vpeljave v tehnično prakso.

Profil zob je bil preučen z numerično analizo na računalniku. Pri reševanju so bile uporabljene naslednje raziskovalne metode:

1) Izpeljani so bili izrazi za poljubno krivuljo na površini valja, ki je bila osnova za razdelno ploskev.

2) Na podlagi načela transformacije koordinat, teorije ubiranja, teorije premika krivulj idr. so bile izpeljane enačbe razdelne ploskve in normalnih ekvidistančnih krivulj. Izračunana je bila tudi razdelna krivulja oblikovnega rezkarja in njena presečišča s prej omenjenimi krivuljami. Sečišča je mogoče poiskati z enačbo ubiranja, s katero dobimo točke na profilu zoba.

3) Teoretični in eksperimentalni podatki so bili obdelani po postopkih generiranja ubirnice in analize napak, določeno pa je bilo tudi odstopanje med teorijo in eksperimentom oz. napaka kot merilo za ugotavljanje natančnosti strojne obdelave.

Rezultat opisanega raziskovalnega procesa je postopek za konstruiranje zobnikov z valovito razdelno krivuljo v cilindričnem koordinatnem sistemu. Numerično izračunan profil zoba je natančnejši in ima manjšo napako, s tem pa izpolnjuje konstrukcijske zahteve v inženirski praksi. Natančnejši model ni le osnova za izdelavo in merjenje omenjenih zobnikov, ampak tudi izhodišče za raziskave površine in oblike zob.

Rezultati kažejo, da je uporabljena metoda za izračun profila zob pravilna in primerna za določanje profila zob poljubnega zobnika.

Prihodnje raziskave bodo usmerjene v izboljševanje natančnosti numerične metode. Nova smer pri raziskavah zobnikov z valovito razdelno ploskvijo bo lahko uporaba te metode v praksi in vzpostavitev metod za vrednotenje. Zelo dejavno je tudi raziskovalno področje, ki se ukvarja s praktično uporabo tovrstnih zobnikov.

Članek predstavlja novo splošno numerično metodo za izračun profila zob zobnikov z valovito razdelno ploskvijo, ki je lahko pomembno orodje za modeliranje, obdelavo, analizo merilne napake ipd. V članku je predstavljena tudi metoda za preučevanje zobnikov posebnih oblik.

Ključne besede: cilindrične koordinate, zobnik z valovito razdelno ploskvijo, numerični izračun, profil zoba, analiza napak

---

Tridimenzionalna karakterizacija abrazijske odpornosti betonov z uporabo laserske profilometrije

Dominik Kozjek[1] – Urban Pavlovčič[1] – Andrej Kryžanowski[2] – Jakob Šušteršič[3] – Matija Jezeršek[1,*]

[1] Univerza v Ljubljani, Fakulteta za strojništvo, Slovenija
[2] Univerza v Ljubljani, Fakulteta za gradbeništvo, Slovenija
[3] Inštitut IRMA, Slovenija

Ena izmed metod karakterizacije odpornosti betonov na abrazijo je metoda ASTM C1138. Pri njej z vrtinčenjem vode in jeklenih kroglic simuliramo interakcijo med betonom in delci, ki jih nosi vodni tok. Rezultat preizkusa je povprečna obrabna globina. Metoda je uspešna pri manj odpornih betonih, medtem ko se pri betonih visoke kvalitete, kjer so obrabne globine majhne, rezultati pogosto nahajajo znotraj merilne negotovosti merjenja obrabe. Zato je kaže potreba po izboljšani natančnosti, ki jo je možno doseči z laserskim tridimenzionalnim merjenjem obrabljene površine. Poleg tega z izmero reliefa obrabljene površine tudi bolje razumemo fizikalne procese ob interakciji jeklenih kroglic s površino betona, gibanja jeklenih kroglic in sam proces abrazije.

V članku predstavljamo dopolnitev metode, kjer površino vzorca izmerimo s 3D merilnikom na osnovi laserske triangulacije, meritve analiziramo in tako pridemo do podatkov o spremembah obrabne globine v posameznih časovnih intervalih. Merilnik sestoji iz laserskega projektorja, ki projicira svetlobno ravnino, in kamere, ki pod triangulacijskim kotom opazuje nastalo presečno krivuljo. Ta je na zajeti sliki deformirana glede na obliko osvetljenega dela površine. Na delovni razdalji 800 mm znaša merilno območje 500 × 370 mm², izmeri 400.000 točk z natančnostjo 0,14 mm, celotna izmera pa traja 8,2 sekunde.

Za testiranje so bili uporabljani betonski vzorci cilindrične oblike, premera 295 mm in višine 100 mm. Pred 3D merjenjem so bili pozicionirani v merilni sistem; tri podporne točke so uporabljene za ponovljivo pozicioniranje v Z meri, dve stranski podpori pa za pravilno rotacijo okrog Z osi in pozicioniranje v XY ravnini. Merilni interval je bil s standardnih 12 skrajšan na 3 ure. Z namenom izboljšanja natančnosti smo ob posameznem času vzorec izmerili desetkrat, ter izmerjene površine povprečili. Na podlagi te površine je bila izračunana povprečna obraba površine in mesto maksimalne obrabe, povprečna obraba pri različnih radijih in celotna prostornina odstranjenega materiala.

Evaluacija merilnika in metode je bila opravljena z analizo ponovljivosti merjenja in primerjavo rezultatov z rezultati konvencionalne metode. Pri analizi ponovljivosti je bilo ugotovljeno, da je standardna deviacija razlik pod 0,14 mm, kar je več kot velikostni razred pod spremembami v enem časovnem intervalu. Primerjava obeh metod je bila prikazana z Bland-Altmanovim diagramom. Razlika med obema metodama raste s povečevanjem količine odstranjenega materiala, a lahko velik del pripišemo netočnostim pri določevanju premera in višine vzorcev in posledično netočni konverziji prostornine v maso. A če pretvorimo povprečno spremembo teže v posameznem intervalu, ta ustreza 10 mm obrabe, medtem ko je točnost merjenja 0,1 mm. Na podlagi tega lahko zaključimo, da je metoda po točnosti primerljiva s konvencionalnimi metodami, poleg tega pa omogoča tudi topološko karakterizacijo abrazije.

Ključne besede: obraba površine betonov, abrazijska odpornost, tridimenzionalno merjenje, laserska triangulacija

*Naslov avtorja za dopisovanje: Univerza v Ljubljani, Fakulteta za strojništvo, Aškerčeva 6, 1000 Ljubljana, Slovenija, matija.jezersek@fs.uni-lj.si

Numerično kuhanje za pripravo pasteriziranih mehko kuhanih jajc

Marjan Jenko

Univerza v Ljubljani, Fakulteta za strojništvo, Slovenija

Razvoj novega termičnega procesa in naprave za pripravo pasteriziranih mehko kuhanih jajc je zahteval tudi študijo občutljivosti dinamike temperaturnega polja v kurjem jajcu ob segrevanju na njegove snovno dimenzijske lastnosti. Za ta namen je razvit simulator časovno odvisnega konduktivnega prehajanja toplote v dveh dimenzijah za osno simetričen objekt. Poudarek je na hitrosti računanja in na nadgradljivosti funkcionalnosti simulatorja. Eden od ciljev je simulacija, ki je bistveno hitrejša od termičnega procesa v realnem času. To omogoča sodelovanje simulacije scenarijev v krmiljenju procesov.

Zadnjih 30 let za simulacijo prehajanja toplote uporabljamo metodo končnih elementov (MKE) in v manjšem obsegu tudi metodo končnih razlik (MKR). Pri obeh metodah najprej določimo simulacijsko mrežo. Z obema metodama izračunamo temperature v vseh mrežnih vozliščih naenkrat s pomočjo reševanja sistema enačb. Za računanje stacionarnega prehajanja toplote je to optimalen pristop. Tranzientna simulacija, oziroma računanje prehodnih pojavov, pa je časovno zahtevno, saj za vsak trenutek t računamo vse temperature mrežnih vozlišč z reševanjem sistema enačb. Tak pristop k simuliranju toplotnega prehodnega pojava je na današnjih in jutrišnjih računalnikih počasnejši od prehajanja toplote v realnem času.

Za doseganje hitrosti simuliranja tranzientnega prehoda toplote je potrebno reševanje sistema enačb za vsak čas t pohitriti ali pa nadomestiti s postopkom z manj računanja. K prvemu inkrementalno prispeva stalen razvoj strojne opreme, v tem prispevku pa je prikazan postopek z manj računanja. Z lokalnim računanjem Fourierove enačbe prehajanja toplote za vsak čas t prehodnega pojava tranzientno simulacijo v primerjavi z MKE pohitrimo za več kot velikostni red, na danem primeru za 2 velikostna reda. Simulacija verifikacijskega primera je tudi na skromnejši platformi lahko 10 krat hitrejša od termičnega procesa v realnem času. MKE in MKR pa ostajata v prednosti pri hitrosti računanja stacionarnega prehajanja toplote.

Tranzientne simulacije prehajanja toplote v kurjem jajcu pokažejo, da na hitrost segrevanja najbolj vplivata velikost jajca in velikost rumenjaka, manj pa debelina lupine, položaj rumenjaka, formiranje zračnega žepa s staranjem jajca, spremembe toplotne prevodnosti in kapacitivnosti beljaka ob delni koagulaciji. Določitev občutljivosti dinamike temperaturnega polja na snovno geometrijske lastnosti jajca je nujen korak v razvoju termičnega procesa za izdelavo pasteriziranih mehko kuhanih jajc. Zahteve so namreč kontradiktorne: rumenjak ne sme koagulirati, za več velikostnih razredov pa je potrebno zmanjšati eventuelno okužbo s salmonelo in preostanek salmonel mora biti bistveno oslabljen. Organoleptične lastnosti procesiranih jajc in referenčne bakterijske meritve v pooblaščenem institutu Fresenius potrjujejo ustreznost novo razvitega termičnega procesa, udejanjenega v napravi Zlato jajce.

Na simulacijah referenčnih objektov bo potrebno ugotoviti velikost odstopanj med simulacijo z MKE in predstavljeno metodo, za katere pa že po simulacijah občutljivosti spreminjanja toplotnega polja v kurjem jajcu na snovno geometrijske parametre ugotavljamo, da so lahko dovolj majhna – kriterij zavisi od zahtev konkretne naloge.

Ključne besede: tranzientna simulacija prehajanja toplote, Fourierov zakon prevajanja toplote, termično procesiranje hrane, simulacija s fiksno mrežo, pasterizirana mehko kuhana jajca

---

Strategija in modeli šestosnega diagonalnega odvalnega rezkanja neokroglih zobnikov s poševnim ozobjem

Youyu Liu[1,2,*] – Jiesheng Diao[1,2]
[1] Politehnika Anhui, Šola za strojništvo in avtomobilsko tehniko, Kitajska
[2] Politehnika Anhui, Institut za robotiko AHPU, Kitajska

Odvalno rezkanje je visokoučinkovit obdelovalni postopek. Pri tradicionalnem neokroglem odvalnem rezkanju je aksialni položaj orodja nespremenljiv, obremenitve in obraba zob odvalnega rezkarja pa so zato izjemno neenakomerne. Življenjska doba odvalnega rezkarja je zelo kratka in odvisna od tistega zoba, ki se najbolj obrablja. Za razrešitev teh problemov je bila razvita shema sočasne šestosne obdelave po načelu diagonalnega odvalnega rezkanja.

Rezkar se med postopkom sočasnega šestosnega odvalnega rezkanja nenehno premika vzdolž svoje osi, tako da pri obdelavi sodelujejo vsi zobje rezkarja in ni pokvarjeno originalno sočasno petosno gibanje. Dolžine osi mnogih odvalnih rezkarjev običajno ne izpolnjujejo zahtev za obdelavo zobnikov, saj se rezkar giblje samo v eni smeri. Pri velikih hitrostih je mogoče uporabiti metodo ponavljajočega se aksialnega premika. Rezkar sprva reže vzdolž svoje osi (ali pravokotno nanjo). Ko se točka ubiranja premakne proti koncu osi rezkarja, ta odreže vzdolž svoje osi (ali pravokotno nanjo), se vrne na začetek brez rezalnega giba in nato spet zareže v obdelovanec. Pri srednjih in nizkih hitrostih je mogoče uporabiti pristop z recipročnim aksialnim pomikom, kjer se točka pomika vzvratno od konca proti začetku. To metodo je treba prilagoditi, da se izognemo pomanjkljivostim ponavljajočega se aksialnega pomika.

Postavljeni so bili štirje modeli diagonalnega odvalnega rezkanja po načelu čistega kotaljenja z enakovredno dolžino loka na surovcu, tako da hitrost rezkarja ostane konstantna. Štirje modeli obdelave, ki ustrezajo štirim verjetnim delovnim situacijam, so bili preverjeni z virtualnim odvalnim rezkanjem eliptičnega zobnika s poševnim ozobjem tretjega reda. Analiziran/a je bila linearna/kotna hitrost/pospešek vsake osi za primerjavo njihovih dinamičnih lastnosti v štirih delovnih situacijah. Tako sta se progresivno izkristalizirali dve odlični strategiji in modeli z odličnimi dinamičnimi lastnostmi. Eliptični zobnik s poševnim ozobjem tretjega reda je bil uspešno obdelan po metodi recipročnega aksialnega pomika. Uporabnost strategije in veljavnost modelov obdelave sta bili preizkušeni z ozirom na tri merila: življenjsko dobo odvalnega rezkarja, natančnost profila zob in mikrotopografijo bokov zob. Članek vsebinsko spada na področje uporabe numerične analize pri obdelavi neokroglih zobnikov.

Rezultati in ugotovitve:
1) Strategija diagonalnega odvalnega rezkanja lahko popolnoma odpravi omenjene težave. Preverjena je bila z virtualno obdelavo v štirih verjetnih delovnih situacijah, kjer poti orodij kažejo enakomerno natančnost zob.
2) Pri visokohitrostnem odvalnem rezkanju ima prednost shema 'V', saj ima boljše dinamične lastnosti hitrosti in pospeškov kot shema 'U'. Za srednje- in nizkohitrostno odvalno rezkanju je mogoče uporabiti shemi 'U' in 'V', čeprav je boljša shema 'V'. Hitrosti in pospeški osi pri shemah 'U' in 'V' ne vplivajo na različne smeri vrtenja zob. V tem delu je bila potrjena strategija recipročnih aksialnih pomikov, ki ne pušča sledov na bokih zob in je brez praznega hoda rezkarja.
3) Eksperimenti so pokazali pravilnost ter uporabnost modela obdelave (19) in njegovih strategij za implementacijo. Diagonalno odvalno rezkanje ima prednost pred nediagonalnim odvalnim rezkanjem zaradi 3,68-krat daljše življenjske dobe orodja, stabilnejša pa je tudi mikrotopografija zob za prenos gibanja.

Zaradi prostorskih omejitev ni bila preverjena pravilnost ubiranja zobnikov in tema zato ostaja odprta za prihodnje raziskave.

V prispevku je predstavljen teoretično zanimiv pristop k izdelavi neokroglih zobnikov s poševnim ozobjem po postopku diagonalnega odvalnega rezkanja. Metode in rezultati iz tega članka so zaradi podobnosti uporabni tudi pri strojih za brušenje polžastih zobnikov.
Ključne besede: neokrogli zobniki s poševnim ozobjem, diagonalno odvalno rezkanje, modeli obdelave, življenjska doba odvalnega rezkarja

*Naslov avtorja za dopisovanje: Politehnika Anhui, Šola za strojništvo in avtomobilsko tehniko, Wuhu 241000, Kitajska, Liuyoyu1@163.com

Konceptualna zasnova in preliminarna analiza konstrukcije satelita za lovljenje asteroidov z napihljivo košaro

Alessandro Ceruti[1,*] – Siro Pettenuzzo[2] – Marco Tuveri[3]

[1] Univerza v Bologni, Oddelek za industrijski inženiring – DIN, Italija
[2] Univerza v Bologni, Fakulteta za tehniko in arhitekturo, Italija
[3] Univerza v Bologni, Medoddelčno središče za industrijske raziskave v aeronavtiki, Italija

Narejenih je bilo že več študij na temo misij s človeško posadko, katerih cilj naj bi bil uloviti asteroid in ga preusmeriti v nizko zemeljsko orbito. Takšne študije so uporabne za razvoj tehnologij za preusmerjanje asteroidov, ki bi lahko udarili v zemljo, kakor tudi za preučevanje mineralne sestave teles, ki prihajajo iz globin vesolja. Uresničljivost takšnih vesoljskih mesij so dokazale študije Keckovega instituta in agencije NASA. Osnovna zamisel Keckovega dela je ulov asteroida premera 7 metrov s pomočjo orbitalnega satelita z napihljivo konstrukcijo, ki se v vesolju razširi in obda skalo. Za transport takšnega satelita v orbito bi bilo primernih več vesoljskih plovil premera 4 m do 4,5 m. Omejitev velikosti nosilnih raket je spodbuda za razvoj razširljivih ali napihljivih naprav za aplikacije v vesolju, ki zahtevajo velike konstrukcije. Vse te konceptualne študije pa zahtevajo tudi podrobnejšo zasnovo profila misije, sistemov, opreme in konstrukcije takšnega satelita. Članek obravnava tretji vidik – zasnova konfiguracije in konstrukcije satelita zahteva inovativen proces projektiranja in dimenzioniranja napihljivega dela satelita. Namen predstavljenega dela je opis metodologije konstruiranja in simulacije vedenja napihljivega dela satelita po metodi končnih elementov (MKE).

Problem, ki ga je treba razrešiti, je razvoj metodologije za poglobljeno zasnovo napihljivega dela satelita. Zaradi kompleksnega poteka snovanja je nujno pripraviti predloge različnih konceptov konfiguracij, med njimi izbrati najprimernejšega, ter na podlagi tega sprožiti podrobnejšo fazo dimenzioniranja in opredeljevanja konstrukcijskih podrobnosti. Vrednotenje različnih konfiguracij je bilo opravljeno po pristopu odločanja na podlagi več atributov (MADM), za konstrukcijski proces pa je bila uporabljena analiza po MKE.

Vrednotenje obremenitev konstrukcije koša satelita med misijo lova na asteroid je zelo kompleksna naloga, saj zahteva upoštevanje več dejavnikov: oblike asteroida, ki je lahko okrogla ali (bolj verjetno) podolgovata, njegove vztrajnosti in vrtilne hitrosti, trdnosti, možnih udarcev pri pristajanju ter sprememb centripetalnega pospeška zaradi rotacijske hitrosti satelita med združevanjem. V okviru naštetih negotovosti smo izvedli primerjalno študijo različnih konstrukcijskih rešitev koša za ovrednotenje vzdrževanja notranjega tlaka in končne oblike po napihovanju. Pri analizi po MKE je bilo ugotovljeno, da je za konvergenco pomikov in napetosti potrebno dušenje modela (v tem primeru α dušenje). Za upoštevanje kompresijskega vedenja tkanine je potreben model tkanine za simulacijo kompresijskih slabosti in zmanjšanja napetosti, v študiji pa je predlagan membranski element.

Po simulaciji z MKE je mogoče zaključiti, da je uporaba napihljivih konstrukcij za lov na asteroide povezana s težami, ki so tudi sicer značilne za satelite. Vsekakor pa bi bile uporabne tudi dodatne analize in eksperimentalni preizkusi za natančnejšo uglasitev modela po MKE.

V nadaljevanju bi bilo smiselno bolje preučiti podrobnosti, kot sta modeliranje stika med elementi tkanine ter simulacija trkov med asteroidom in satelitom. Podrobne študije kompromisov za ugotavljanje najprimernejšega tlaka napihovanja bodo možne, ko bo na voljo realna simulacija lova na asteroid. Tukaj predstavljena metodologija pa daje informacije o možnem poteku prihodnjih raziskav.

Rezultati študije so razvita metodologija za razvrščanje možnih konfiguracij, predlog oblike napihljivega koša, seznam smernic pri analizi napihljivih konstrukcij po MKE ter definicija uporabnega kroja tkanine. Pred misijo lova na asteroid bo v vsakem primeru treba napisati še veliko študij, članek pa usmerja pozornost na nekatere izzive pri snovanju in konstrukciji.

Ključne besede: konceptualna zasnova, napihljiva konstrukcija, MKE, MADM, tkanina, α dušenje, mehki materiali

---

Doktorske disertacije, specialistično delo, magistrska dela, diplomske naloge

DOKTORSKE DISERTACIJE

Na Fakulteti za strojništvo Univerze v Ljubljani so obranili svojo doktorsko disertacijo:

● dne *8. aprila 2015* **Matic TEPEŠ** z naslovom: »Razvojni model orodjarne bodočnosti« (mentor: prof. dr. Janez Kopač, somentor: izr. prof. dr. Peter Krajnik);

Delo vsebuje sintezo interdisciplinarnega pregleda literature s področij sodobne organizacije in sodelovanja, napovedi in trendov avtomobilske industrije kot kupca, novih omogočitvenih tehnologij ter zahtev globalnega poslovnega okolja. Na podlagi pregleda vrednostne verige orodjarne in teorije managementa izdelka skozi celotno dobo trajanja ter preko evropskih smernic je preučena možnost ustvarjanja dodane vrednosti znotraj orodjarskega sektorja. V delu je postavljen predlog modela, osnovan na hipotezi, da je s pomočjo novih, specifičnih organizacijskih in tehnoloških prijemov, možno ustvariti dodano vrednost za kupce. Podani so predlogi za ustvarjanje dodane vrednosti v očeh kupcev in za njeno realizacijo. Predlog modela je raziskan preko dveh instrumentov. Prvi je namenjen raziskavi in validaciji osnovih idej modela s strani kupcev in je osnova za drugega, ki je namenjen raziskavi proizvajalcev namenskih orodij, strojev in naprav. Ocenjeni so večji trendi, testirane so prioritete in videnje dodane vrednosti s strani kupcev, pomembnost komunikacije in sodelovanja med deležniki, uporaba IKT ter organizacijska fleksibilnost. Identificirana in rangirana je pomembnost tehnoloških indikatorjev za nadzor na daljavo, preučeno je tudi mnenje samih proizvajalcev. Razvit je alternativni poslovni model za podjetja iz orodjarstva in strojegradnje ter strateški okvir za razvoj izdelkov in storitev, ki je skladen z migracijo vrednosti v industriji, utemeljeno znotraj naloge;

● dne *10. aprila 2015* **Janez TRATAR** z naslovom: »Robotizirani sistemi za obdelavo lesa in kovin« (mentor: prof. dr. Janez Kopač, somentor: doc. dr. Franci Pušavec);

V doktorski disertaciji je predstavljena uporaba industrijskega robotskega manipulatorja v namene aplikacij mehansko obdelovalnih tehnologij, predvsem obdelav lesa, sekundarnih lesnih izdelkov in kovin. Na podlagi združevanja obstoječih standardov iz robotike ter obdelovanih strojev so bile eksperimentalno določene karakteristike robotske roke pod lahkimi obdelovalnimi pogoji. Postavljen je primer testnega kosa za šest osne industrijske robote. Izvedena je karakterizacija orodja pri planarnih obdelavah lesa in lesnih plošč po robotovi delovni ravnini. Postavljena sta empirična modela za obrabo orodja in vrednosti velikosti amplitud vibracij. Zaradi problematike prisotnih vibracij med odrezovalnim procesom z robotsko roko, je razvit algoritem in postavljen celoten sistem adaptivnega krmiljenja. Robotska roka je krmiljena po podajalni hitrosti glede na vibracije, nastale pri procesu mehansko obdelovalnih procesov;

● dne *20. aprila 2015* **Aleš SLAK** z naslovom: »Optimizacija logistike manipulativnih procesov v tehničnih informacijskih sistemih« (mentor: izr. prof. dr. Jože Tavčar, somentor: prof. dr. Jožef Duhovnik);

Doktorsko delo obravnava problem optimiranja interne logistike manipulativnih procesov v sodobni proizvodnji. Na podlagi znanih metod in tehnik ter kompleksnosti proizvodnega sistema je predstavljen nov model integriranega sistema za planiranje, razvrščanje in obvladovanje proizvodnje v realnem času. Model vsebuje novo optimizacijsko metodo, s katero se je izvedla optimizacija logističnih procesov s posebnim poudarkom na planiranju in razvrščanju izdelkov, materialnih tokov ter logistiki orodij. Izkoristil se je potencial obojesmerne informacijske povezave med procesi. Metoda je v osnovi univerzalna in uporabna za različne tipe proizvodenj. V njej je zajeta relacijska podatkovna baza, matematični model z večkriterijsko ciljno funkcijo ter uporaba umetne inteligence. Razvito in opisano je praktično računalniško okolje, ki omogoča uporabo te nove metode. Metoda in uporabniški vmesnik sta bila preizkušena prek implementacije v realno okolje proizvodnega sistema.

*

SPECIALISTIČNO DELO

Na Fakulteti za strojništvo Univerze v Mariboru je z uspehom zagovarjal svoje specialistično delo:

dne *22. aprila 2015:*

Mihael KUKOVEC z naslovom: »Avtomatizacija proizvodnje predstikalnih naprav z uporabo načel vitke proizvodnje« (mentor: prof. dr. Borut Buchmeister).

*

MAGISTRSKO DELO

Na Fakulteti za strojništvo Univerze v Ljubljani so pridobili naziv magister inženir strojništva:

dne 24. aprila 2015:

Jure FILAK z naslovom: »Karakterizacija in zagotavljanje ustrezne priprave rezalnih robov sodobnih frezal« (mentor: doc. dr. Franci Pušavec, somentor: prof. dr. Janez Kopač);

Jan MOŽINA z naslovom: »Študija izvedljivosti avtomatskega zlaganja jedra transformatorja« (mentor: prof. dr. Janez Diaci);

Niko PINTAR z naslovom: »Konstrukcija in montaža elementov za zagotavljanje vodotesnosti pri aparatih za osebno nego« (mentor: izr. prof. dr. Niko Herakovič).

*

Na Fakulteti za strojništvo Univerze v Mariboru so pridobili naziv magister inženir strojništva:

dne 22. aprila 2015:

Nejc BOŽIČ z naslovom: »Koncipiranje in zasnova težkega členkastega transporterja« (mentor: izr. prof. dr. Stanislav Pehan);

Matej FÜRST z naslovom: »Koncipiranje in zasnova dozirne naprave za težko frakcijo« (mentor: izr. prof. dr. Stanislav Pehan);

Mitja OZMEC z naslovom: »Računalniška podpora pri načrtovanju razmestitve elementov proizvodnega sistema« (mentor: izr. prof. dr. Iztok Palčič);

Matej ULČNIK z naslovom: »Konstruiranje vpenjalne priprave za robotsko varjenje« (mentor: prof. dr. Srečko Glodež).

*

Na Fakulteti za strojništvo Univerze v Mariboru je pridobil naziv magister gospodarski inženir:

dne 22. aprila 2015:

Jaka ŠTEFANČIČ z naslovom: »Preoblikovanje skladišča tekstilne industrije za potrebe predelave polimerov« (mentor: izr. prof. dr. Tone Lerher, izr. prof. dr. Mojca Duh).

*

DIPLOMSKE NALOGE

Na Fakulteti za strojništvo Univerze v Ljubljani so pridobili naziv diplomirani inženir strojništva:

dne 10. aprila 2015:

Rok KONČINA z naslovom: »Načrtovanje in vodenje projekta izdelave tovornih vozil« (mentor: izr. prof. dr. Janez Kušar, somentor: prof. dr. Marko Starbek);

Marko MANFREDA z naslovom: »Strega obdelovalnih strojev z robotom« (mentor: prof. dr. Janez Kopač);

Domen VRHUNC z naslovom: »Zasnova in izdelava prototipa motorja EC« (mentor: prof. dr. Janez Kopač);

Aljaž HUSAK z naslovom: »Karakterizacija kavitacije v ventilih« (mentor: izr. prof. dr. Matevž Dular);

Lovro MOHORIČ z naslovom: »Cenovna presoja tehnologij učinkovite rabe energije v skoraj nič energijskih stavbah« (mentor: prof. dr. Sašo Medved);

Tadej PILAR z naslovom: »Razvoj orodja za dvokomponentno brizganje nosilca« (mentor: izr. prof. dr. Tomaž Pepelnjak);

Klemen ZOBAVNIK z naslovom: »Zasnova in izdelava mobilne enote za ugotavljanje toplotne odzivnosti podzemnih plasti« (mentor: doc. dr. Uroš Stritih, somentor: prof. dr. Vincenc Butala);

dne 13. aprila 2015:

Janez JAKOFČIČ z naslovom: »Razvoj strežne naprave za transport snopov statorskih lamel« (mentor: izr. prof. dr. Niko Herakovič).

*

Na Fakulteti za strojništvo Univerze v Mariboru je pridobil naziv diplomirani inženir strojništva:

dne 23. aprila 2015:

Gorazd ČREPINŠEK z naslovom: »Optimiranje rezanja cevnih navojev s prenosnimi napravami« (mentor: prof. dr. Franci Čuš, somentor: asist. Tomaž Irgolič).

*

Na Fakulteti za strojništvo Univerze v Ljubljani so pridobili naziv diplomirani inženir strojništva (VS):

dne 10. aprila 2015:

Miha ŠKAPIN z naslovom: »Analiza laserskih navarov na poškodovanih orodjih« (mentor: prof. dr. Janez Tušek);

dne 13. aprila 2015:

Tomaž LAVRENČIČ z naslovom: »Izboljšava postopka cementiranja pastorka« (mentor: izr. prof. dr. Roman Šturm, somentor: doc. dr. Tomaž Kek);

Sašo ZRNEC z naslovom: »Analiza delovanja toplotne črpalke« (mentor: izr. prof. dr. Andrej Kitanovski, somentor: prof. dr. Alojz Poredoš).

*

Na Fakulteti za strojništvo Univerze v Mariboru so pridobili naziv diplomirani inženir strojništva (VS):
dne 23. aprila 2015:

Lovro JUHART z naslovom: »Načrtovanje proizvodnje balkonskih ograj v podjetju Adamont d.o.o.« (mentor: doc. dr. Marjan Leber, somentor: prof. dr. Borut Buchmeister);

Nejc OGRINC z naslovom: »Vzdrževanje linije za litje v podjetju Talum d.d.« (mentor: doc. dr. Marjan Leber);

Uroš VODEB z naslovom: »Standardizacija na področju obdelovalnih in preoblikovalnih strojev« (mentor: izr. prof. dr. Ivan Pahole, somentor: red. prof. dr. Bojan Ačko).

*

Na Fakulteti za strojništvo Univerze v Mariboru sta pridobila naziv diplomirani inženir mehatronike (VS):
dne 23. aprila 2015:

Žiga PRAH z naslovom: »Izdelava štiriosnega CNC rezkalnega stroja za obdelavo mehkejših materialov« (mentorja: izr. prof. dr. Karl Gotlih, doc. dr. Suzana Uran);

Žiga ŽGANK z naslovom: »Posodobitev avtomatskega krmilja ohlajevalnega traku za kontrolirano ohlajevanje odkovkov v podjetju Unior d.d.« (mentorja: izr. prof. dr. Karl Gotlih, izr. prof. dr. Aleš Hace).

Information for Authors

All manuscripts must be in English. Pages should be numbered sequentially. The manuscript should be composed in accordance with the Article Template given above. The maximum length of contributions is 10 pages. Longer contributions will only be accepted if authors provide juastification in a cover letter. For full instructions see the Information for Authors section on the journal's website: http://en.sv-jme.eu .

SUBMISSION:
Submission to SV-JME is made with the implicit understanding that neither the manuscript nor the essence of its content has been published previously either in whole or in part and that it is not being considered for publication elsewhere. All the listed authors should have agreed on the content and the corresponding (submitting) author is responsible for having ensured that this agreement has been reached. The acceptance of an article is based entirely on its scientific merit, as judged by peer review. Scientific articles comprising simulations only will not be accepted for publication; simulations must be accompanied by experimental results carried out to confirm or deny the accuracy of the simulation. Every manuscript submitted to the SV-JME undergoes a peer-review process.

The authors are kindly invited to submit the paper through our web site: http://ojs.sv-jme.eu. The Author is able to track the submission through the editorial process - as well as participate in the copyediting and proofreading of submissions accepted for publication - by logging in, and using the username and password provided.

SUBMISSION CONTENT:
The typical submission material consists of:
- A **manuscript** (A PDF file, with title, all authors with affiliations, abstract, keywords, highlights, inserted figures and tables and references),
- Supplementary files:
  • a **manuscript** in a WORD file format
  • a **cover letter** (please see instructions for composing the cover letter)
  • a ZIP file containing **figures** in high resolution in one of the graphical formats (please see instructions for preparing the figure files)
  • possible **appendicies** (optional), cover materials, video materials, etc.
Incomplete or improperly prepared submissions will be rejected with explanatory comments provided. In this case we will kindly ask the authors to carefully read the Information for Authors and to resubmit their manuscripts taking into consideration our comments.

COVER LETTER INSTRUCTIONS:
Please add a **cover letter** stating the following information about the submitted paper:
1. Paper **title**, list of **authors** and their **affiliations**.
2. **Type of paper**: original scientific paper (1.01), review scientific paper (1.02) or short scientific paper (1.03).
3. A **declaration** that neither the manuscript nor the essence of its content has been published in whole or in part previously and that it is not being considered for publication elsewhere.
4. State the **value of the paper** or its practical, theoretical and scientific implications. What is new in the paper with respect to the state-of-the-art in the published papers? Do not repeat the content of your abstract for this purpose.
5. We kindly ask you to suggest at least two **reviewers** for your paper and give us their names, their full affiliation and contact information, and their scientific research interest. The suggested reviewers should have at least two relevant references (with an impact factor) to the scientific field concerned; they should not be from the same country as the authors and should have no close connection with the authors.

FORMAT OF THE MANUSCRIPT:
The manuscript should be composed in accordance with the Article Template. The manuscript should be written in the following format:
- A **Title** that adequately describes the content of the manuscript.
- A list of **Authors** and their **affiliations**.
- An **Abstract** that should not exceed 250 words. The Abstract should state the principal objectives and the scope of the investigation, as well as the methodology employed. It should summarize the results and state the principal conclusions.
- 4 to 6 significant **key words** should follow the abstract to aid indexing.
- 4 to 6 **highlights;** a short collection of bullet points that convey the core findings and provide readers with a quick textual overview of the article. These four to six bullet points should describe the essence of the research (e.g. results or conclusions) and highlight what is distinctive about it.
- An **Introduction** that should provide a review of recent literature and sufficient background information to allow the results of the article to be understood and evaluated.
- A **Methods** section detailing the theoretical or experimental methods used.
- An **Experimental section** that should provide details of the experimental set-up and the methods used to obtain the results.
- A **Results** section that should clearly and concisely present the data, using figures and tables where appropriate.
- A **Discussion** section that should describe the relationships and generalizations shown by the results and discuss the significance of the results, making comparisons with previously published work. (It may be appropriate to combine the Results and Discussion sections into a single section to improve clarity.)
- A **Conclusions** section that should present one or more conclusions drawn from the results and subsequent discussion and should not duplicate the Abstract.
- **Acknowledgement** (optional) of collaboration or preparation assistance may be included. Please note the source of funding for the research.
- **Nomenclature** (optional). Papers with many symbols should have a nomenclature that defines all symbols with units, inserted above the references. If one is used, it must contain all the symbols used in the manuscript and the definitions should not be repeated in the text. In all cases, identify the symbols used if they are not widely recognized in the profession. Define acronyms in the text, not in the nomenclature.
- **References** must be cited consecutively in the text using square brackets [1] and collected together in a reference list at the end of the manuscript.
- **Appendix(-icies)** if any.

SPECIAL NOTES
Units: The SI system of units for nomenclature, symbols and abbreviations should be followed closely. Symbols for physical quantities in the text should be written in italics (e.g. v, T, n, etc.). Symbols for units that consist of letters should be in plain text (e.g. ms^{-1}, K, min, mm, etc.). Please also see: http://physics.nist.gov/cuu/pdf/sp811.pdf .

Abbreviations should be spelt out in full on first appearance followed by the abbreviation in parentheses, e.g. variable time geometry (VTG). The meaning of symbols and units belonging to symbols should be explained in each case or cited in a **nomenclature** section at the end of the manuscript before the References.

Figures (figures, graphs, illustrations digital images, photographs) must be cited in consecutive numerical order in the text and referred to in both the text and the captions as Fig. 1, Fig. 2, etc. Figures should be prepared without borders and on white grounding and should be sent separately in their original formats. If a figure is composed of several parts, please mark each part with a), b), c), etc. and provide an explanation for each part in Figure caption. The caption should be self-explanatory. Letters and numbers should be readable (Arial or Times New Roman, min 6 pt with equal sizes and fonts in all figures). Graphics (submitted as supplementary files) may be exported in resolution good enough for printing (min. 300 dpi) in any common format, e.g. TIFF, BMP or JPG, PDF and should be named Fig1.jpg, Fig2.tif, etc. However, graphs and line drawings should be prepared as vector images, e.g. CDR, AI. Multi-curve graphs should have individual curves marked with a symbol or otherwise provide distinguishing differences using, for example, different thicknesses or dashing.

Tables should carry separate titles and must be numbered in consecutive numerical order in the text and referred to in both the text and the captions as Table 1, Table 2, etc. In addition to the physical quantities, such as t (in italics), the units [s] (normal text) should be added in square brackets. Tables should not duplicate data found elsewhere in the manuscript. Tables should be prepared using a table editor and not inserted as a graphic.

REFERENCES:
A reference list must be included using the following information as a guide. Only cited text references are to be included. Each reference is to be referred to in the text by a number enclosed in a square bracket (i.e. [3] or [2] to [4] for more references; do not combine more than 3 references, explain each). No reference to the author is necessary.

References must be numbered and ordered according to where they are first mentioned in the paper, not alphabetically. All references must be complete and accurate. Please add DOI code when available. Examples follow.

Journal Papers:
Surname 1, Initials, Surname 2, Initials (year). Title. Journal, volume, number, pages, DOI code.

[1] Hackenschmidt, R., Alber-Laukant, B., Rieg, F. (2010). Simulating nonlinear materials under centrifugal forces by using intelligent cross-linked simulations. *Strojniški vestnik - Journal of Mechanical Engineering,* vol. 57, no. 7-8, p. 531-538, DOI:10.5545/sv-jme.2011.013.
Journal titles should not be abbreviated. Note that journal title is set in italics.

Books:
Surname 1, Initials, Surname 2, Initials (year). Title. Publisher, place of publication.

[2] Groover, M.P. (2007). *Fundamentals of Modern Manufacturing*. John Wiley & Sons, Hoboken.
Note that the title of the book is italicized.

Chapters in Books:
Surname 1, Initials, Surname 2, Initials (year). Chapter title. Editor(s) of book, book title. Publisher, place of publication, pages.

[3] Carbone, G., Ceccarelli, M. (2005). Legged robotic systems. Kordić, V., Lazinica, A., Merdan, M. (Eds.), Cutting Edge Robotics. Pro literatur Verlag, Mammendorf, p. 553-576.

Proceedings Papers:
Surname 1, Initials, Surname 2, Initials (year). Paper title. Proceedings title, pages.

[4] Štefanić, N., Martinčević-Mikić, S., Tošanović, N. (2009). Applied lean system in process industry. *MOTSP Conference Proceedings*, p. 422-427.

Standards:
Standard-Code (year). Title. Organisation. Place.

[5] ISO/DIS 16000-6.2:2002. *Indoor Air – Part 6: Determination of Volatile Organic Compounds in Indoor and Chamber Air by Active Sampling on TENAX TA Sorbent, Thermal Desorption and Gas Chromatography using MSD/FID*. International Organization for Standardization. Geneva.

WWW pages:
Surname, Initials or Company name. Title, from http://address, date of access.

[6] Rockwell Automation. Arena, from *http://www.arenasimulation.com,* accessed on 2009-09-07.

EXTENDED ABSTRACT:
When the paper is accepted for publishing, the authors will be requested to send an **extended abstract** (approx. one A4 page or 3500 to 4000 characters). The instruction for composing the extended abstract are published on-line: http://www.sv-jme.eu/information-for-authors/ .

COPYRIGHT:
Authors submitting a manuscript do so on the understanding that the work has not been published before, is not being considered for publication elsewhere and has been read and approved by all authors. The submission of the manuscript by the authors means that the authors automatically agree to transfer copyright to SV-JME when the manuscript is accepted for publication. All accepted manuscripts must be accompanied by a Copyright Transfer Agreement, which should be sent to the editor. The work should be original work by the authors and not be published elsewhere in any language without the written consent of the publisher. The proof will be sent to the author showing the final layout of the article. Proof correction must be minimal and executed quickly. Thus it is essential that manuscripts are accurate when submitted. Authors can track the status of their accepted articles on http://en.sv-jme.eu/.

PUBLICATION FEE:
Authors will be asked to pay a publication fee for each article prior to the article appearing in the journal. However, this fee only needs to be paid after the article has been accepted for publishing. The fee is 240.00 EUR (for articles with maximum of 6 pages), 300.00 EUR (for articles with maximum of 10 pages), plus 30.00 EUR for each additional page. The additional cost for a color page is 90.00 EUR. These fees do not include tax.

Contents

Papers